NASA Technical Memorandum 85813

NASA-TM-85813 19840020966

AN INVESTIGATION OF THE EXISTENCE OF A SURFACE WATER LAYER ON AIRCRAFT RADOMES DURING SIMULATED FLIGHT IN HEAVY PRECIPITATION

J. R. BRANSTETTER (EDITOR), M. C. BAILEY, C. P. HEARN,
R. E. DUNHAM, JR., R. H. COUCH, H. A. VERSTYNEN,
G. L. GENTRY, JR., AND J. B. WILLIAMS

JUNE 1984

National Aeronautics and Space Administration

Langley Research Center
Hampton, Virginia 23665

FEDERAL AVIATION ADMINISTRATION

LANGLEY FIELD OFFICE

TABLE OF CONTENTS

LIST OF ILLUSTRATIONS

Page

AN INVESTIGATION OF THE EXISTENCE OF A SURFACE WATER LAYER ON AIRCRAFT RADOMES DURING SIMULATED FLIGHT IN HEAVY PRECIPITATION

J. R. Branstetter (Editor) and H. A. Verstynen
NASA/Langley Development & Logistics Field Office

M. C. Bailey, C. P. Hearn, R. E. Dunham, Jr., R. H. Couch,
G. L. Gentry, Jr., and J. B. Williams
NASA Langley Research Center

I. SUMMARY

An experiment to investigate the electromagnetic attenuation effects of an impacting water spray on an aircraft weather radome was conducted in Langley's 4 x 7 m. wind tunnel equipped with a water spray system. Results indicate no significant liquid water film formed at the stagnation point of the radome under the test conditions. However, a water "sheath" was observed standing away from the radome surface, which could possibly have significant attenuation properties of its own. Due to the lack of fidelity in modeling both the natural environment with the tunnel apparatus and the water sheath, it is recommended that further studies be undertaken to better define the water distribution in the vicinity of the radome and measure its effect on weather radar performance.

II. INTRODUCTION

This report describes the results of joint research conducted by NASA and the FAA to examine whether aircraft weather radomes, having various surface qualities and subjected to conditions simulating flight in heavy precipitation, would support a water layer on the surface. Based on the experimental findings, an estimation of the water surface thickness is made for use in calculating the potential attenuation of such a layer.

The project stems from an National Transportation Safety Board recommendation (A781) which said in part that the FAA should, " . . . initiate research to determine the attenuating effects of various levels of precipitation and icing on airborne radomes of both X- and C-band radars, and disseminate to the aviation community any data derived concerning the limitations of airborne radar in precipitation." The NTSB recommendation was predicated on events surrounding the crash of a Southern Airways DC-9-31 jetliner (Flight 242 at New Hope, Georgia, on April 4, 1977) which suggested the possibility of performance degradation of the contour function of the on-board weather radar. NTSB's investigation disclosed, " . . . the flight had entered an intense precipitation area which resulted in the failure of both of the aircraft's engines. Considering the level of experience and qualifications of the crew, the Safety Board believes that they most likely were receiving a radar signal which was attenuated by the precipitation in which the flight was conducted."

Since that report, the crash of an Air Wisconsin Swearingen Metro (Flight 965 near Valley, Nebraska on June 12, 1980) during flight in heavy

rain points again to the little known effects of water accretion on a radome and its subsequent effect on the reliability of indications of airborne weather radar installations.

In an effort to acquire documented evidence of research that may have been accomplished, the FAA Office of Airworthiness (AWS-130) initiated informal coordination with the Radio Technical Commission for Aeronautics (RTCA), industry, U. S. Air Force, and NASA. Industry representatives on RTCA SC-133 (Weather Radar) generally agreed that attenuation effects of rain and ice were basically known, and that icing was of limited concern. The major unknown was whether a water layer could exist on a radome under actual flight conditions, and if it could exist, it's approximate thickness. If these parameters were known, attenuation could be more reliably computed.

NASA technical personnel (at the request of FAA) initiated a limited literature survey and related experience search to determine what research had been accomplished. This investigation concluded that evidence of a standing-water layer on large radomes under static conditions could exist and that further research to determine the actual presence and effect of a water layer on aircraft radomes in flight appeared to be needed. The major questions to be addressed were whether a radome in flight will allow a water layer to exist and, if it does exist, what is the approximate water layer thickness. NASA further concluded that if a water layer of some measurable thickness (0.015 inch or more) does exist, then the degradation of the performance of airborne weather radar can be reliably calculated.

III. DESCRIPTION OF EXPERIMENT

The experiment devised for measuring the surface water layer phenomena entailed placing an aircraft radome instrumented with a pair of microwave reflectometers in a wind tunnel equipped with a water spray system. Figure 1 shows the "old" radome installed in the tunnel with the spray bar in the foreground.

A. Test Radomes

The two radomes, designated herein as "new" and "old", were chosen to provide a comparison of the water retention capabilities between a radome with a newly-painted surface and one having a weather-eroded surface. (See Fig. 2)

The "new" radome was obtained through USAF supply channels which resulted in the purchase of a literally new T-39 radome. When received, the radome was found to be uncut and oversized for mating with the afterbody section that was to be used for mounting it in the wind tunnel. To adapt it to fit the afterbody, the model shop cut and reformed the radome. This "surgery" required that the radome be reglassed in certain areas and repainted first with a primer coat and then with the smooth polyurethane surface finish coat. Neither process should have significantly altered the electrical characteristics required for these tests since, with the experimental instrumentation used, it was not necessary to scan any large cross-sectional areas (of the radome) as an operating radar would have had to do.

The "old" radome was obtained from the USAF, having been removed from actual service and scheduled for refurbishing. Prior to testing, this radome was used as the model for mounting the reflectometers and designing the afterbody. Hence, the surface suffered more deterioration than airborne weathering alone had accomplished.

B. Measurement Technique

Water-layer thickness was determined by a two-step process whereby measured values of a parametric variable, the feed-point impedance of a test antenna, were related to water thickness through an analytical model.

The technique used in this experiment was derived from previous research done by NASA scientists to determine the properties of dielectric layers over horn and waveguide antennas and subsequently determining the thickness of plasma sheaths overlying the antennas of space reentry vehicles. In theory, placing a layer of a lossy dielectric, such as water, over an otherwise well-matched antenna aperture will result in a change of the amplitude and phase of the wave reflected back toward the antenna signal source. By measuring and analyzing these parameters, the characteristics of the reflected wave can be determined, and once known, calculations can be made which will indicate the effect caused by an accretion layer on the surface. (Mathematical derivations for the technique can be found in Appendix A(1), "Analytical Modeling.")

For this experiment two microwave reflectometer sensor units were constructed and installed in the radomes. One sensor was located at the stagnation point and the other approximately 30 degrees off-axis in the horizontal plane. Each reflectometer consisted of a microwave horn-type antenna designed for Ku-band operation (the design frequency of the radome), a Gunn oscillator signal source, a specially designed stripline with integral voltage probes, and a dual-directional coupler. (A schematic diagram of the system is shown in figure 3 and the hardware mounted in one of the radomes is shown in figure 4.) The horns were fitted to the inner surface of the radome while attempting to electrically match the horn to the radome so that when the surface is dry there are no signal reflections.

Analog voltages from the four probes in each stripline along with foreward and reverse voltages from each dual-directional coupler were digitized and recorded for analysis. During the tests, the reflectometer package was wrapped in an insulating blanket to maintain the components at a constant temperature (120+/-0.2 degrees F.).

C. Data Acquisition System

The design for the data acquisition system used in this test is shown in figure 5 and the actual hardware is shown in the background of figure 2. This system represents a simple and straightforward approach to the problem of acquiring and recording the data of interest for subsequent data reduction and also providing the system operator with an indication of system performance in real time.

An eight-bit microcomputer was employed having EPROM program memory and static RAM. Voltage data measurements from the sensors were converted for digital processing by analog-to-digital modules each consisting of an eight-channel multiplexer, a sample-and-hold amplifier, and the analog-to-digital converter. The converter has twelve-bit resolution and was configured for unipolar operation. An internal time code generator provided timing information to identify data as to date and time-of-day and was recorded along with the voltage data. The keyboard and display unit allowed the operator to initialize the time code generator and to start and stop the tape recorder, in addition to displaying voltage data in real time. Finally, all data was tape recorded on a one-half inch IBM compatible seven-track tape for use in the data reduction process.

D. Wind Tunnel

The Langley 4- by 7-m wind tunnel was used for this test. The general characteristics and operating ranges for this facility are discussed in reference 1. For the purpose of these tests, a water-spray manifold was installed in the tunnel and positioned with respect to the test radome as illustrated in figures 1 and 6.

E. Water Spray System

The spray manifold was made from streamline pipe having a fineness ratio of 2.2 and a streamwise dimension of 3.5 inches. The manifold had provisions for installing water injection nozzles in the aft portion every 6 inches along the span. The nozzles chosen for this test were Spraying Systems Inc.,

model #1570. These were installed every foot along the trailing edge and were oriented so as to inject water aft in the streamwise direction. Water was provided to the manifold through a solenoid control supply system as seen in figure 6. In order to get the desired flow rate, only half of the ports on the spray bar were needed. This caused an asymetrical positioning of the nozzles with respect to the radome stagnation point. To alleviate the possibility of inadequate spray formation, two different nozzle configurations were tried. Designated Configuration No. 1 and No. 2, respectively, the nozzles were shifted laterally by one port between runs for testing both the old and new radomes (see figure 7).

F. Test Conditions

To check for water accretion over a wide range of airspeeds and water flow conditions a test matrix was established around the tunnel and spray system limitations. Figure 8 shows the test points used for data collection. The wind tunnel airspeeds ranged from 97 to 192 knots with test points taken at speeds of approximately 97, 122, 145, 165, 183, and 192 kts. The water spray system was capable of delivering liquid water content ranging from 6 to 16 gm/m^3.

The "calibration" of the spray rig was performed using high-speed photography to document the spray characteristics. Spark-gap photo tubes of finite pulse duration were used to produce a photograph of spray drop streaks. Based on the measured length of the streaks and the known pulse duration, the spray drop velocities were determined. For the spray range over which calibrations were obtained (Fig. 8), the spray drops were found to be moving at nearly free-stream velocity. Drop size distribution was determined from photographs obtained

with very short light pulse durations, which effectively stopped drop motion. For all configurations evaluated, the drop size distribution was found to be log-normally distributed with a median drop diameter of about .4 mm. The rain spray concentration for the calibrated conditions was obtained from the photographic area of spray coverage at the radome test position, the velocity of the spray, and the mass flow through the spray manifold.

Table 1 lists the wind tunnel parameter sets for the data runs using both radomes and both nozzle configurations. Certain test points were omitted in successive runs which seemed redundant or added no new insight to the experiment.

Looking at figure 8, it will be noted that the tunnel and spray system were calibrated for only a portion of the overall matrix. This was due to adding test points during the actual test runs to look at the effects of lower spray rates and higher tunnel speeds in an attempt to examine the full spectrum of available test conditions, after it was discovered that drop sizes were much smaller and liquid water content was higher than what would typically be considered "heavy rain."

In the calibrated region (circular symbols, figure 8), the spray concentration was computed to vary from 9 gm/m^3 to 16 gm/m^3. In the uncalibrated region (square symbols, figure 8), the liquid water content was estimated to range from 6 gm/m^3 to 24 gm/m^3 on the assumption that the spray area coverage only slightly decreased and that the droplets were moving at free-stream velocity.

IV. RESULTS AND DISCUSSION

Tests were run in the wind tunnel on August 4 and 5, 1982, using both radomes and covering the test conditions previously described.

A. Water Spray Definition

The calibration of the water spray indicated that the median drop diameter was .4 mm. This drop diameter turned out to be considerably smaller than would be found in natural rainfall of an equivalent liquid water content. Additionally, the spray does not have the exact velocity orientation with respect to the test radome as would occur in a rain encounter. Because the spray system was near the radome, little vertical motion was imparted to the spray due to gravitational effects. This error was considered to be small since the downward terminal velocity of rain drops is low compared to the free-stream velocity of an encountering aircraft. Also because of tunnel turbulence and nozzle placement, there was some fluctuation of the spray about the radome causing some nonuniformity of wetting. The liquid water content for these tests was very high (6 gm/m^3 to 24 gm/m^3).

The National Weather Service designates storm severity in terms of radar VIP levels (Video Integrated Precipitation). A VIP level 6 represents the highest level reportable in this standardized scheme and corresponds to a liquid water content of as low as 4 gm/m^3. However, liquid water contents on the order of 25 gm/m^3 are believed to occur occasionally. The spray characteristics of small drop diameter, high liquid water content, and nonuniformity contributed to test conditions which lack similarity to the natural environment.

B. Visual Observations

Photographic evidence and observations made during the tests indicate the apparent existence of a water layer on the radome surface for all of the test conditions examined. The form of the water layer was different for the two radomes showing a dependency on surface condition. Water on the "old" radome formed in sheets that contained very small ripples. Water on the "new" radome formed globules and rivulets that traveled aft at substantially less than free-stream velocity. There were no discernable differences in water layer patterns or formation for a particular radome that could be attributed to velocity or liquid water content, based on visual observation.

What was unexpected was the occurrence of a phenomenon depicted in figure 9. Water droplets seemed to form a sheath or concentration of spray that stood some distance off of the radome surface, similar to a shock wave boundary layer. The sheath appeared to thicken with increasing distance from the stagnation point. The droplet size in the sheath appeared to be small, like a fine mist. It could not be determined whether the sheath was composed of small free-stream droplets that were following streamlines around the radome, fractionated droplets that had rebounded from impact with the surface, or a combination of both.

C. Reflectometer Measurements and Interpretation

The reflectometer measured the reflection coefficient amplitude and phase angle of the reflected microwave signal caused by the impedance mismatch produced by the wet radome and external spray. Data obtained during the test are presented in tabular form in Table 1 and graphically in figs. 10 and 12.

The time history data for the reflection coefficient for the front sensor are shown in Appendix B. Data recording was begun approximately 5 seconds prior to the release of water into the flow stream, providing a reference point to show the "no water" condition. As can be seen, the amplitude and phase angle change significantly when the spray is activated. The fluctuations portrayed in the data seem to be attributed to the unsteady nature of the spray impinging upon the radome as observed on motion picture film taken during the tests. This effect could also be due to water droplets striking the radome and producing a nonuniform water film thickness or rivulets of water flowing over the surface as visually noted in the previous section.

The reflection coefficient data for the front sensor are summarized in figure 10 for both old and new radomes. These data points were averaged over a ten-second time interval, beginning after initial radome wetting and ceasing prior to shutting off the spray, to obtain the statistical means for the amplitude and phase components of the reflection coefficient. From the data in Appendix B, it can be seen that a slight impedance mismatch (i.e., non-zero reflection coefficient amplitudes in dry conditions) existed at the radome/horn interface with no water present, hence, the parameters constituting the radome layer in the analytical model were adjusted to simulate the mismatch observed during dry radome measurements. It can be observed from examination of the "new" radome data in fig. 10 that an impedance-matching effect occurs which reduces the amplitude of the reflection coefficient as compared to the dry radome value.

An interpretation of the test results for the side sensor was not attempted since an appreciable impedance mismatch existed for the horn mounted in the side of the radome. This was caused by a significant misalignment between the horn axis and the normal to the radome surface; a discrepancy

that was noted only after the testing had been completed and the apparatus removed from the tunnel.

D. Water Thickness Determination

The measurements were interpreted using a planar model of the radome and water film as illustrated in figure 11. In figure 12, a comparison is made between the old radome measurements and the plane wave calculations. (See Appendix A for the derivation of the plane wave model used.) The range of water film thickness inferred by this comparison is inconsistent between the amplitude and phase data. This inconsistency implies that the water film is thin enough such that the reflectometer measurements are influenced strongly by reflections outside the water film. Apparently, this is due to the sheath of water droplets standing off of the surface noted previously by photographic observation - figure 9. Examination of one of the time-history records (run-point No. 1-6 for the front sensor, see Appendix B) verified that the spray contributed appreciably to the reflectometer measurements. This is manifested by an immediate change in the reflectometer response when the spray was shut-off leaving a residual reflection due to a surface water film that gradually returned to the dry radome values as the film evaporated.

A refinement of the calculations was attempted by modeling the spray as multiple layers outside the liquid water film as shown in figure 13. The transition region between the water spray and the air was modeled as a stepped-approximation to a cosine function.

The calculated reflection coefficient was plotted as a function of the spray thickness with the water film thickness as a parameter (see Appendix C). The calculations were performed for different values of the water volume density

of the spray and the thicknesses of the spray transition region based upon best reasonable estimates of these parameters. The measurements for both the old and new radomes were plotted on the same figures at a value of spray thickness which was consistent with the amplitude and phase used for inferring the water film thickness. From the figures in Appendix C it can be seen that a small change in the thickness of the water film can produce a substantial change in the reflection coefficient.

The water film thickness inferred by the measurements was less than 0.0015 cm for all test runs. The observed thickness of the water film was consistently less for the new radome than for the old radome; as would be anticipated since the rougher surface of the old radome should have had a greater affinity for water accretion in a wind-blown spray environment.

Figure 14 shows the calculated one-way transmission loss through a planar water film. Note that less than 1dB transmission loss can be anticipated for the water film thicknesses observed during the experiment. Figures 15-16 show the additional transmission loss through a planar uniform spray boundary layer outside the radome and water layer. The additional transmission loss due to the spray boundary layer is of the order of 0.5dB or less.

V. CONCLUSIONS

A. Concluding Remarks

A wind tunnel test was conducted to determine the possible existance of a water film on a radome in a water spray environment spanning a range of liquid water contents from 6 gm/m^3 to 24 gm/m^3. Data from microwave reflectometers and a plane wave propagation model were used to estimate the water film thickness and resultant radar transmission loss.

The results of the experiment indicate no significant liquid water film formed at the stagnation point of the radome under the test conditions. Predicted transmission loss at X-band and Ku-band is less than 1 dB for even the maximum water film thicknesses observed during the tests.

Due to the lack of similitude between the tunnel test conditions and the natural environment in conjunction with the simplified plane wave modeling of the complex curved radome, one must be cautioned about attempting to extrapolate the present results to real-world conditions.

There may be other mechanisms involved which could have a significant effect on radar performance, notably the sheath phenomenon observed. The effects of curvature of the radome and the sheath surrounding the radome have not been analyzed and could cause an appreciable change in the interpretation of the data. Additional effort appears to be needed to define the sheath phenomenon believed to be associated with small particle discrimination and to model the effects of this curved sheath upon radar performance.

B. Recommendations

NASA and the FAA should undertake further studies to better define the water distribution in the vicinity of the radome and measure its effect on weather radar performance. At present, it appears that direct measurement of radar transmissivity may be more useful than interpretation of reflectivity data for answering the basic question of whether the film/sheath environment severely degrades weather radar performance. Both wind tunnel experiments, where test conditions can be carefully controlled and measured, as well as flight tests, where higher dynamic pressure and real-world environmental conditions can be obtained, will likely be required to give a more conclusive answer.

TABLE 1

WIND TUNNEL TEST DATA REFLECTOMETER MEASUREMENTS

Run No. 1 - Old Radome, Nozzle Configuration No. 1

TEST POINT	TEST CONDITIONS			TIME		SENSOR DATA			
						FRONT		SIDE	
	Tunnel Velocity (kts.)	Liquid Water Content (gm/m^3)	Tunnel Dynamic Pressure (KPa)*	Start HH-MM-SS	Stop HH-MM-SS	Ampl. ρ	Phase Angle	Ampl. ρ	Phase Angle
1-4	0	0	0	13-0-28	13-0-37.9	.107	3.111	.264	.8178
1-5	145	0	3.21	13-04-09	13-04-27.9	.108	3.098	.259	.8307
1-6	146	9.4	3.21	13-06-59	13-07-25.9	.142	3.790	.279	.9410
1-8	122	11.2	2.26	13-42-45	13-43-10.9	.140	3.767	.273	.9748
1-9	97	14.0	1.44	13-45-13	13-45-37.9	.162	3.946	.281	1.0005
1-10	145	12.8	3.20	13-47-59	13-48-24.9	.140	3.764	.270	.9710
1-11	122	14.2	2.25	13-50-44	13-51-08.9	.142	3.766	.278	.9828
1-12	146	16.3	3.21	13-53-19	13-53-43.9	.135	3.697	.273	.9641
1-13	169	8.0	4.32	13-57-03	13-57-29.9	.133	3.674	.265	.9349
1-14	183	7.5	5.04	13-58-55	13-59-19.9	.127	3.555	.266	.9198
1-15	191	7.3	5.51	14-00-54	14-01-18.9	.128	3.600	.268	.9110
1-16	146	7.9	3.20	14-04-24	14-04-48.9	.127	3.563	.280	.9152
1-17	169	6.8	4.31	14-07-06	14-07-29.9	.126	3.538	.276	.9005
1-18	183	6.3	5.01	14-08-59	14-09-23.9	.123	3.502	.274	.8951
1-19	191	6.1	5.49	14-11-29	14-11-54.9	.123	3.498	.273	.9030
1-20	98	24.5	1.44	14-13-59	14-14-23.9	.165	3.953	.295	.9823
1-21	0	0	0	14-16-36	14-16-45.9	.109	3.106	.269	.8009
1-X	cup of water poured over front sensor			15-02-10	15-02-45.9	.586	5.174	.232	.8495
1-Y	cup of water poured over side sensor			15-03-25	15-03-35.9	.136	3.759	.364	.5780
1-Z	tin foil over front sensor			15-05-52	15-06.10.9	.536	.5980	.711	1.6161

Run No. 2 - Old Radome, Nozzle Configuration No. 2

TEST POINT	TEST CONDITIONS			TIME		SENSOR DATA			
						FRONT		SIDE	
	Tunnel Velocity (kts.)	Liquid Water Content (gm/m^3)	Tunnel Dynamic Pressure (KPa)*	Start HH-MM-SS	Stop HH-MM-SS	Ampl. ρ	Phase Angle	Ampl. ρ	Phase Angle
2-2	0	0	0	15-50-21	15-50-21	.106	3.145	.261	.8469
2-A	146	0	3.21	15-55-18	15-55-31.9	.107	3.139	.250	.8736
2-3	146	9.4	3.21	15-56-50	15-57-7.9	.128	3.621	.273	.9563
2-4	98	14.0	1.44	16-08-56	16-09-21.9	.153	3.860	.301	.9810
2-5	122	14.2	2.24	16-13-28	16-13-52.9	.147	3.802	.301	.9630
2-6	146	16.3	3.20	16-16-02	16-16-25.9	.139	3.732	.294	.9452
2-7	170	8.0	4.31	16-21-12	16-21-34.9	.126	3.562	.285	.9150
2-8	192	7.5	5.53	16-23-07	16-23-31.9	.122	3.468	.278	.9175
2-9	170	6.7	4.30	16-25-08	16-25-32.9	.123	3.523	.288	.8979
2-10	192	6.1	5.51	16-26-47	16-27-11.9	.121	3.443	.287	.8913
2-11	98	24.5	1.44	16-28-43	16-29-06.9	.166	3.964	.309	.9818
2-12	0	0	0	16-44-36	16-44-45.9	.111	3.105	.291	.7989
2-X	Shorts			17-04-27	17-04-35.9	.9023	3.111	1.099	2.8381

(* 1 Pascal = 1 nt/m^2)

TABLE 1

WIND TUNNEL TEST DATA REFLECTOMETER MEASUREMENTS

Run No. 3 - New Radome, Nozzle Configuration No. 1

TEST POINT	TEST CONDITIONS			TIME		SENSOR DATA			
						FRONT		SIDE	
	Tunnel Velocity (kts.)	Liquid Water Content (gm/m^3)	Tunnel Dynamic Pressure (KPa)*	Start HH-MM-SS	Stop HH-MM-SS	Ampl. ρ	Phase Angle	Ampl. ρ	Phase Angle
3-A	cup of water	poured over	side sensor	17-41-24	17-41-38.9	.100	1.6793	.230	.6391
3-B	cup of water	poured over	front sensor	17-42-59	17-43-07.9	.745	5.4021	.182	.9266
3-3	0	0	0	17-56-16	17-56-55.9	.107	1.6999	.179	.9361
3-4	146	0	3.20	18-02-26	18-02-40.9	.112	1.6998	.176	.9623
3-5	145	9.4	3.21	18-03-22	18-03-45.9	.097	1.8466	.182	.9433
3-6	165	14.0	1.45	18-06-03	18-06-23.9	.085	1.9482	.197	.9082
3-7	122	14.2	2.25	18-07-47	18-08-10.9	.085	1.9612	.194	.9148
3-8	146	16.3	3.21	18-10-46	18-11-10.9	.053	2.4323	.211	.9348
3-9	169	8.0	4.31	18-13-52	18-14-13.9	.087	1.9107	.200	.9338
3-10	191	7.3	5.49	18-15-32	18-15-52.9	.099	1.8196	.196	.9334
3-11	169	6.8	4.31	18-17-48	18-18-10.9	.088	1.9019	.200	.9122
3-12	191	6.1	5.50	18-19-14	18-19-33.9	.098	1.8413	.191	.9304
3-13	98	24.5	1.44	18-21-44	18-22-07.9	.047	3.0302	.237	.9204
3-14	0	0	0	18-33-41	18-33-50.9	.105	1.8231	.200	.9103
3-X	cup of water	poured over	front sensor	18-47-31	18-47-39.9	.707	5.2869	.188	.9177
3-Y	cup of water	poured over	side sensor	18-48-12	18-48-25.9	.099	1.7170	.195	.2375

Run No. 4 - New Radome, Nozzle Configuration No. 2

TEST POINT	TEST CONDITIONS			TIME		SENSOR DATA			
						FRONT		SIDE	
	Tunnel Velocity (kts.)	Liquid Water Content (gm/m^3)	Tunnel Dynamic Pressure (KPa)*	Start HH-MM-SS	Stop HH-MM-SS	Ampl. ρ	Phase Angle	Ampl. ρ	Phase Angle
4-1	0	0	0	19-07-26	19-07-35.9	.109	1.6879	.179	.9416
4-2	146	0	3.22	19-11-06	19-11-20.9	.110	1.6857	.174	.9745
4-3	145	9.4	3.19	19-12-21	19-12-42.9	.063	2.1657	.190	.9512
4-5	97	14.0	1.43	19-17-50	19-18-11.9	.046	2.8317	.226	.9369
4-7	122	14.2	2.25	19-22-30	19-22-52.9	.056	2.3400	.219	.9297
4-8	145	16.3	3.21	19-25-37	19-25-55.9	.064	2.1732	.212	.9346
4-9	169	8.0	4.31	19-28-16	19-28-39.9	.072	2.0573	.196	.9445
4-11	191	7.3	5.50	19-31-37	19-31-58.9	.075	2.0300	.197	.9383
4-13	169	6.7	4.30	19-35-46	19-36-05.9	.0800	1.9782	.201	.9222
4-15	191	6.1	5.49	19-38-45	19-39-06.9	.087	1.9261	.189	.9362
4-16	98	24.5	1.44	19-41-15	19-41-39.9	.048	2.9811	.237	.9177
4-17	0	0	0	19-53-16	19-53-25.9	.1145	1.7114	.187	.9164

(* 1 Pascal = 1 nt/m^2)

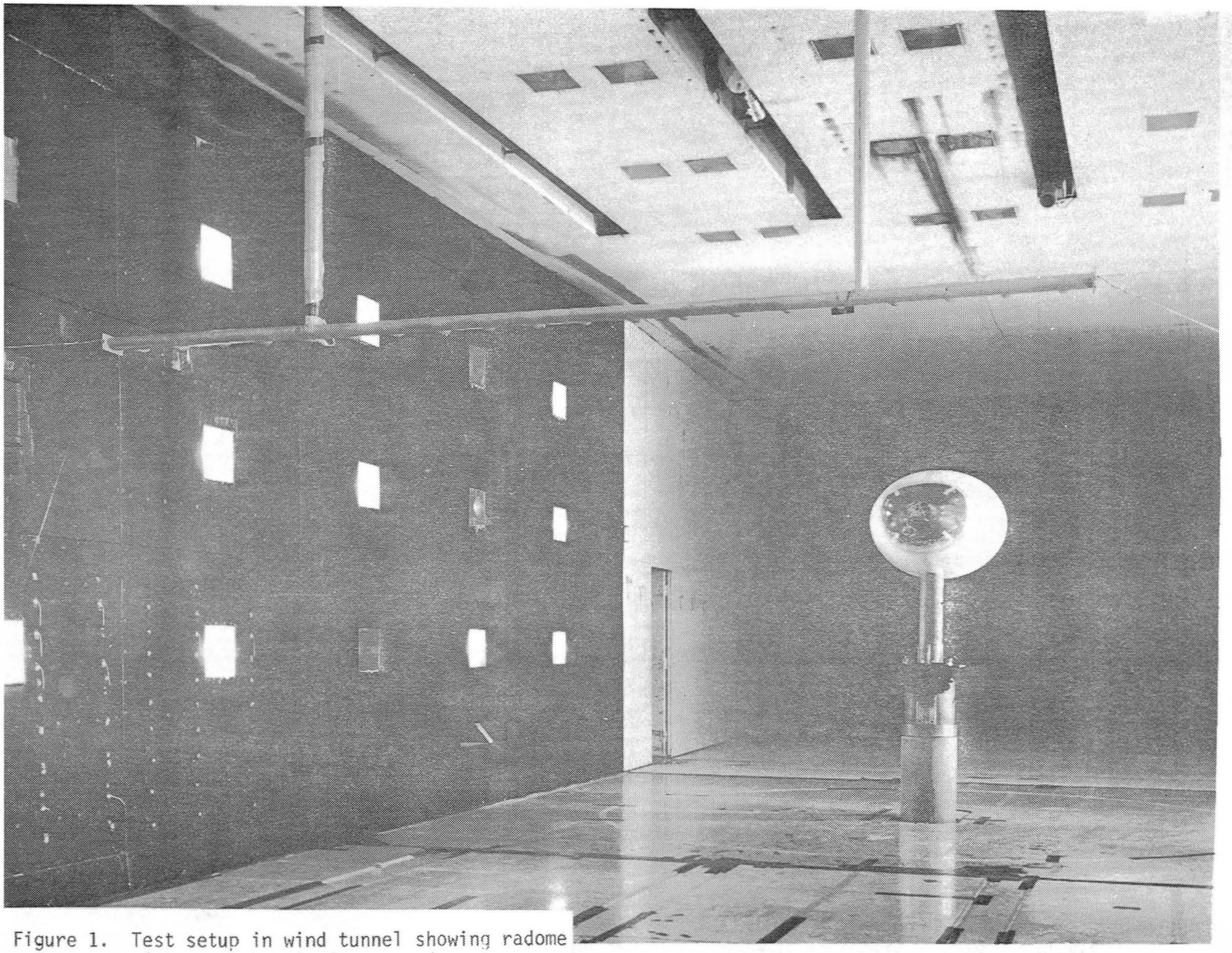

Figure 1. Test setup in wind tunnel showing radome with spray bar in foreground.

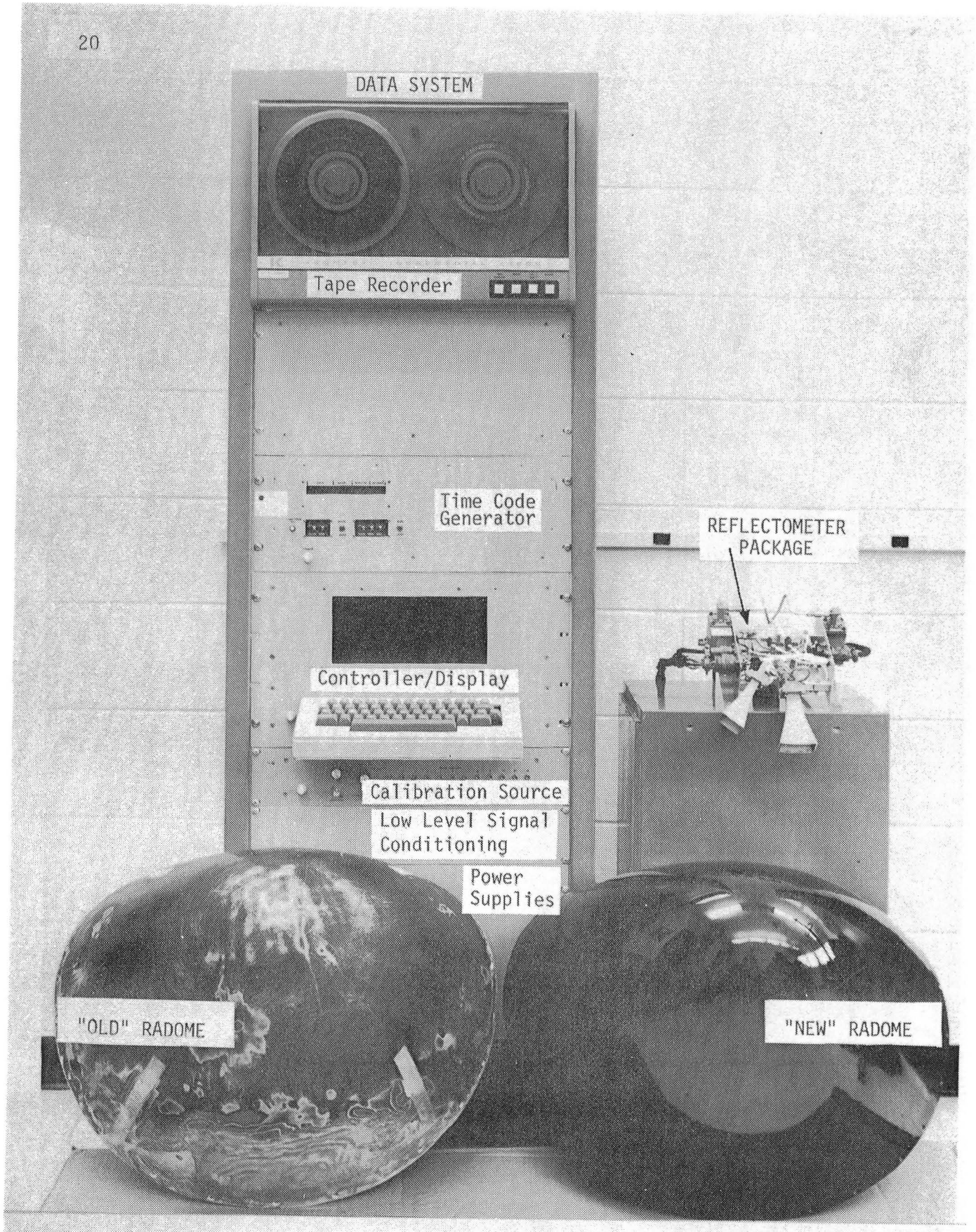

Figure 2. Complete measurement system.

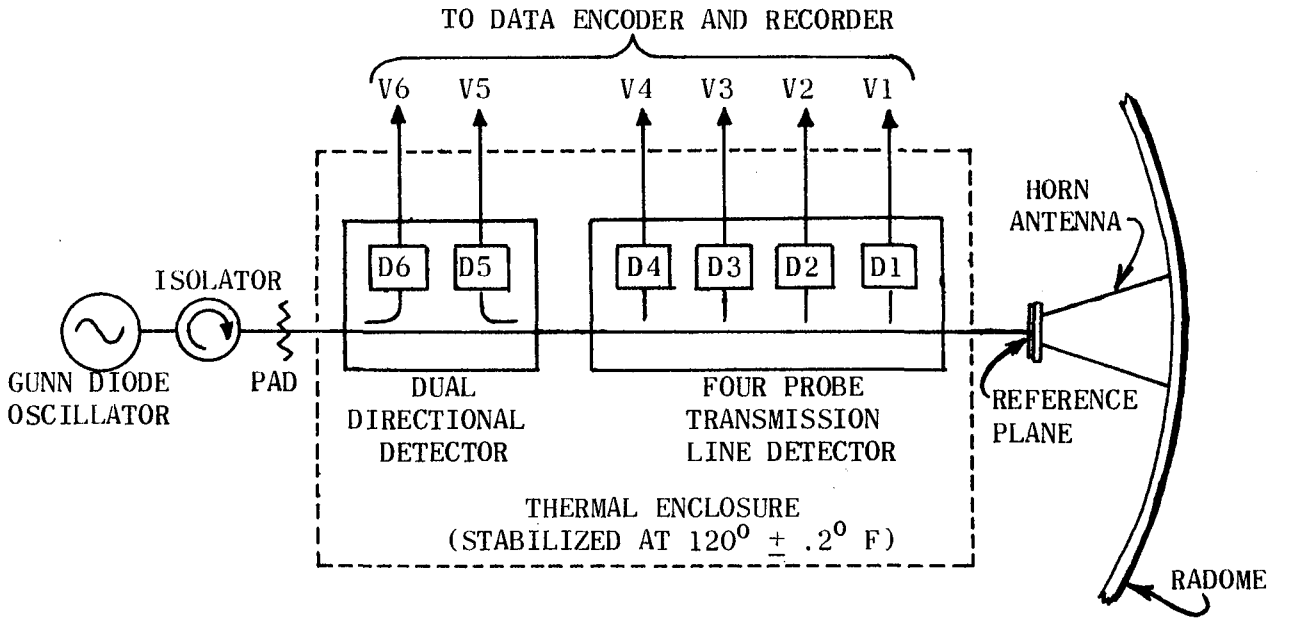

Figure 3. 15 GHz reflectometer system.

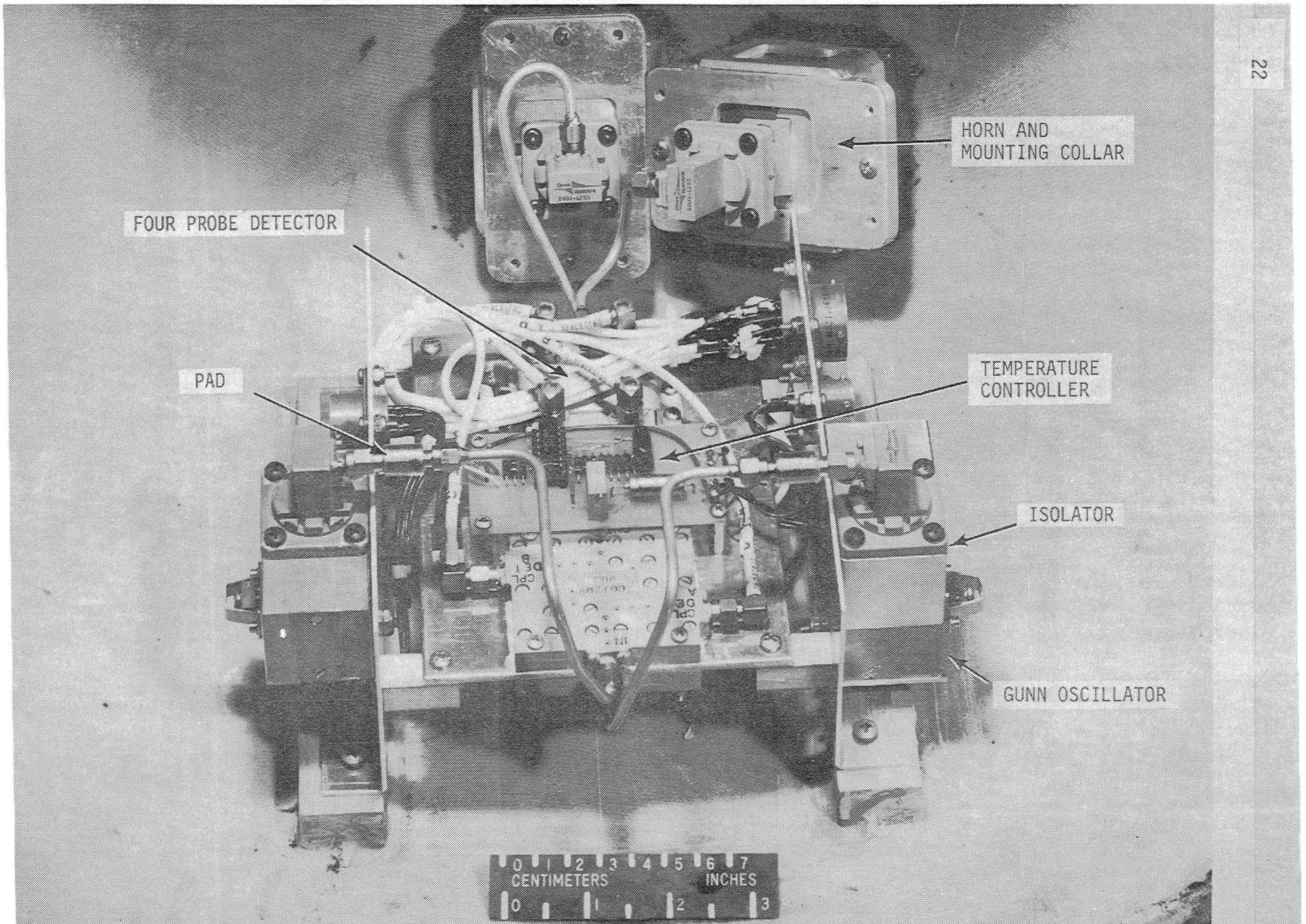

Figure 4. Dual-channel reflectometer.

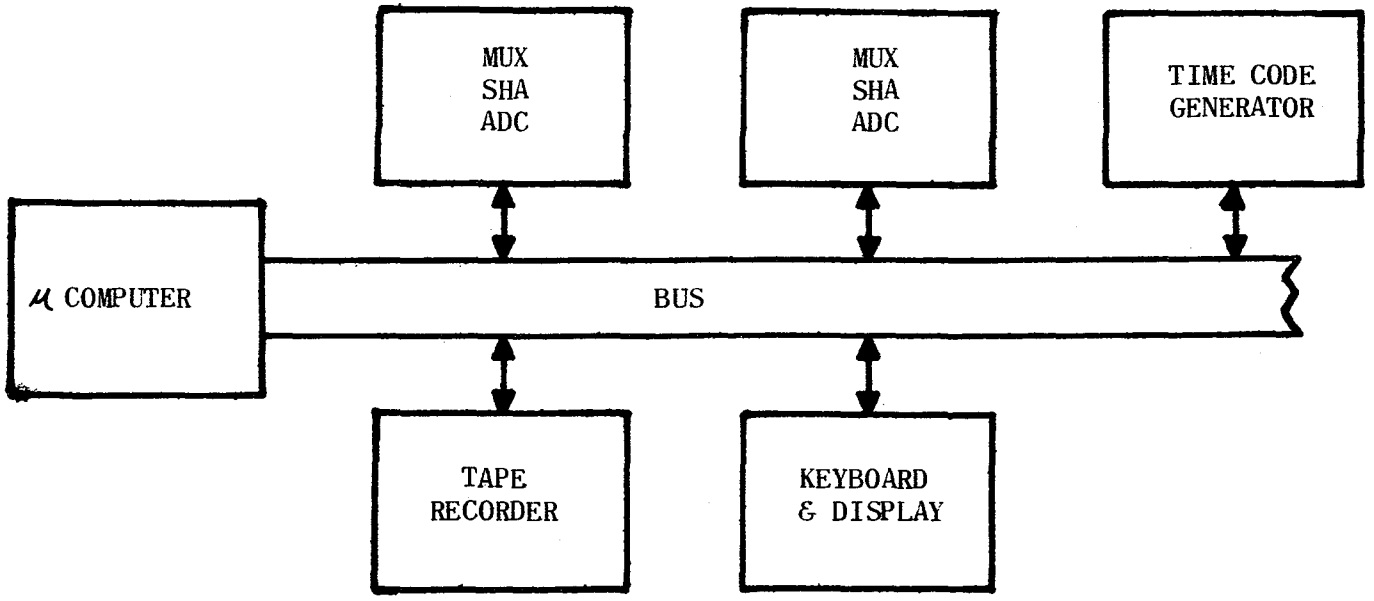

Figure 5. Data acquisition system.

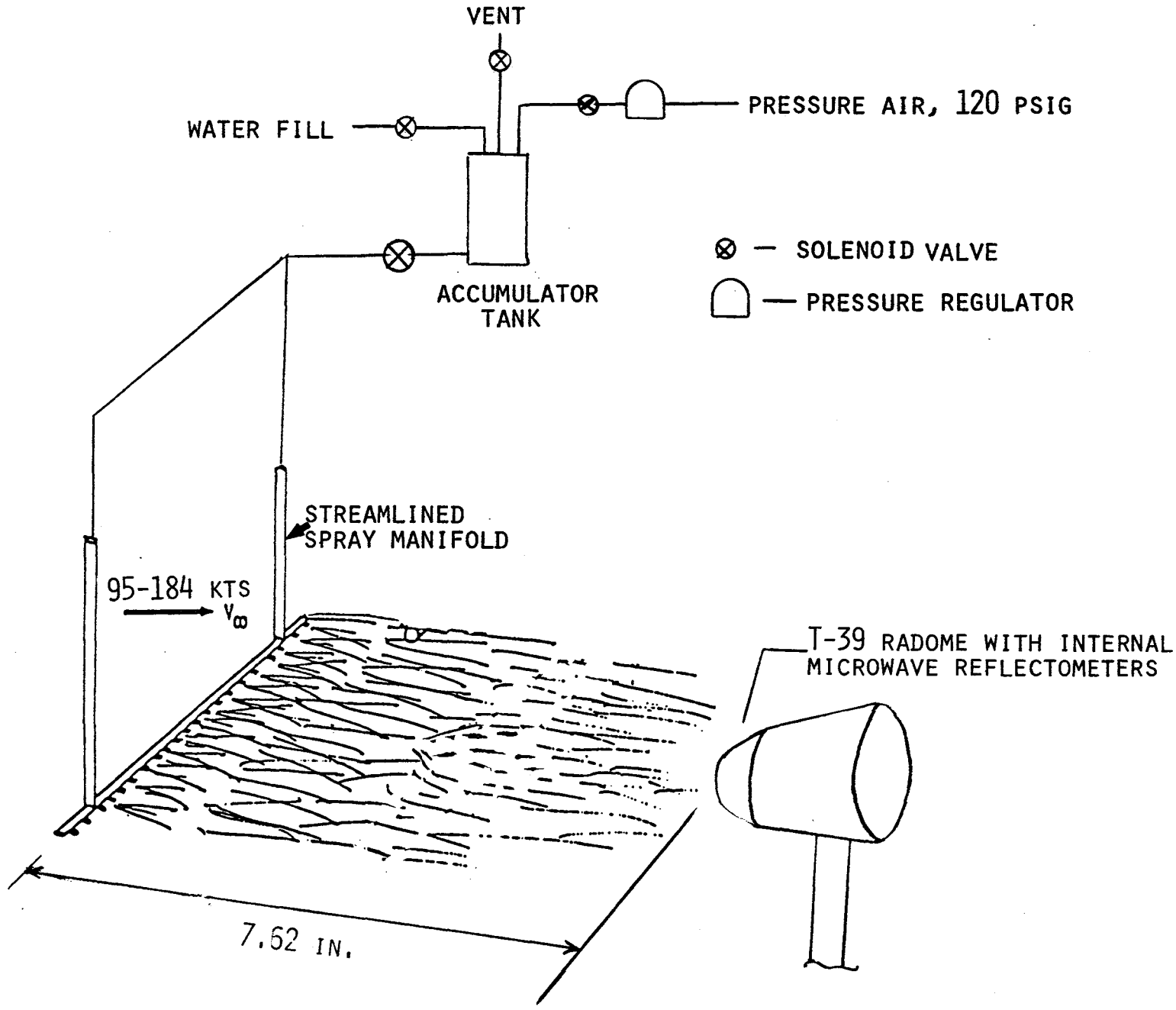

Figure 6. Spray system.

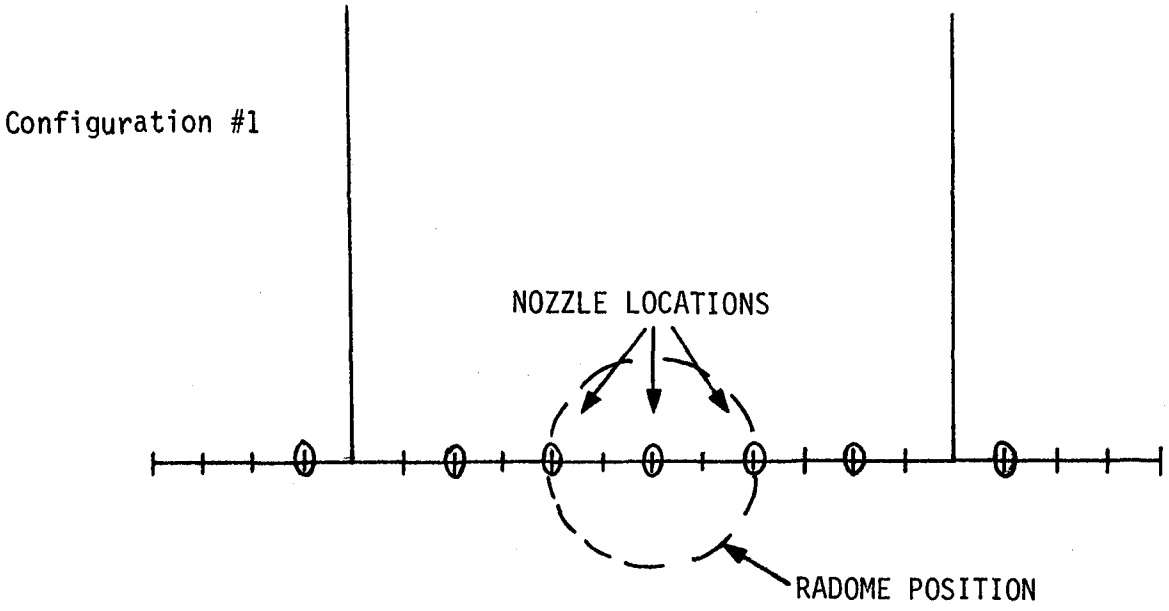

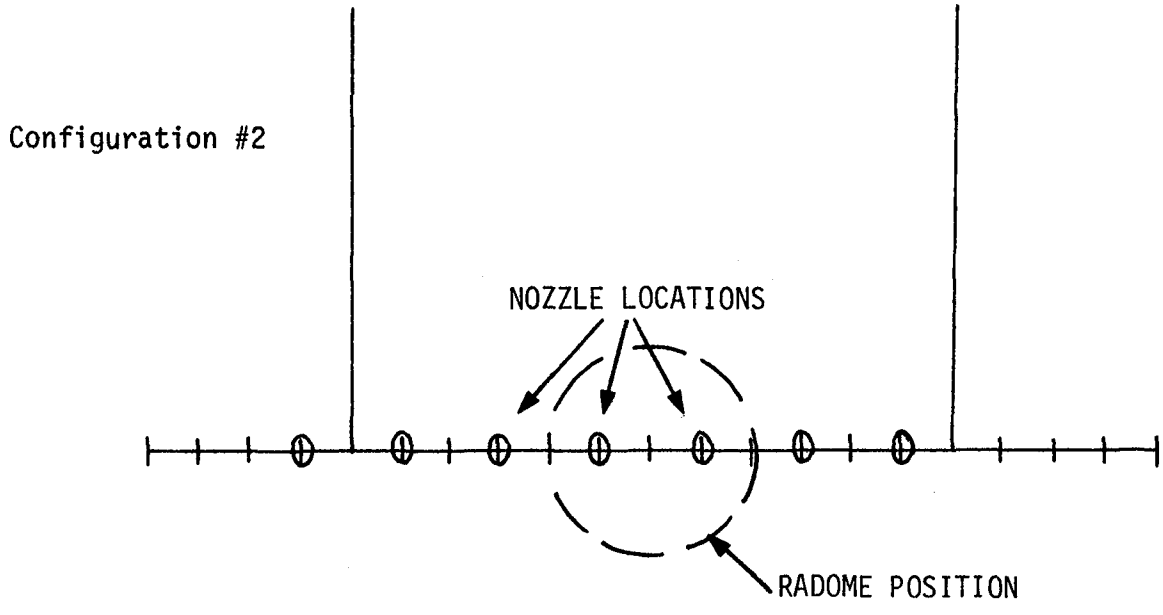

Looking upwind in tunnel at spray rig standing at model.

Figure 7. Nozzle configurations.

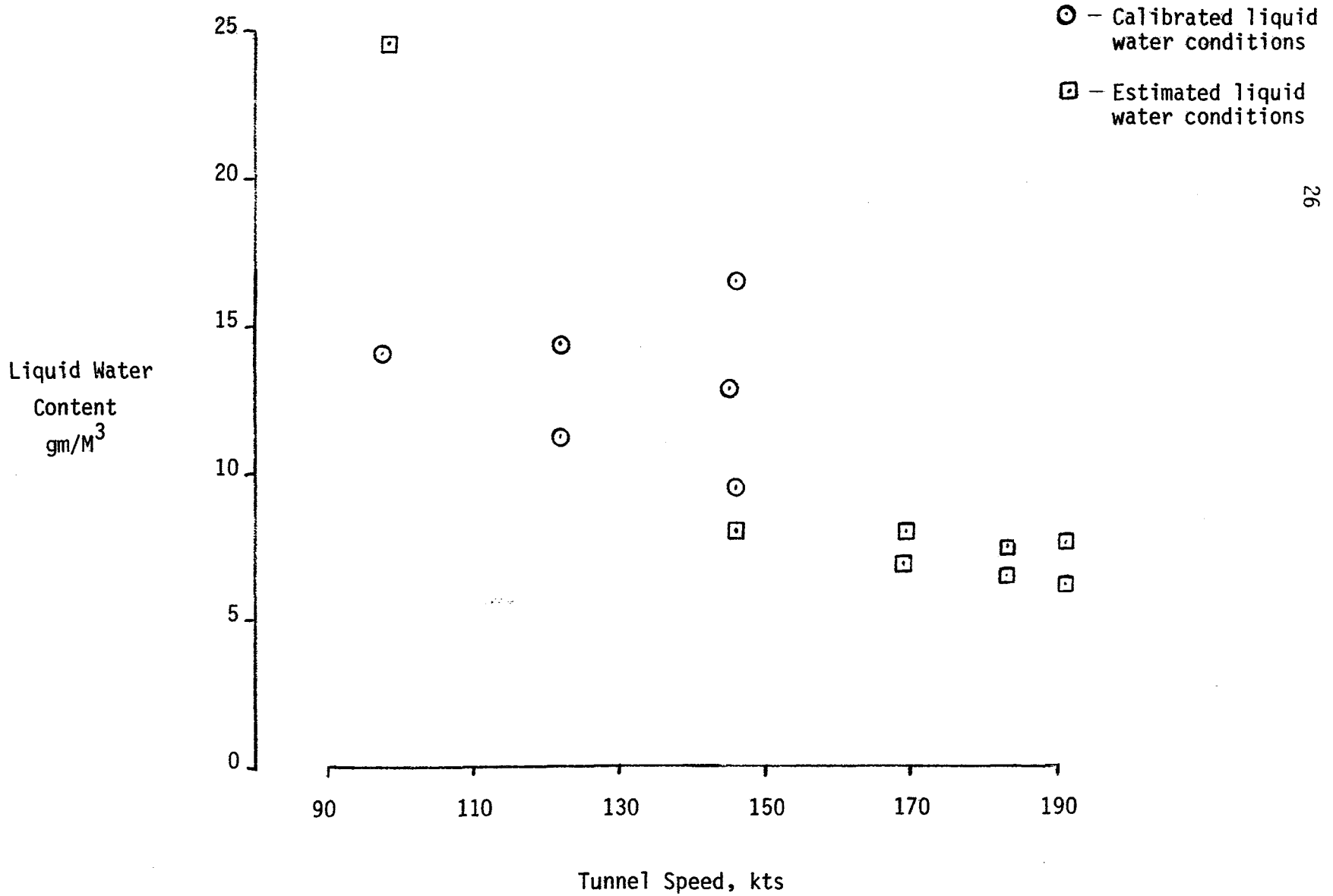

Figure 8. Test conditions of tunnel airspeed versus liquid water content.

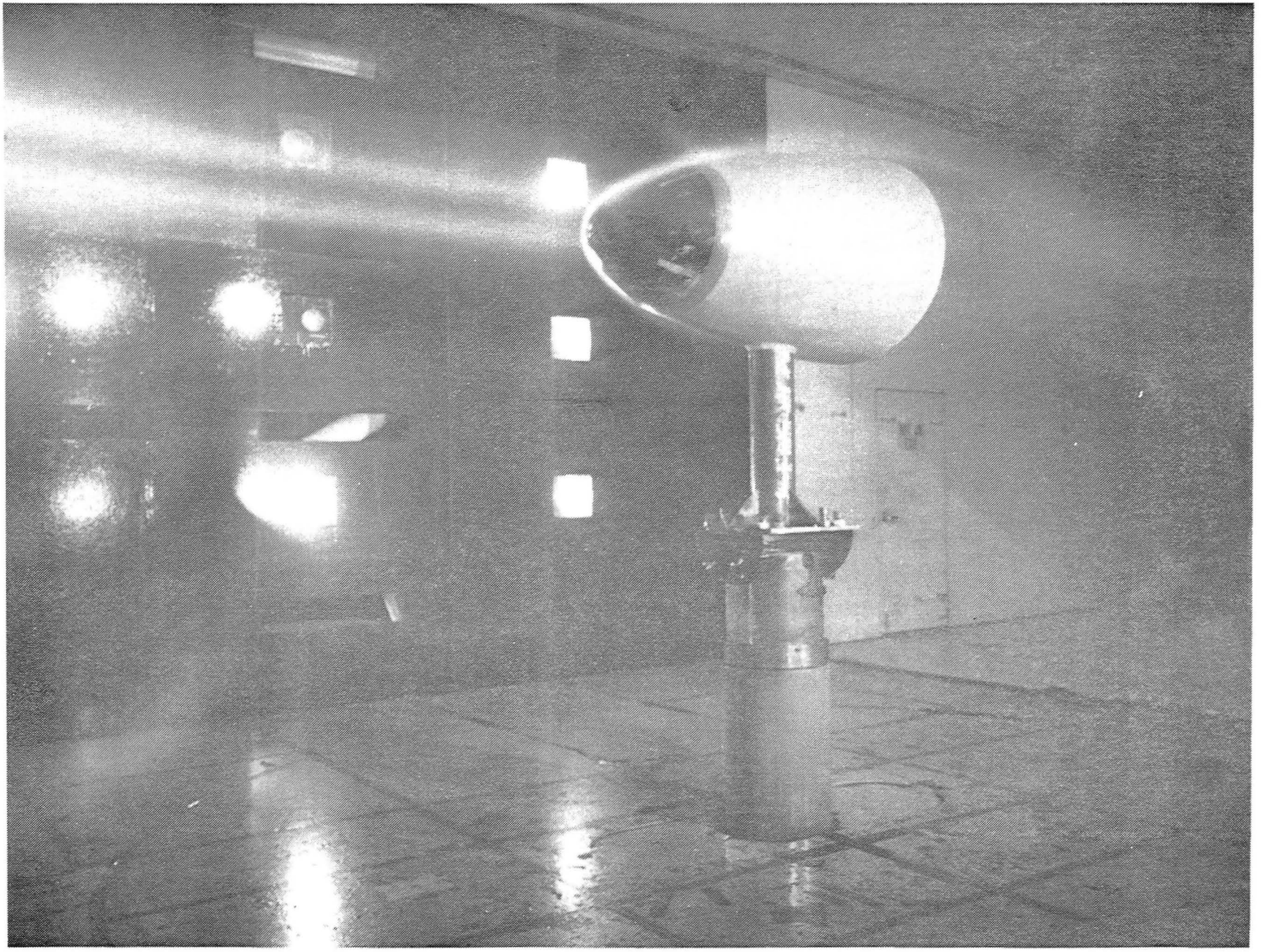

Figure 9. Radome on mounting fixture during wind tunnel test.

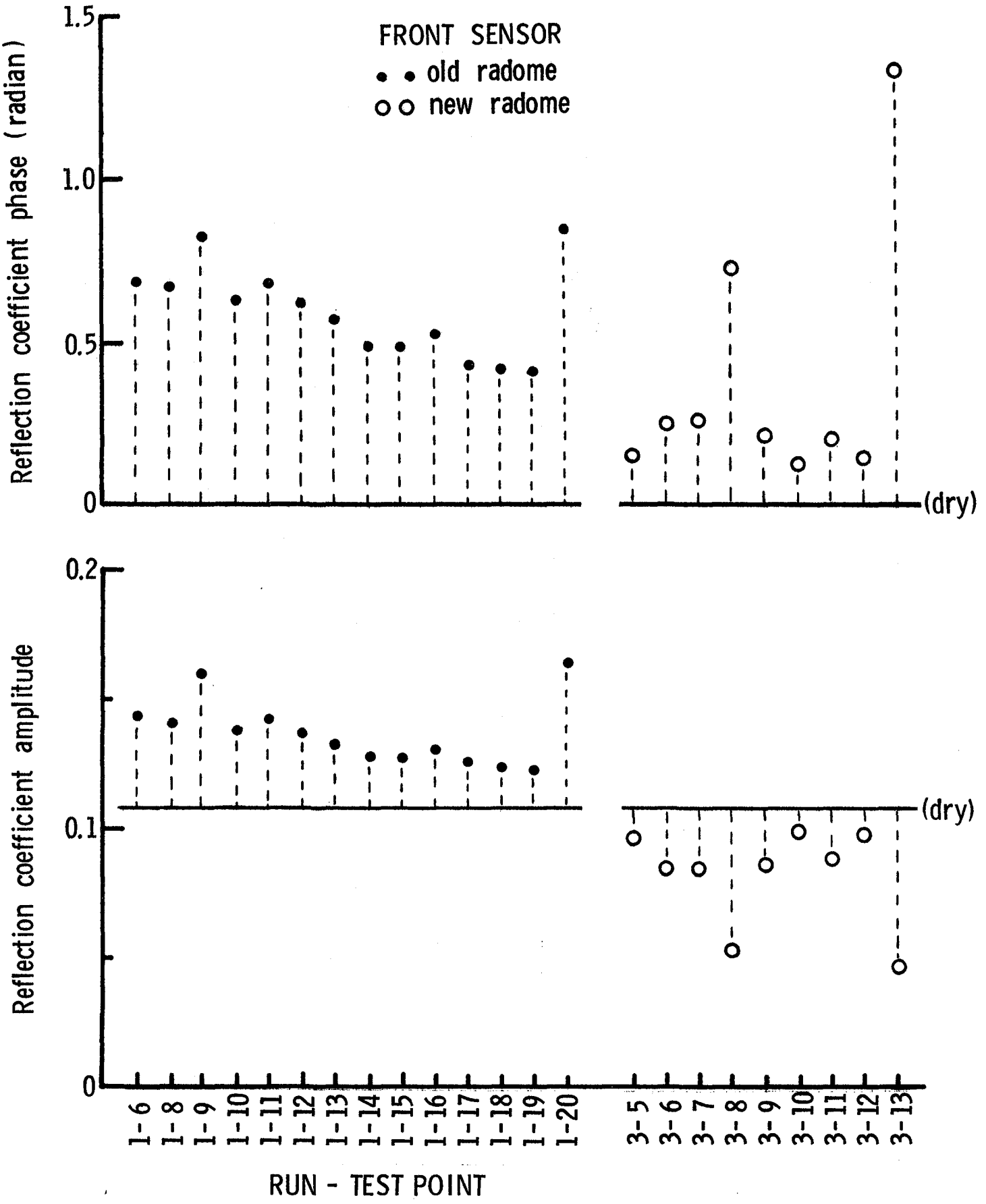

Figure 10. Measured reflection coefficient data for front sensor.

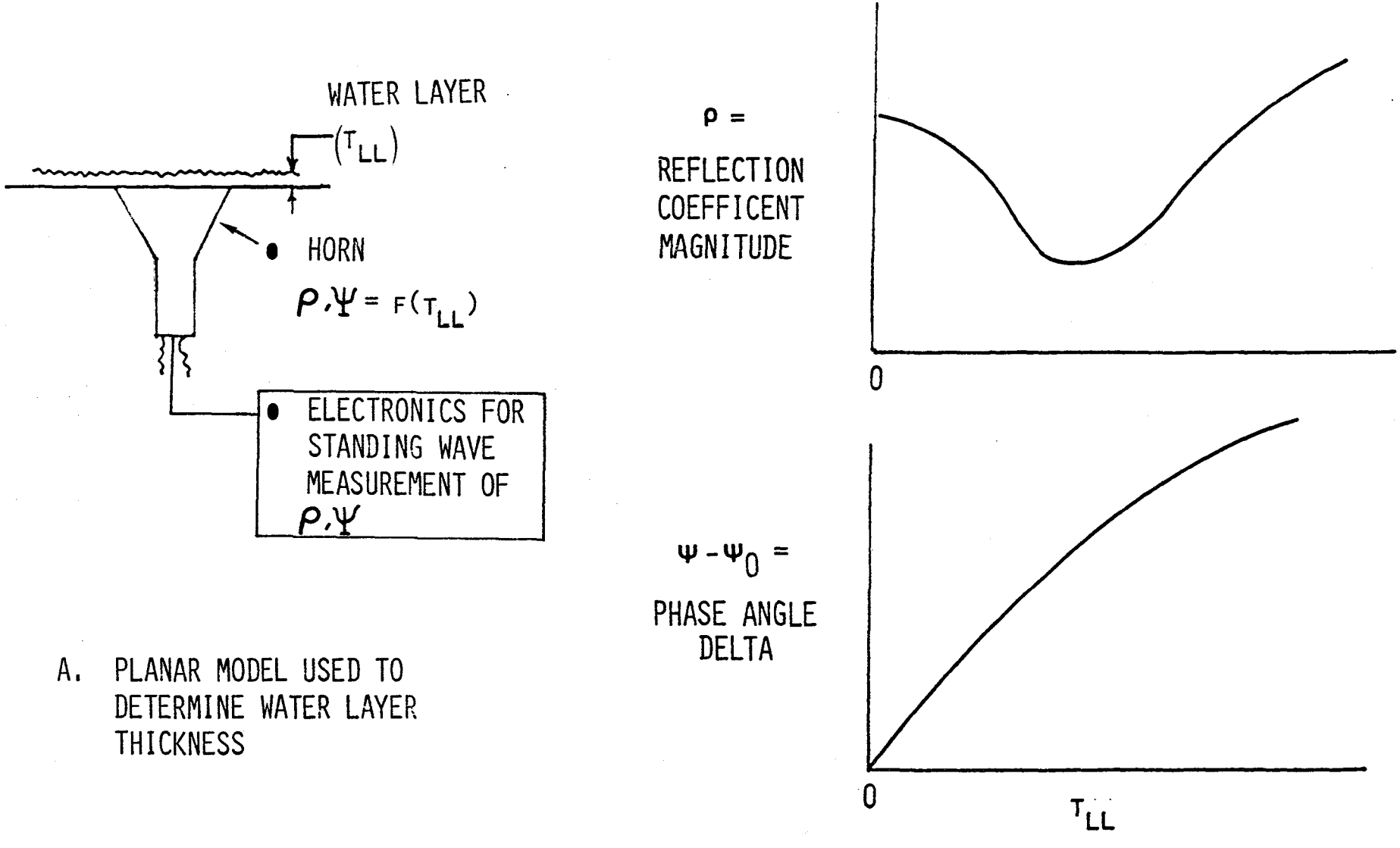

A. PLANAR MODEL USED TO DETERMINE WATER LAYER THICKNESS

B. CHARACTERISTIC CURVES

Figure 11. Planar model of microwave reflectometer.

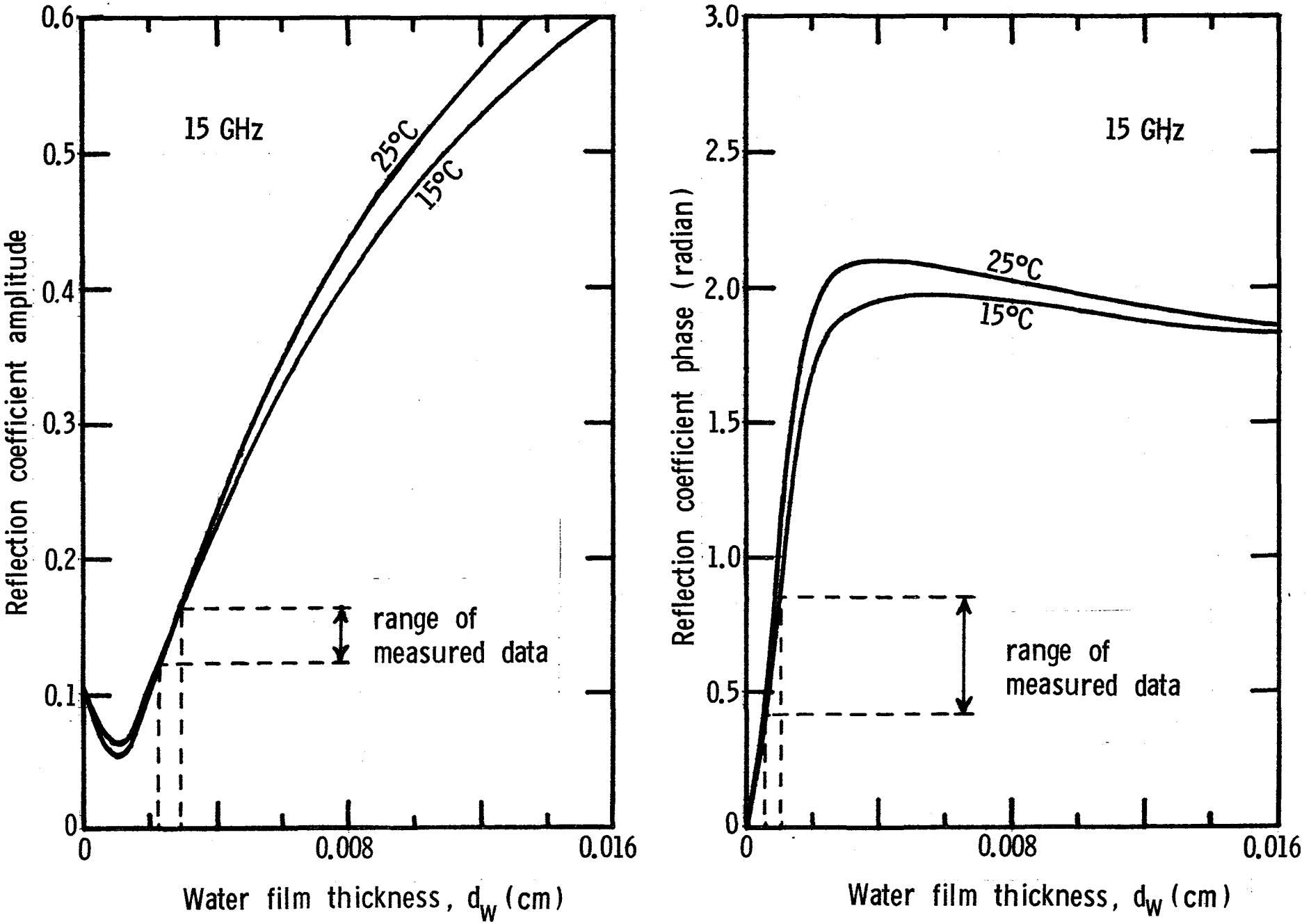

Figure 12. Comparison between plane wave calculation for d_s=0 and measured reflection coefficient for front sensor in "old" radome.

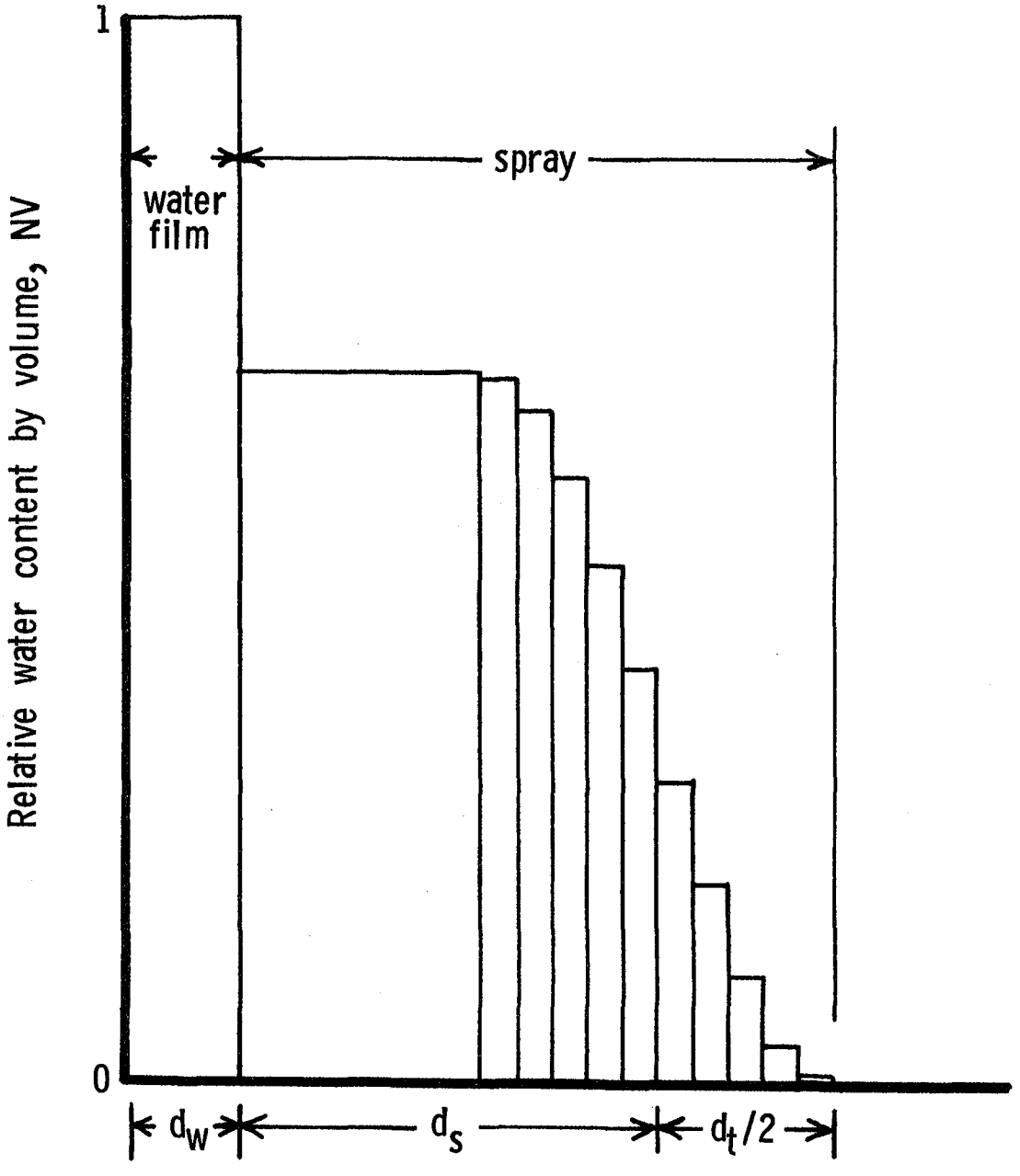

Figure 13. Profile of water film and water spray density for analytical model.

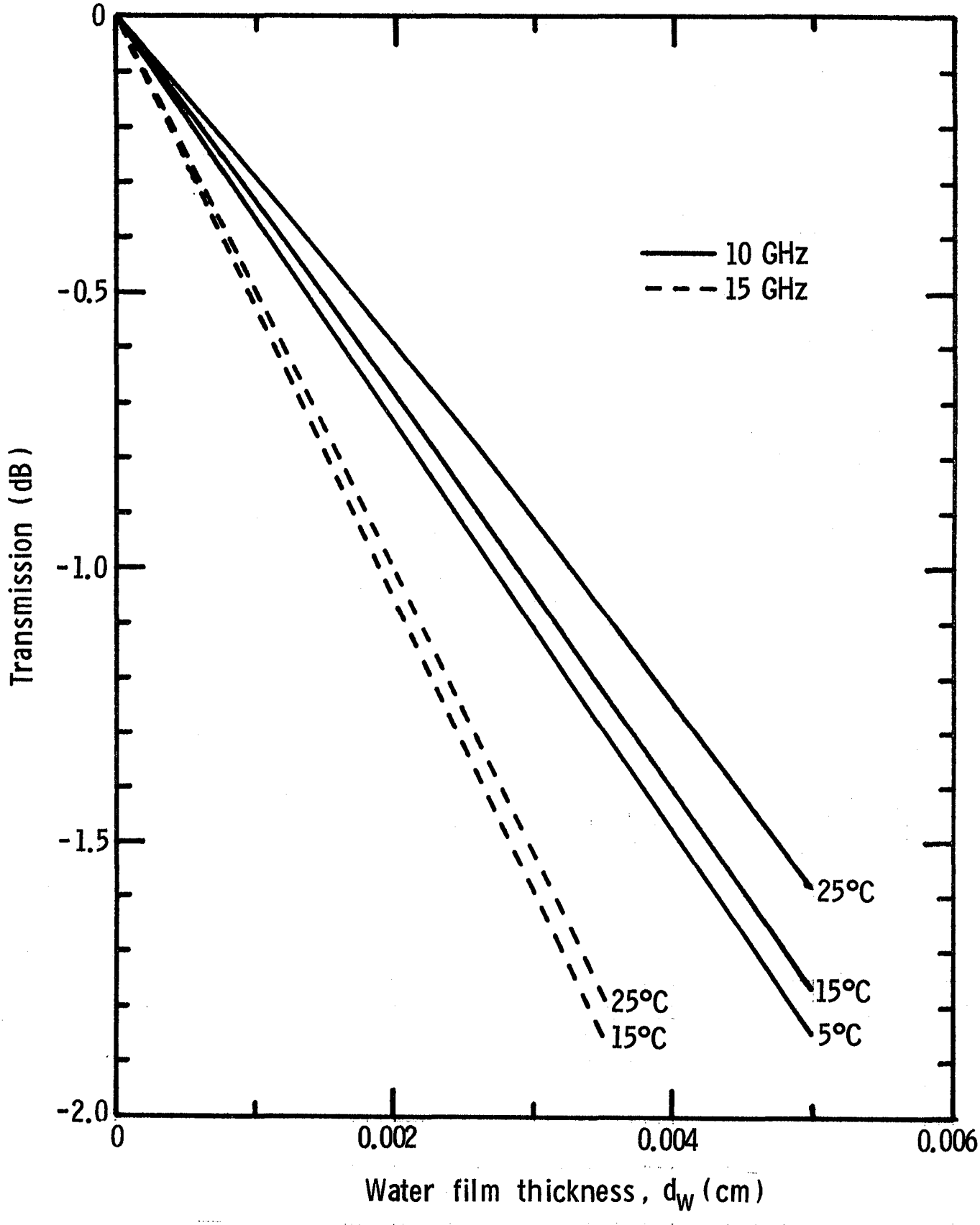

Figure 14. Calculated one-way transmission loss versus water thickness.

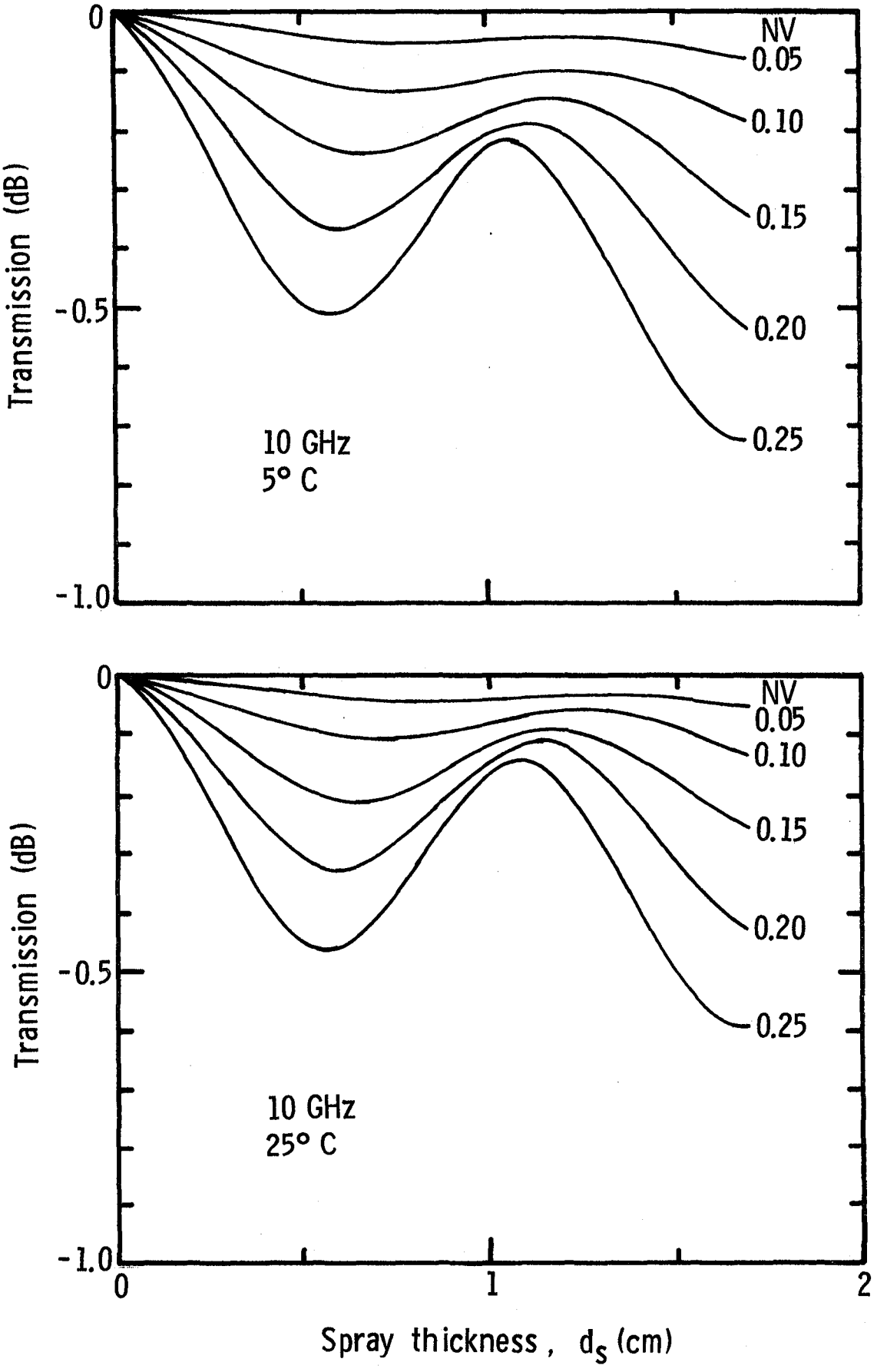

Figure 15. Calculated one-way transmission loss versus uniform spray thickness.

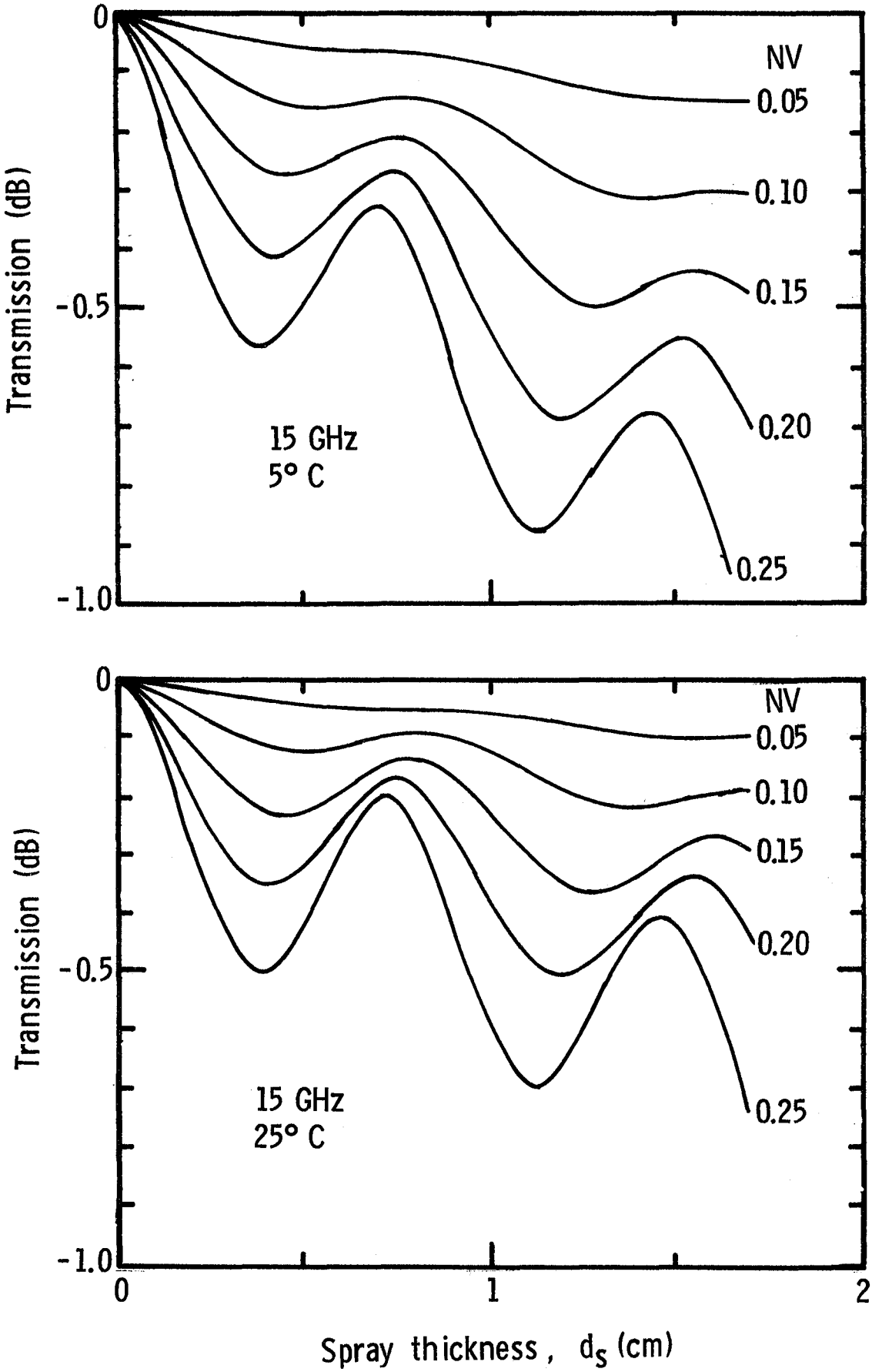

Figure 16. Calculated one-way transmission loss versus uniform spray thickness.

APPENDIX A

ANALYTICAL MODELING

1. ANALYTICAL MODEL - by M. C. Bailey

The analytical modeling of the electromagnetic impedance properties for a horn near a dielectric radome which also has a water film and spray outside is a difficult task and one which has not been formulated at present. In a related problem Knop, et. al. (Ref. 2) solved the boundary value problem in electromagnetics for the impedance of a slot on a dielectric coated cylinder. In order to obtain results from this related problem, one must resort to the numerical evaluation of a quite complicated integral. Extension of the problem to a doubly curved surface with multiple layers becomes more difficult and may not be necessary for the present consideration. Computations using the related cylindrical formulation (Ref. 3) show that an approximation by infinite planar geometry can yield good results for impedance when the cylinder radius is greater than a half-wavelength. Since the impedance of a small slot or horn is predominantly a local field effect, it may be anticipated that a similar conclusion could be drawn concerning the local radius-of-curvature for the doubly curved geometry problem; although this has not yet been shown.

In order to expedite the analysis of measured data from the microwave reflectometer tests, the plane wave reflection from a multilayered dielectric is used as the analytical model to infer water film thickness on the radome. One layer of the dielectric represents the radome and the remaining layers represent the liquid water film plus the water spray outside the radome. The use of the plane wave model instead of the horn is a further simplification

of the analytical problem since the horn problem with a planar dielectric also involves the numerical evaluation of a double integral in order to obtain results. The justification for making this last simplification is demonstrated in figure A-1 in which a comparison is given between the calculated plane wave reflection coefficient and measurements for an X-band waveguide-fed horn radiating into a single plexiglass layer of different thicknesses.

The analytical expressions for plane wave reflection and transmission for a plane dielectric layer can be found in most text books on electromagnetic theory. The analytical model used in this report follows the procedure given by Richmond (Ref. 4) in which the reflection and transmission coefficients are evaluated through recursive equations for the complex amplitudes of the standing wave within each layer of a multilayer lossy dielectric.

Figure A-2 illustrates a plane wave of amplitude A_0 incident on a dielectric with I number of layers and with a reflected amplitude B_0. In order to facilitate the analysis, incident and reflected plane waves of amplitudes B_{I+1} and A_{I+1} are assumed at the outer surface of the multilayered dielectric. In the analysis, the electric field vector is assumed to be x-directed. The incident, reflected, and transmitted electric field components for the multilayer dielectric are expressed in the traveling wave form as

$$E_x^i = A_0 e^{-jk_0 z} \tag{1.1}$$

$$E_x^r = RA_0 e^{jk_0 z} \tag{1.2}$$

$$E_x^t = TA_0 e^{-jk_0 z} \tag{1.3}$$

where R and T are the plane wave reflection and transmission coefficients for the multilayer dielectric and k_o is the free space propagation constant. The electric and magnetic fields within each layer can be represented as the superposition of waves traveling in opposite directions. In layer (i) these are written as

$$E_x = A_i e^{-jk_o z\sqrt{\varepsilon_i}} + B_i e^{jk_o z\sqrt{\varepsilon_i}} \tag{1.4}$$

$$H_y = \frac{\sqrt{\varepsilon_i}}{120\pi}\left[A_i e^{-jk_o z\sqrt{\varepsilon_i}} - B_i e^{jk_o z\sqrt{\varepsilon_i}}\right] \tag{1.5}$$

where ε_i is the complex dielectric constant of the i-th layer. Applying boundary conditions for the electromagnetic fields at the interface ($z = z_i$) between layers i and i + 1 and solving for A_i and B_i in terms of A_{i+1} and B_{i+1}, gives the recursive equations

$$2A_i = \left(1 + \sqrt{\varepsilon_{i+1}}/\sqrt{\varepsilon_i}\right) A_{i+1} e^{-jk_o z_i}\left(\sqrt{\varepsilon_{i+1}} - \sqrt{\varepsilon_i}\right) + \left(1 - \sqrt{\varepsilon_{i+1}}/\sqrt{\varepsilon_i}\right) B_{i+1} e^{jk_o z_i}\left(\sqrt{\varepsilon_{i+1}} + \sqrt{\varepsilon_i}\right) \tag{1.6}$$

$$2B_i = \left(1 - \sqrt{\varepsilon_{i+1}}/\sqrt{\varepsilon_i}\right) A_{i+1} e^{-jk_o z_i}\left(\sqrt{\varepsilon_{i+1}} + \sqrt{\varepsilon_i}\right) + \left(1 + \sqrt{\varepsilon_{i+1}}/\sqrt{\varepsilon_i}\right) B_{i+1} e^{jk_o z_i}\left(\sqrt{\varepsilon_{i+1}} - \sqrt{\varepsilon_i}\right) \tag{1.7}$$

Now if we set

$$A_{I+1} = 1 \tag{1.8}$$

$$B_{I+1} = 0 \tag{1.9}$$

then the reflection and transmission coefficients become

$$R = B_o/A_o \tag{1.10}$$

$$T = 1/A_o \tag{1.11}$$

where the values of A_o and B_o are found through the recursive equations. This calculation is generally carried out with the aid of a digital computer.

The water film is modeled as a dielectric layer by using the Debye expression for the dielectric constant (ε_w) of distilled water after being empirically adjusted by Klein and Swift (Ref. 5) as

$$\varepsilon_w = \varepsilon' - j\varepsilon''$$

$$= 4.9 + (1-j\omega\tau)\left[\frac{\varepsilon_o - 4.9}{1 + (\omega\tau)^2}\right] \tag{1.12}$$

where the static value (ε_o) is given by

$$\varepsilon_o = 88.045 - 0.414C + 6.295 \times 10^{-4}C^2 + 1.075 \times 10^{-5}C^3 \tag{1.13}$$

and the relaxation time (τ) is

$$\tau = 1.768 \times 10^{-11} - 6.086 \times 10^{-13}C + 1.104 \times 10^{-14}C^2 - 8.111 \times 10^{-17}C^3 \quad (1.14)$$

where C is the temperature of the water in degrees centigrade and ω is the frequency of the electromagnetic wave in radians per second.

The spray outside the radome and water film is represented as a multi-layer dielectric in which the complex dielectric constant of each layer is expressed as a function of the relative volume density of water in the spray. This expression assumes small particle scattering theory (Ref. 6, p. 38) applies to the droplets in the spray and further assumes homogeneous spheres (Ref. 6, p. 70) for the droplets. Under these assumptions, the equivalent dielectric constant (ε_s) for the water spray can be written in the form

$$\varepsilon_s = \left[(1+1.5NV\beta')^2 - (1.5NV\beta'')^2\right] - j\left[3NV\beta''(1+1.5NV\beta')\right] \quad (1.15)$$

where NV is the relative volume density of liquid water in the spray, and

$$\beta' = \frac{(\varepsilon'-1)(\varepsilon'+2) + (\varepsilon'')^2}{(\varepsilon'+2)^2 + (\varepsilon'')^2} \quad (1.16)$$

$$\beta'' = \frac{3\varepsilon''}{(\varepsilon'+2)^2 + (\varepsilon'')^2} \quad (1.17)$$

By estimating the volume density of the spray and the water temperature, these expressions can be used with the recursive equations to calculate the reflection and transmission coefficients. The thickness of the water film on the radome is inferred through a comparison between the measured and calculated reflection coefficient amplitude and phase.

APPENDIX A

ANALYTICAL MODELING

2. MEASUREMENT TECHNIQUE AND INTERPRETATION - by C. P. Hearn

Determination of the water layer thickness requires a knowledge of the feedpoint impedance variations under test conditions. This was accomplished by making standing wave measurements at multiple points along the feedline, preceeding the antenna, and then calculating the feeding point impedance (or complex reflection coefficient).

Historically, the determination of impedance, or alternately the complex reflection coefficient, has been based on the use of the Smith chart (Ref. 7 and 8); however, in this experiment the volume of data to be evaluated made computer-aided data reduction mandatory. The complex reflection coefficient, Γ, was determined by a curve-fitting routine in which the magnitude and phase of Gamma (ρ and ψ) were picked to minimize the sum of the mean square deviations between the measured data points and theoretical values based on the mathematical model shown in figure A-3. Note that in this model, the direction of propagation is in the negative X direction.

The actual Ku-band impedance measurement system, described more fully in Section II-B, used a four-probe stripline with built-in diode envelope detectors to provide the primary data, with a dual directional detector providing a "quick-look", scalar indication of the complex reflection coefficient. Referring to figure A-3, the forward voltage wave $v_F(X)$ referenced to its value at X_1 may be expressed as

$$v_F(X) = V_{F1}\, e^{\alpha(X-X_1)}\, e^{j\beta(X-X_1)}, \quad X_1 \leq X \leq X_4 \tag{2.1}$$

where $\gamma = \alpha - j\beta$ is the complex wave propagation constant.

The reverse voltage wave $v_R(X)$ is expressible as

$$v_R(X) = \rho v_F(X)\, e^{-2\alpha(X-X_1)}\, e^{-2\alpha X_1}\, e^{j2\beta(X-X_1)}\, e^{j2\beta X_1}\, e^{j\psi} \tag{2.2}$$

The voltage $v(x)$ at any point along the line is the vector sum of $v_F(X)$ and $v_R(X)$, or

$$v(X) = v_F(X)\left[1 + \rho T^2\, e^{-2\alpha(X-X_1)}\, e^{j2\beta(X-X_1)}\, e^{j2\beta X_1}\, e^{j\psi}\right] \tag{2.3}$$

where the two-way cable loss term, $e^{-2\alpha X_1}$ in Equation 2.2, is replaced by T^2. The voltage produced by a square-law (diode) detector located at X is

$$V(X) = K(X)|v(X)|^2 \tag{2.4}$$

where $K(X)$ is the detector gain constant. Combining Equations (2.3) and (2.4) leads to

$$V(X) = K(X)|v_F(X)|^2 \cdot \left[1 + \rho T^2\, e^{-2\alpha(X-X_1)}\, e^{j2\beta(X-X_1)} \cdot e^{j2\beta X_1}\, e^{j\psi}\right]^2 \tag{2.5}$$

combining Equations 2.1 and 2.5 gives

$$V(X) = K(X)V^2_{F1}\, e^{2\alpha(X-X_1)}\left[1 + \rho T^2\, e^{-2\alpha(X-X_1)}\, e^{2\beta(X-X_1)}\, e^{j2\beta X_1}\, e^{j\psi}\right]^2 \tag{2.6}$$

To obtain the desired relationship for the individual probe voltages, V_i, the 4 distinct values of X_i (X_1 through X_4) are combined with the multiplicative constants of the squared magnitude into one constant to give

$$V_i = K_i \left[1 + \rho T^2 e^{-2\alpha\Delta X_i} e^{j2\beta\Delta X_i} e^{j2\beta X} e^{j\psi}\right]^2 , \quad i = 1 \text{ to } 4 \qquad (2.7)$$

The unknowns in Equation 2.7 are ρ and ψ; the remaining parameters are determined through the following calibration procedure which provides a measurement of the unknown parameters. The unknown impedance (i.e. the microwave horn/radome interface) was replaced with a micrometer-controlled sliding short to generate the set of curves illustrated in figure A-4 in which the 4 probe voltages are plotted with respect to the displacement of the sliding short from the reference plane ($X = 0$). Channel gains (K_i) were set so that all channels produced approximately equal maximum values. The sliding short was replaced with a fixed short at $X = 0$. The measured values of the output voltages of the detectors, under this condition, were located on the curves of figure A-4, thereby establishing the location of the reference plane (to an ambiguity of $\lambda/2$). The sample points, X_i, were obtained by measuring their displacement in wavelengths from the reference plane.

The line loss between the reference plane and the i^{th} sensor was determined indirectly using the standing wave ratio definition. Referring to Equation 2.7, the ratio of maximum and minimum values of V_i was determined and the loss term computed yielding

$$Te^{-\alpha\Delta X_i} = \left\{ \frac{\left(\frac{V_i \text{ max.}}{V_i \text{ min.}}\right) - 1}{\left(\frac{V_i \text{ max.}}{V_i \text{ min.}}\right) + 1} \right\}^{1/2} \tag{2.8}$$

Experimental results indicated that the incremental loss, $e^{-\alpha\Delta X_i}$, was small enough to justify neglecting it, and assuming $\alpha = 0$.

Finally, the K_i were selected so that Equation 2.7 had the same maximum values as were measured in figure A-4. These data are tabulated in Table A-1.

APPENDIX A

ANALYTICAL MODELING

3. PARAMETER ESTIMATION - by C. P. Hearn

The data reduction task was to determine the values of ρ and ψ that minimized the error between the four data points, $\hat{V}_1$ through $\hat{V}_4$, and the theoretical relationship of Equation 2.7. The function to be minimized was defined as:

$$ERF = \sum_{i=1}^{4} (v_i - \hat{V}_i)^2 \tag{3.1}$$

Equation 3.1 was minimized with the finite-difference, Levenberg-Marquardt Algorithm (called Marguardt's Compromise in Ref. 9). This algorithm demonstrates excellent convergence properties. Additionally, it is available from the International Mathematical and Statistical Libraries (IMSL) version 9.0 software package (Ref. 10) and hence required a minimal amount of programming effort. A full description of the method may be found in reference 11.

Implementation of this algorithm produced surprisingly small values for the sum of the squared errors. On the average, this value was .017 over 122 data sets. The average amount of computer time required to implement the algorithm was .0679 cpu seconds per data set, with each execution requiring approximately 8 iterations to converge.

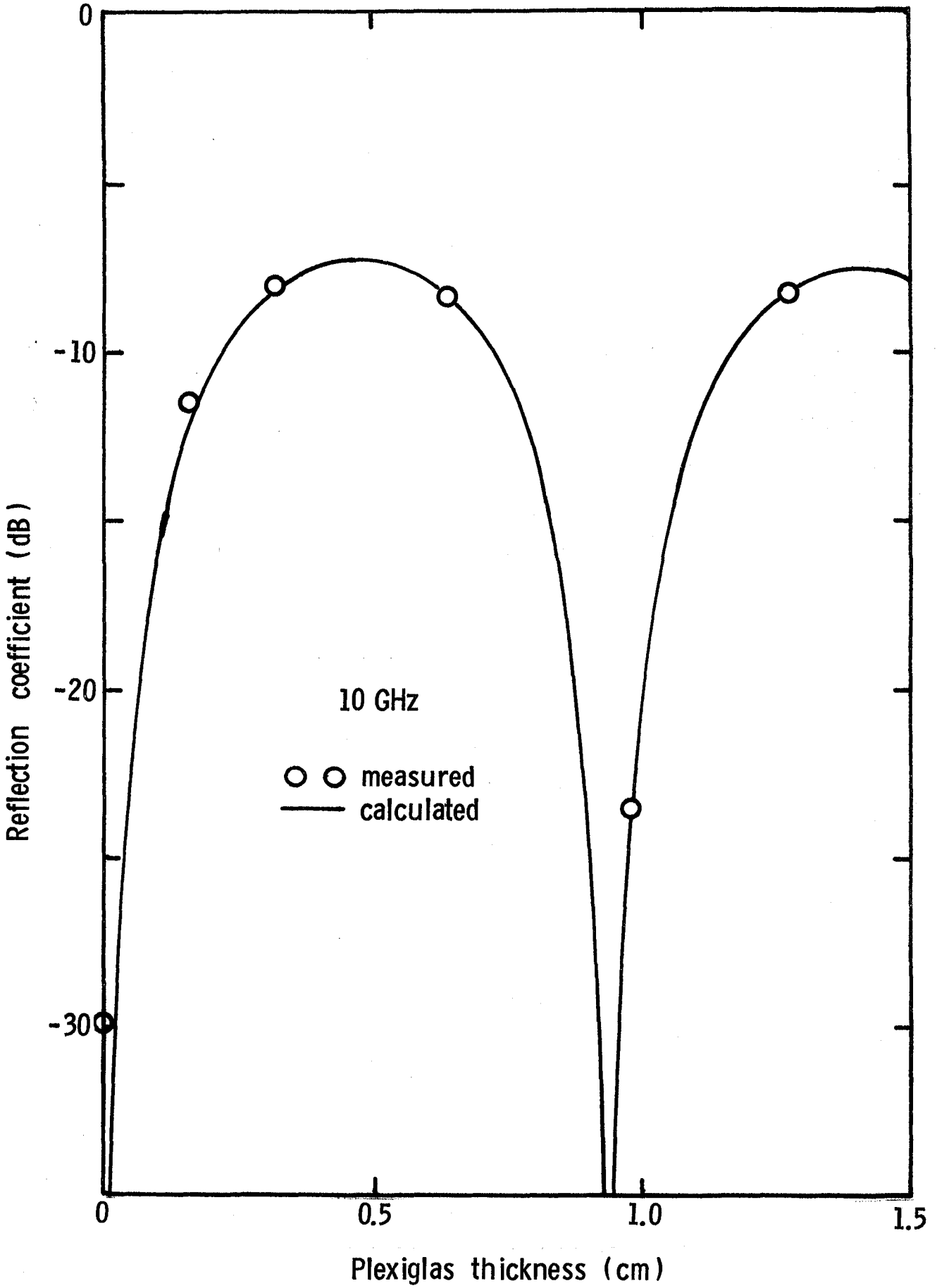

Figure A-1. Comparison between measured and calculated reflection coefficient for X-band horn with plexiglas cover.

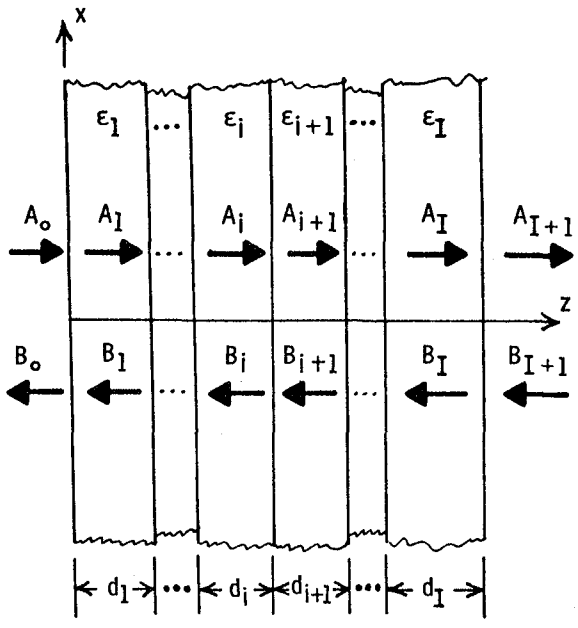

Figure A-2. Multilayer dielectric geometry for plane wave analysis.

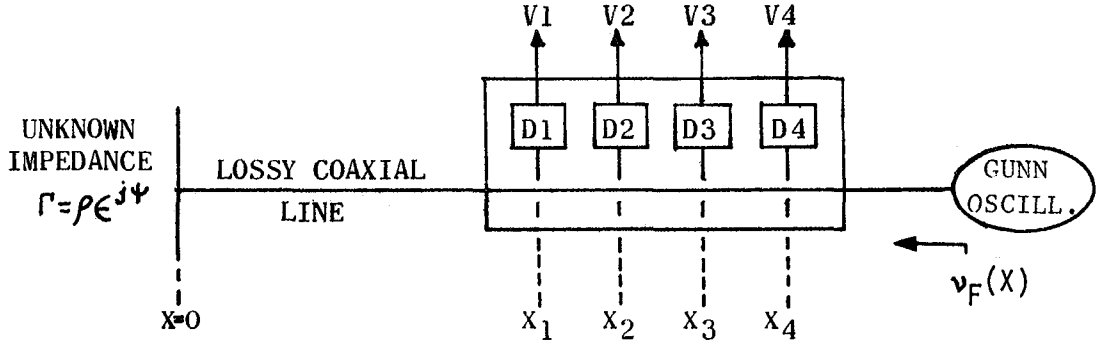

Figure A-3. Configuration for mathematical modeling.

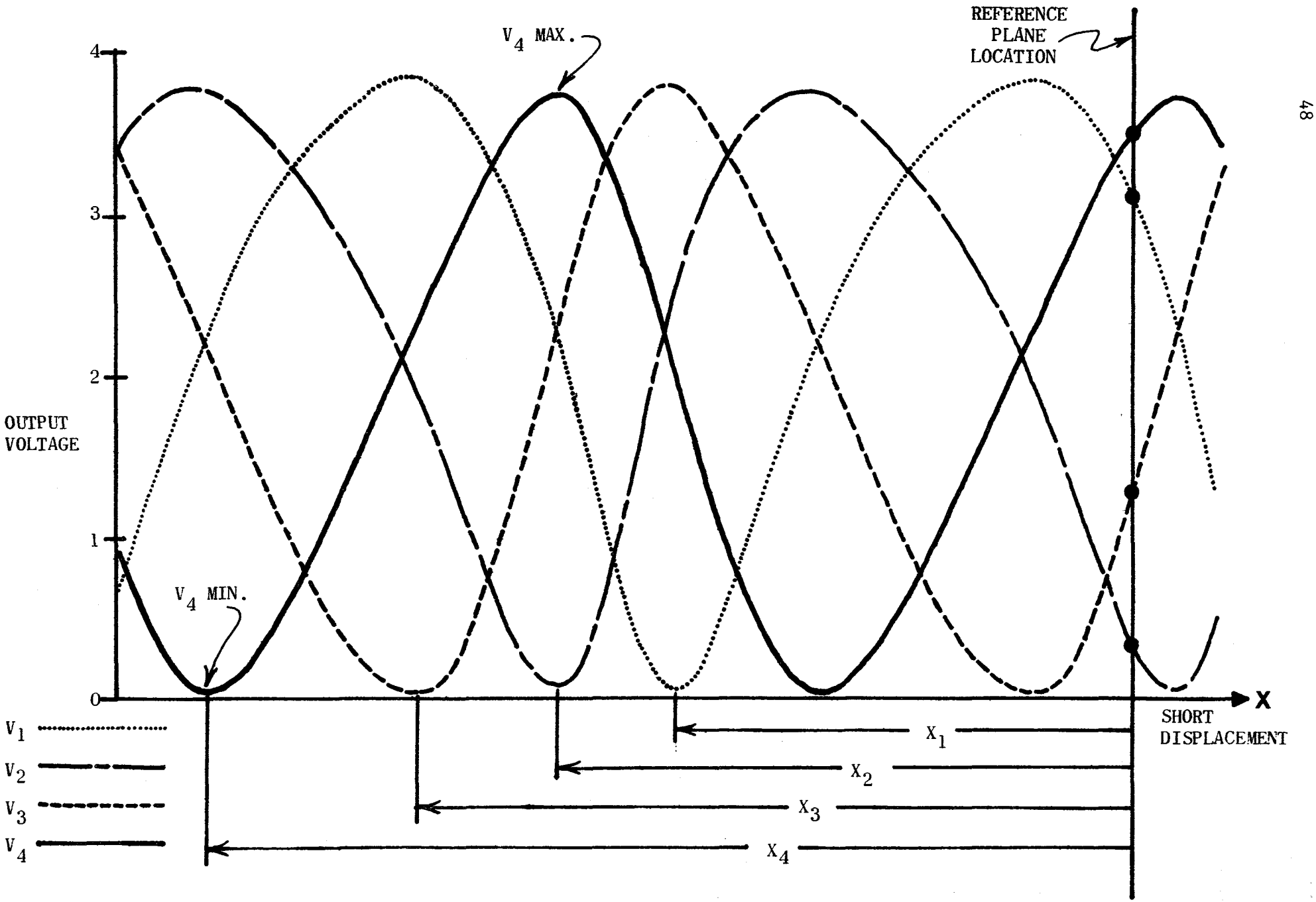

Figure A-4. Sliding-short calibration curves.

Table A-1. Experimentally measured constants.

PARAMETER	SIDE SENSOR	FRONT SENSOR
X_1	.3763λ	.21875λ
ΔX_i	.0930λ	.11405λ
ΔX_2	.2122λ	.2084 λ
ΔX_3	.3280λ	.3229 λ
T^2	.851	.852
K_1	1.100	1.067
K_2	1.086	1.067
K_3	1.103	1.079
K_4	1.074	1.085

APPENDIX B

MEASURED REFLECTION COEFFICIENT DATA

The reflection coefficient determined from the reflectometer four-probe data is presented in this appendix as plots of amplitude and phase versus time during each test run. The data for the "old" radome is presented in figures B-1 through B-14 for the front sensor and in figures B-15 through B-28 for the side sensor. The data for the side sensor was not analyzed because of reasons given in the Results and Discussion section, but the data is included here so that it would be available for analysis at a later date, if needed. Two representative sets of data for the "new" radome are given in figures B-29 through B-32 for the front and side sensors. Due to the fluctuations in the data versus time, a value of amplitude and phase was obtained by averaging each set of data over a time interval of about 10 seconds during the "steady" portion of the fluctuations (i.e. between the initial and final transient regions). These averaged data are presented in the Results and Discussion section and used in the determination of the water layer thickness.

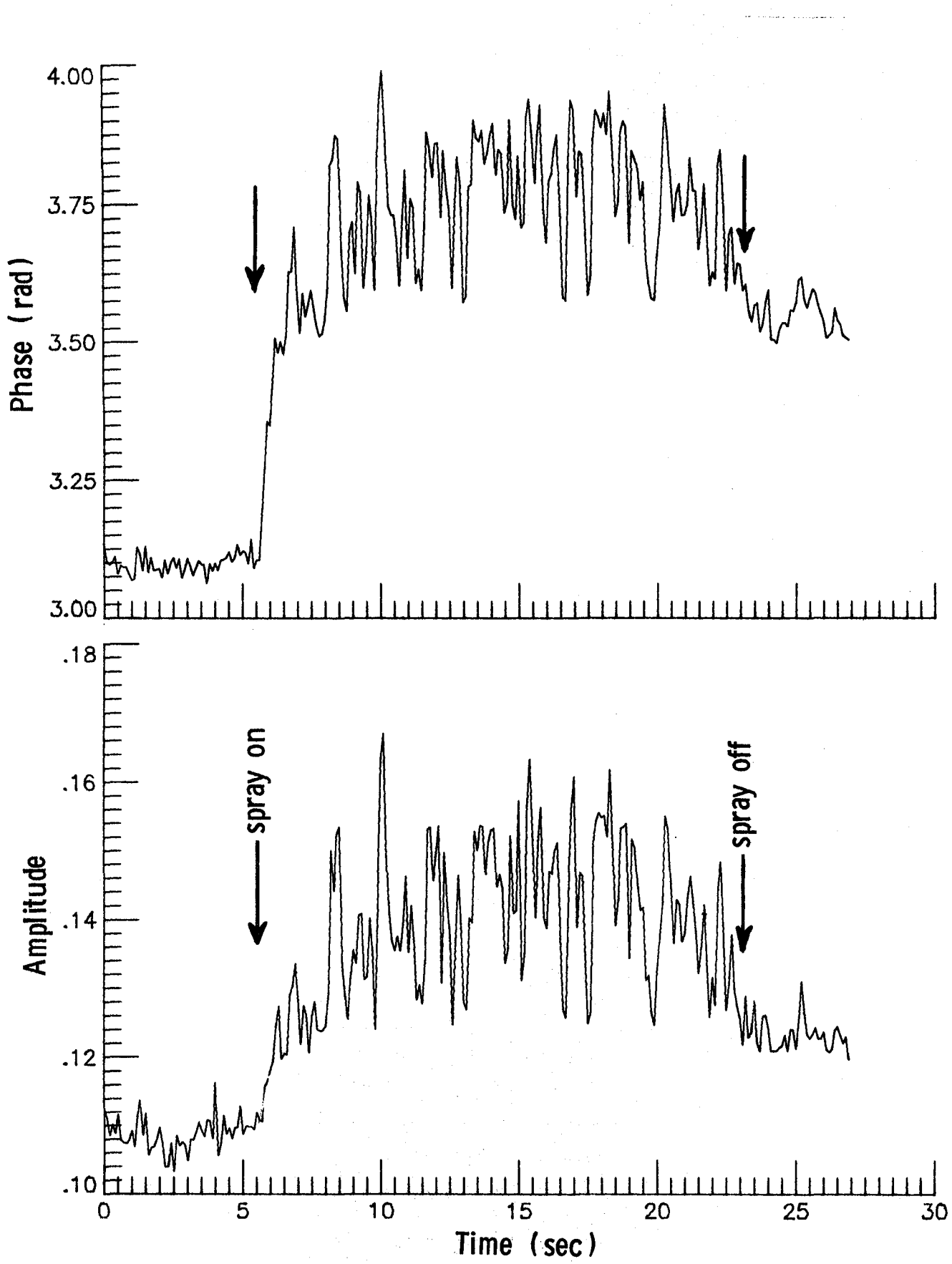

Figure B-1. Reflection coefficient for front sensor in "old" radome.

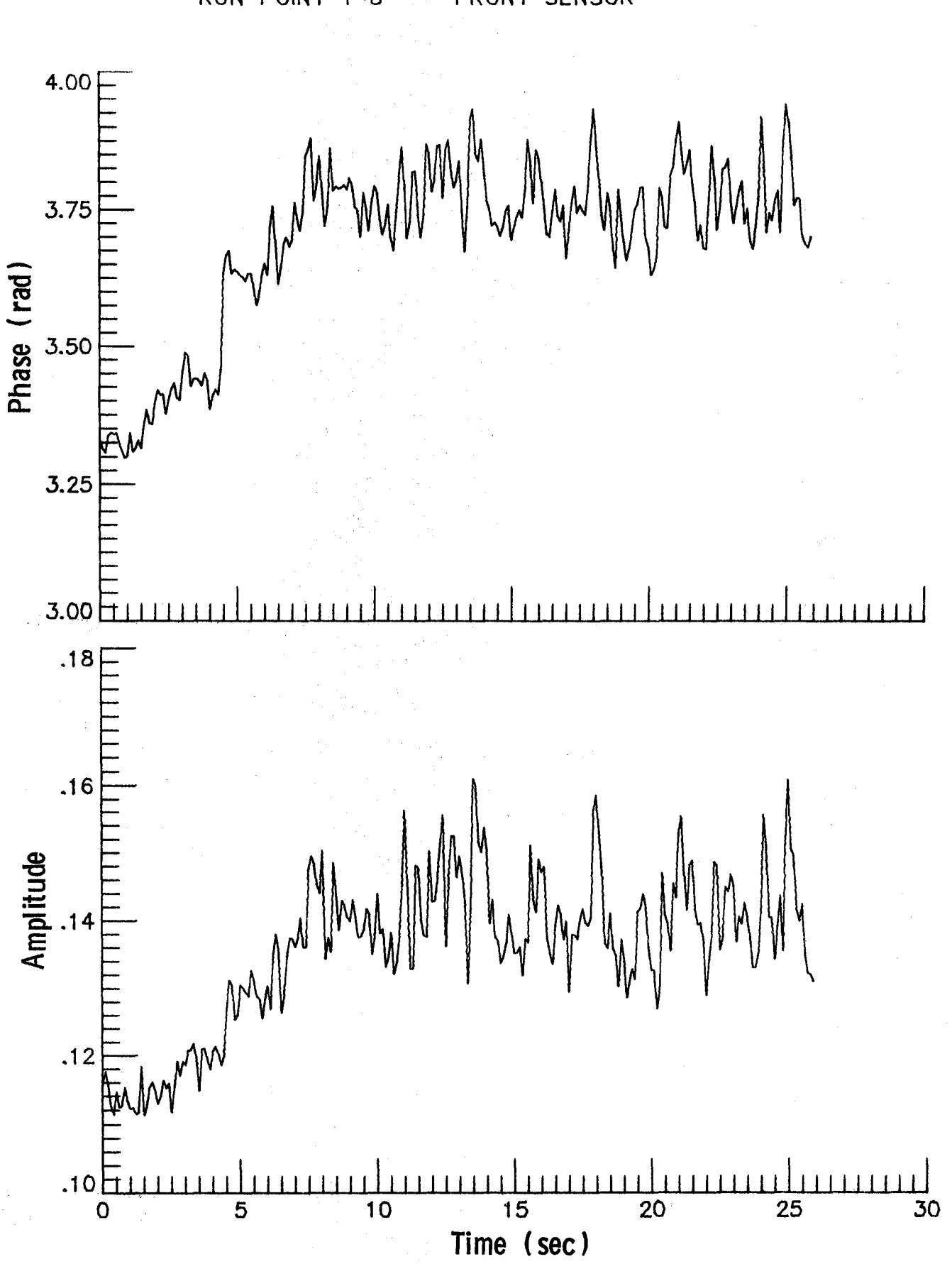

Figure B-2. Reflection coefficient for front sensor in "old" radome.

RUN-POINT 1-9 FRONT SENSOR

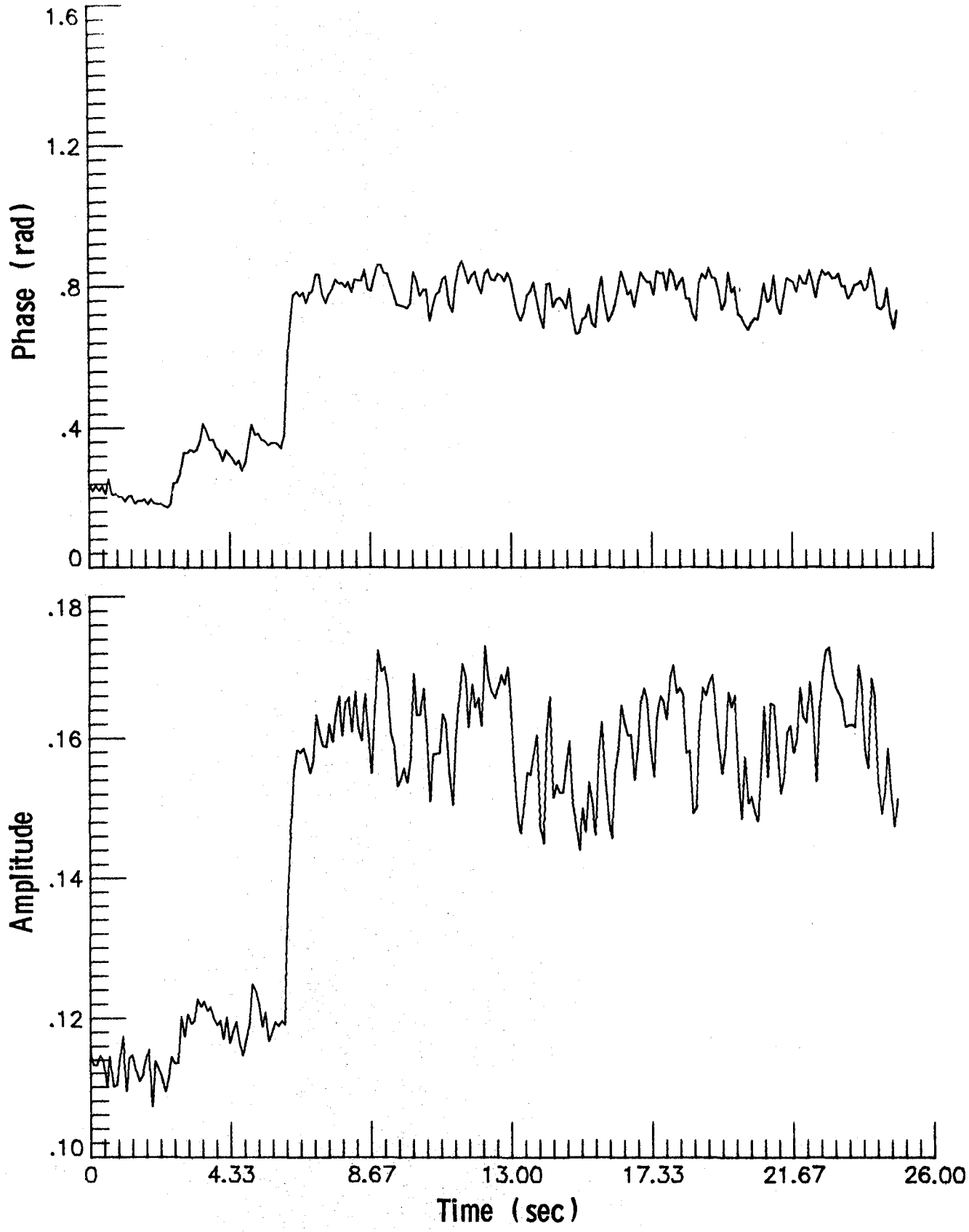

Figure B-3. Reflection coefficient for front sensor in "old" radome.

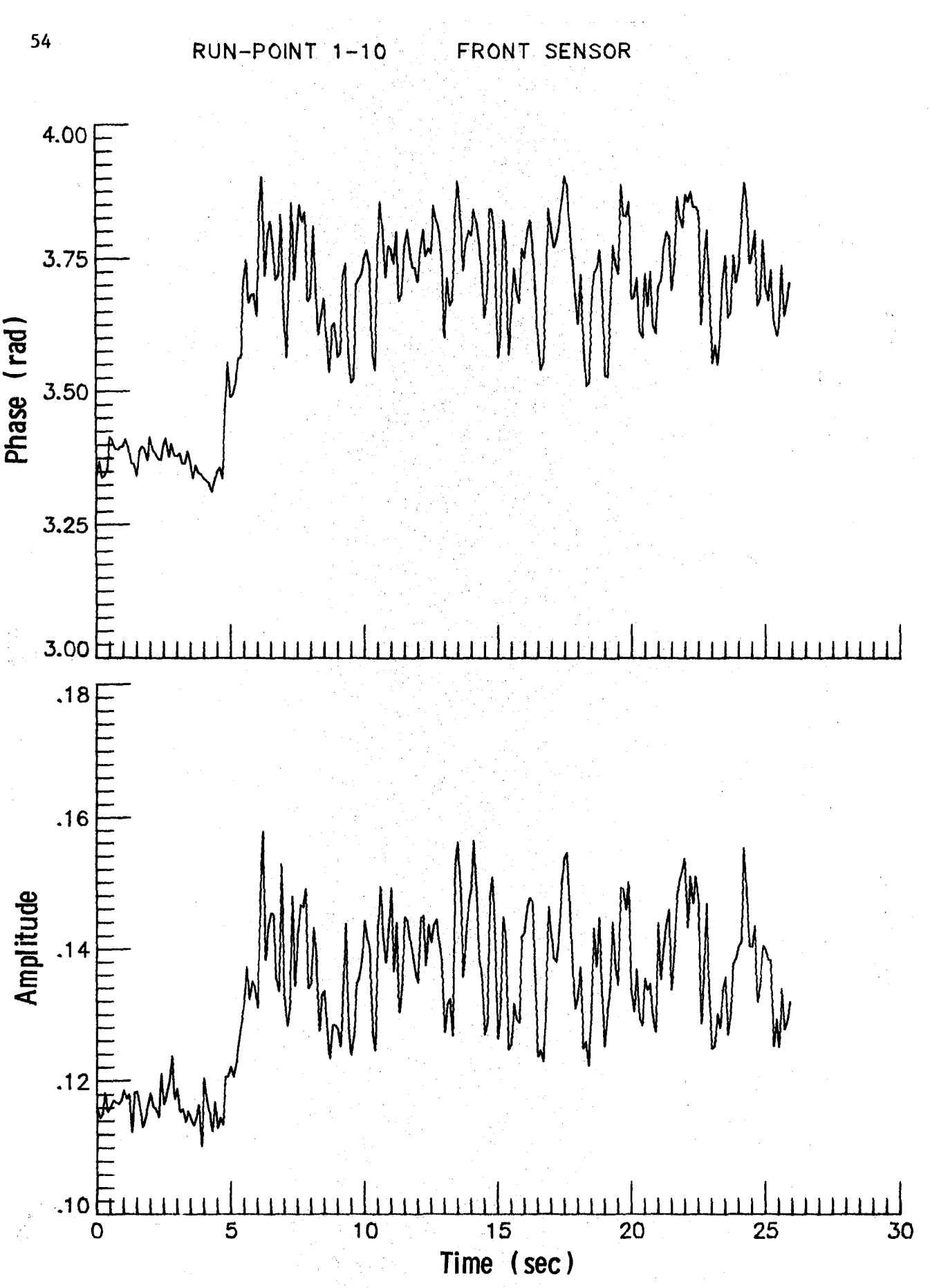

Figure B-4. Reflection coefficient for front sensor in "old" radome.

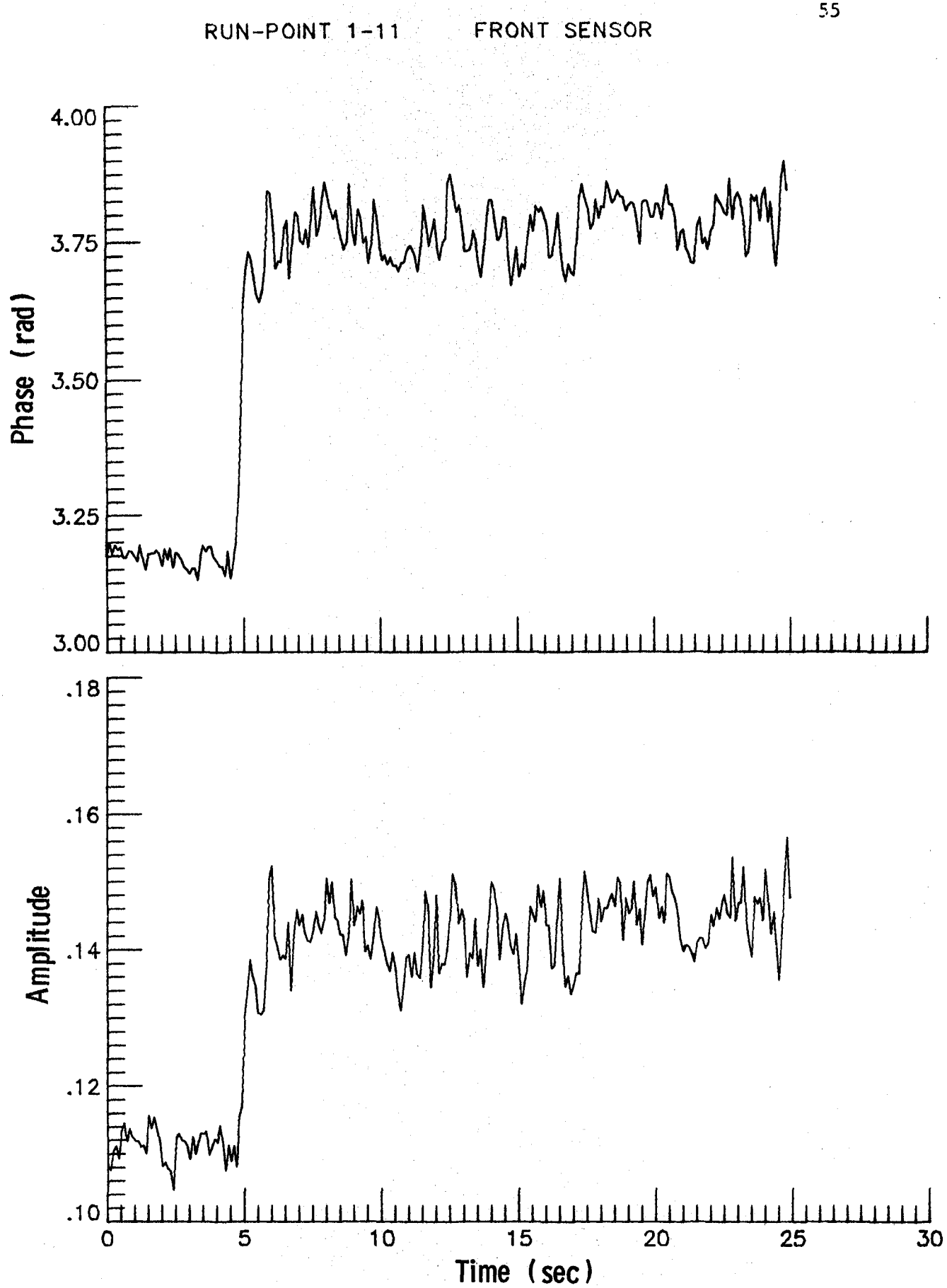

Figure B-5. Reflection coefficient for front sensor in "old" radome.

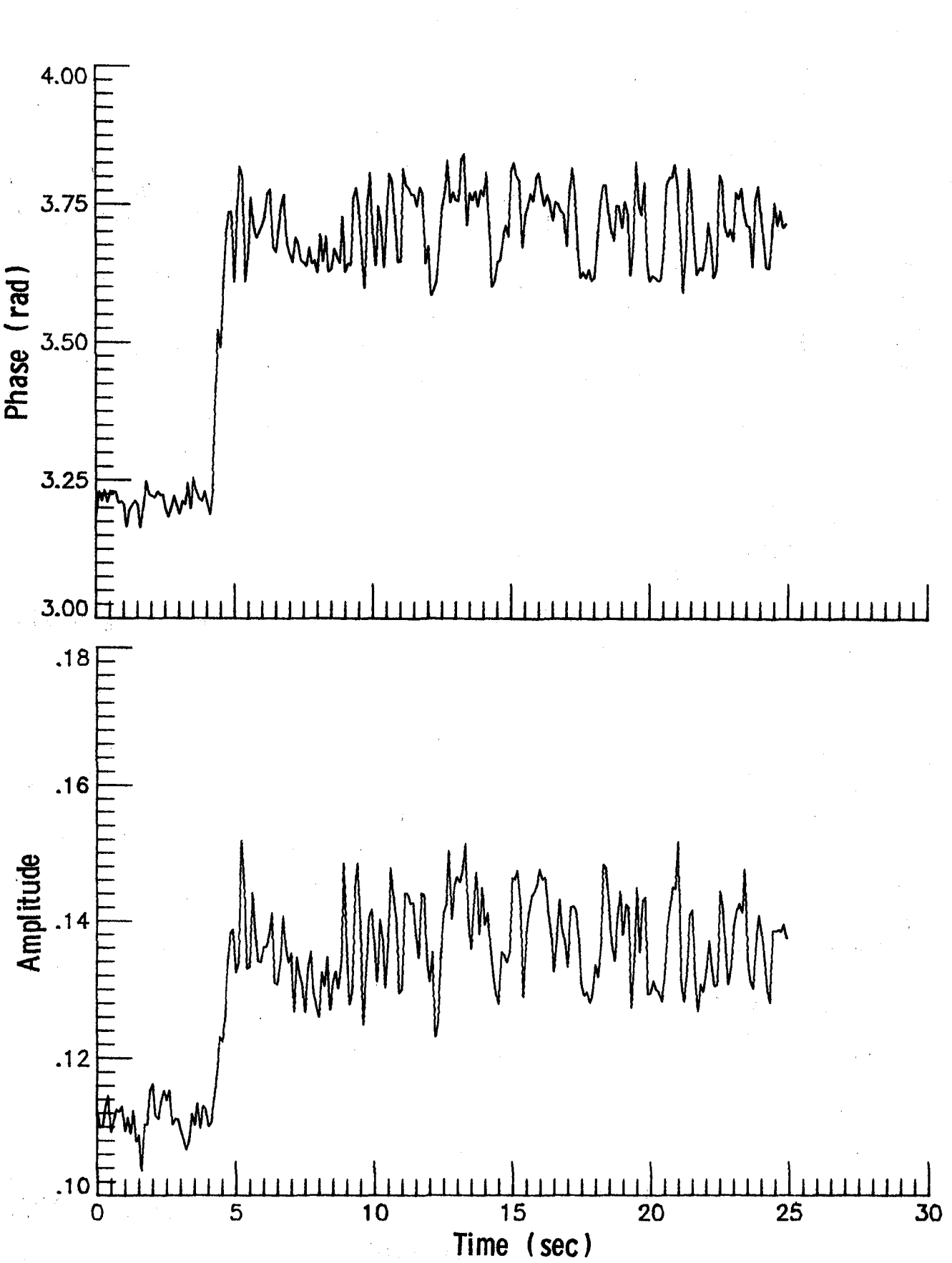

Figure B-6. Reflection coefficient for front sensor in "old" radome.

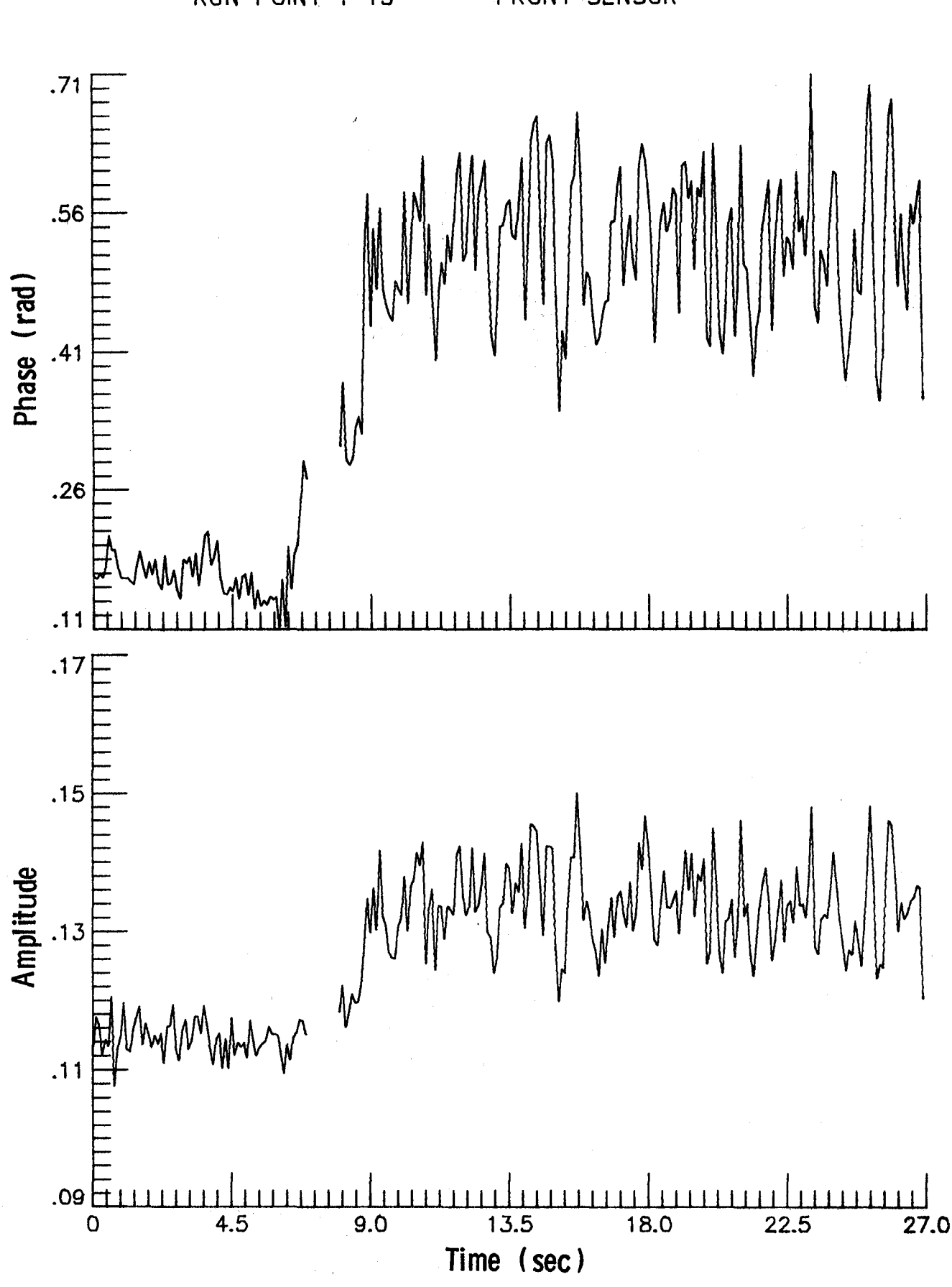

Figure B-7. Reflection coefficient for front sensor in "old" radome.

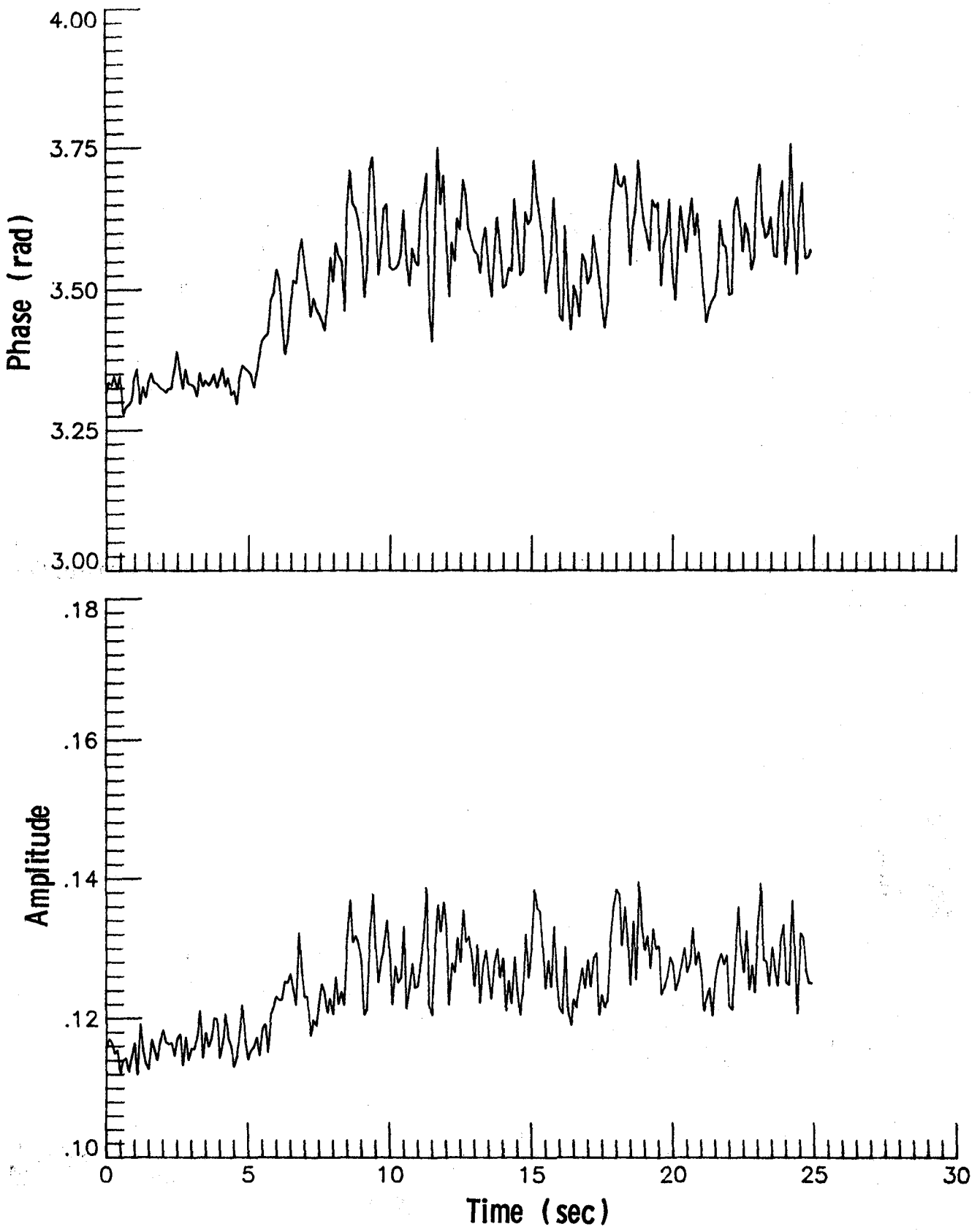

Figure B-8. Reflection coefficient for front sensor in "old" radome.

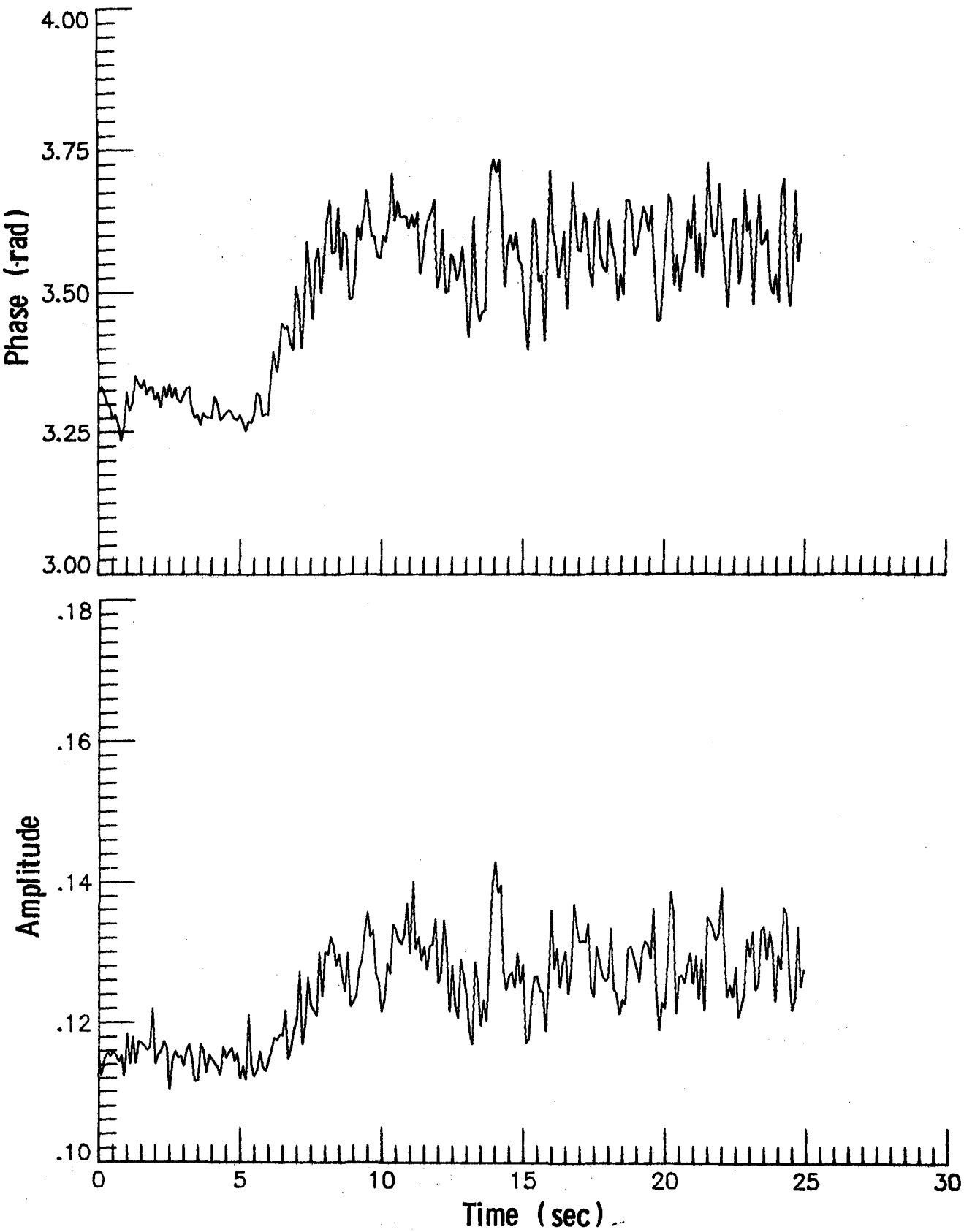

Figure B-9. Reflection coefficient for front sensor in "old" radome.

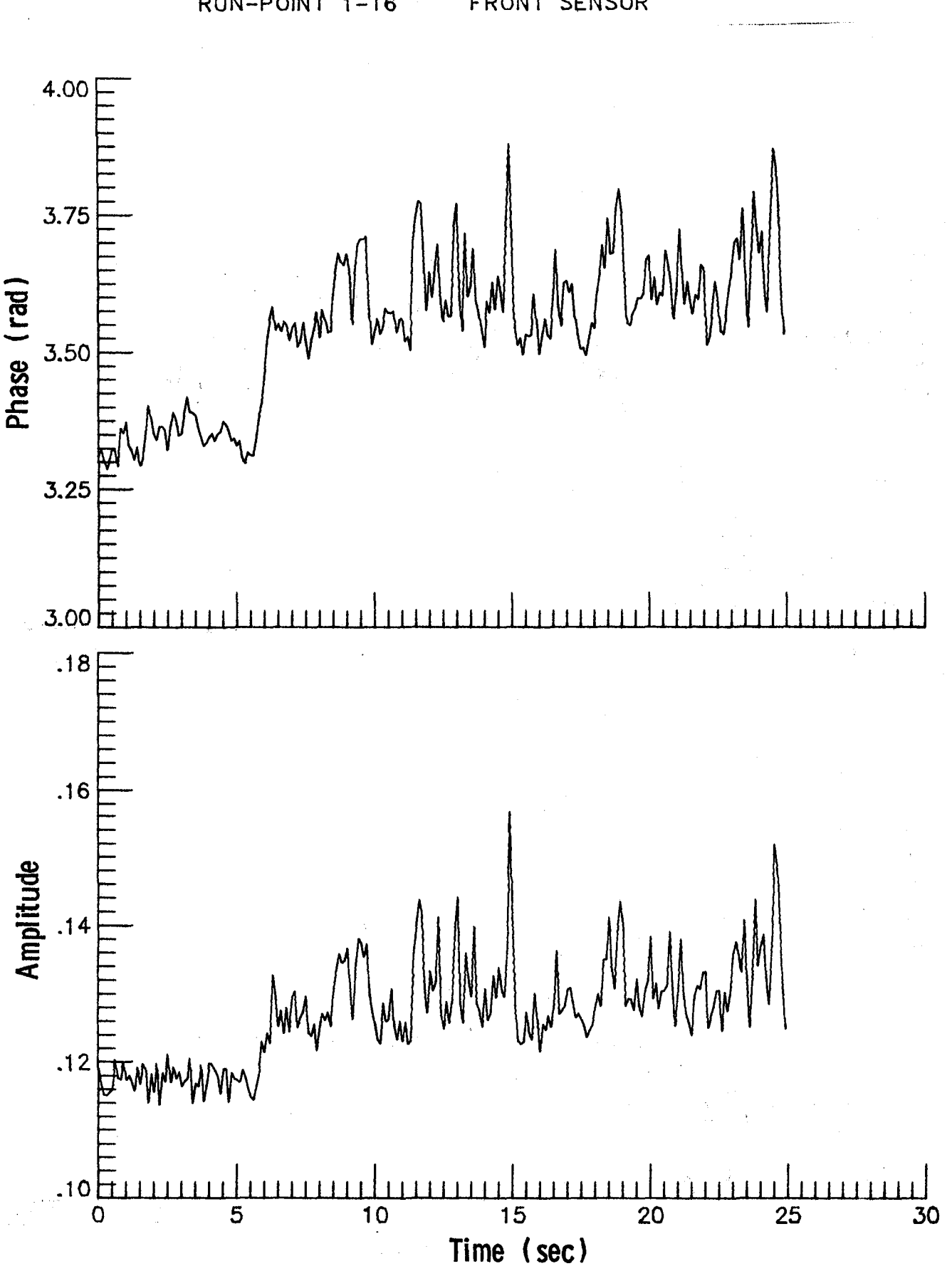

Figure B-10. Reflection coefficient for front sensor in "old" radome.

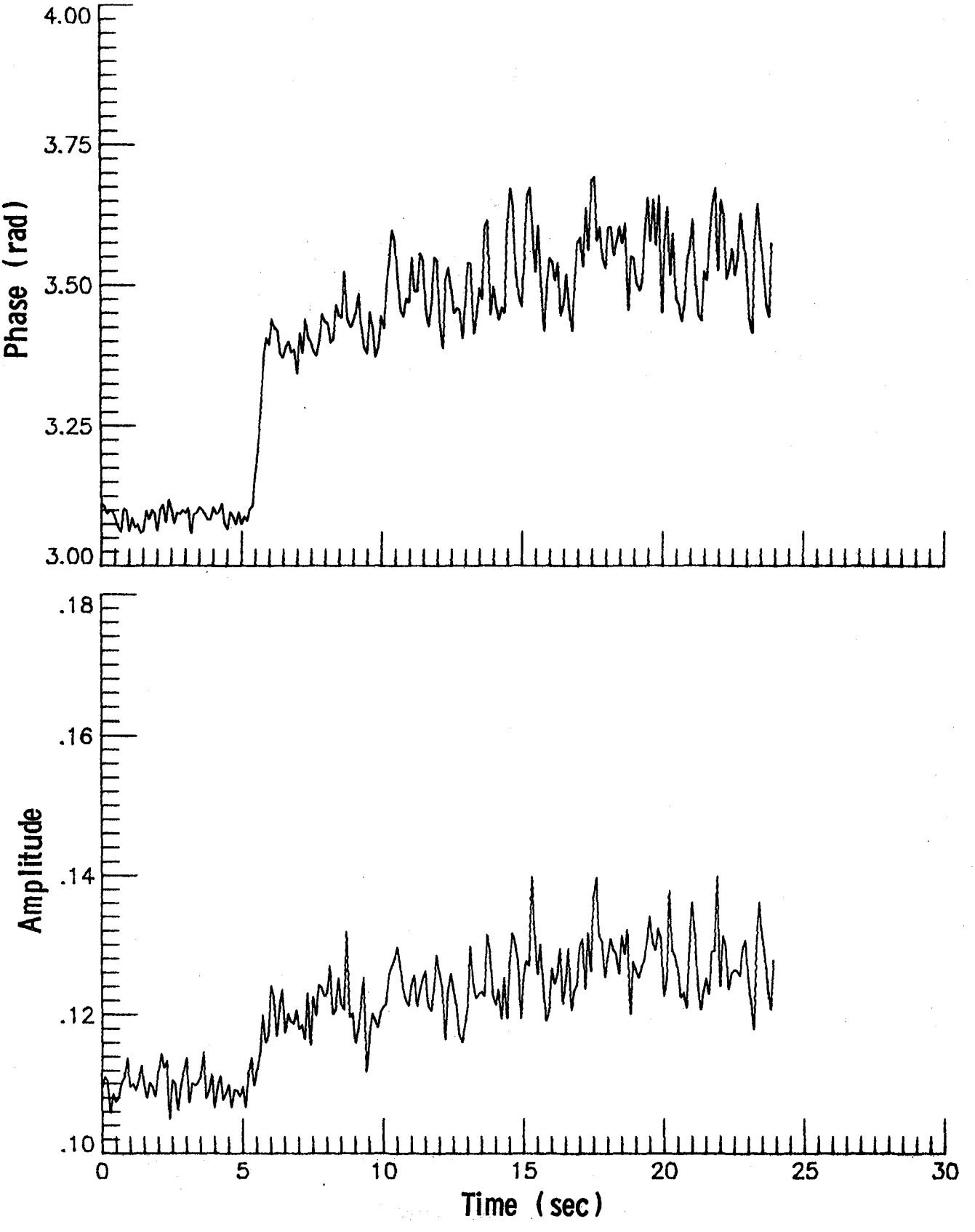

Figure B-11. Reflection coefficient for front sensor in "old" radome.

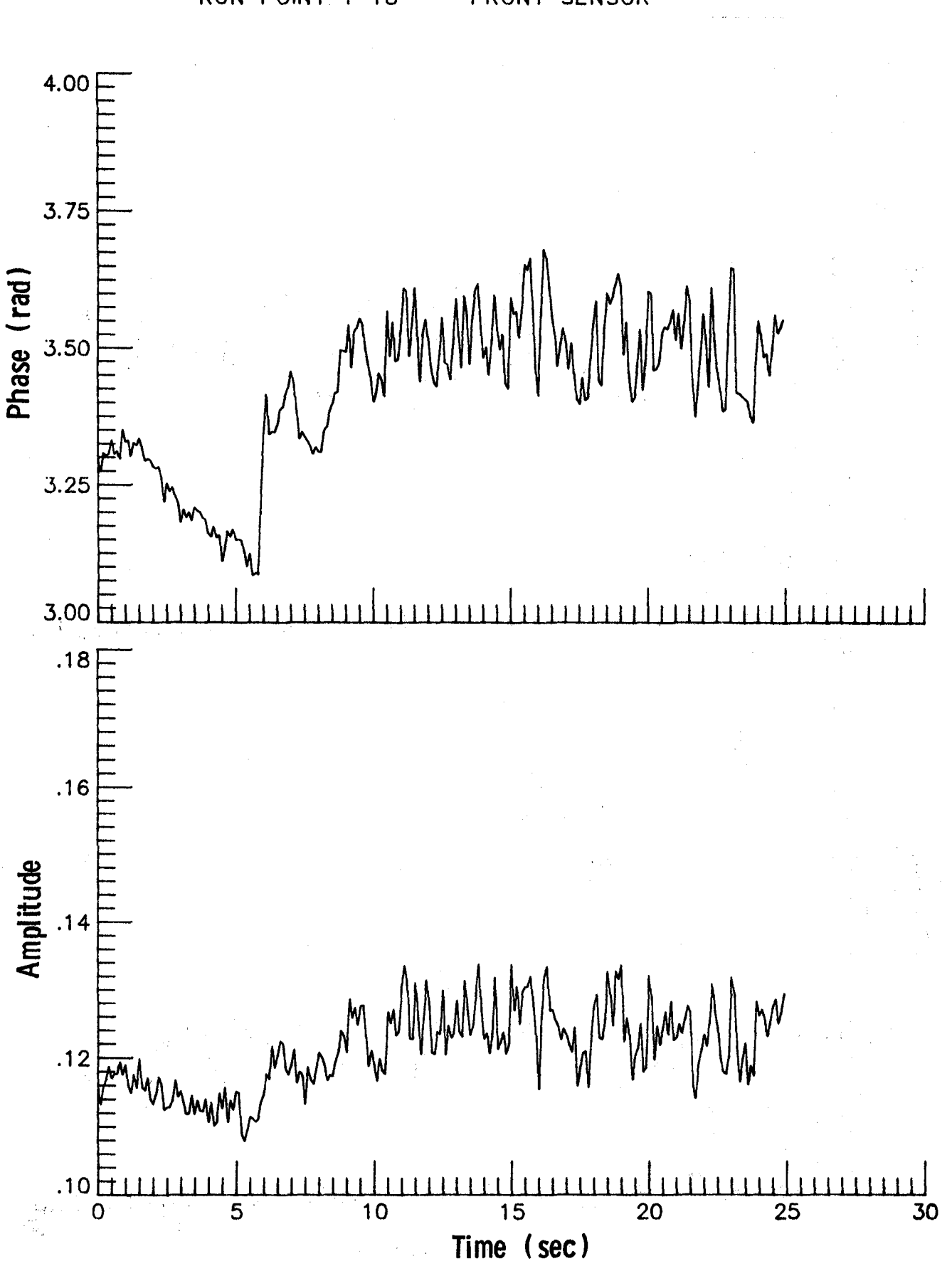

Figure B-12. Reflection coefficient for front sensor in "old" radome.

RUN-POINT 1-19 FRONT SENSOR

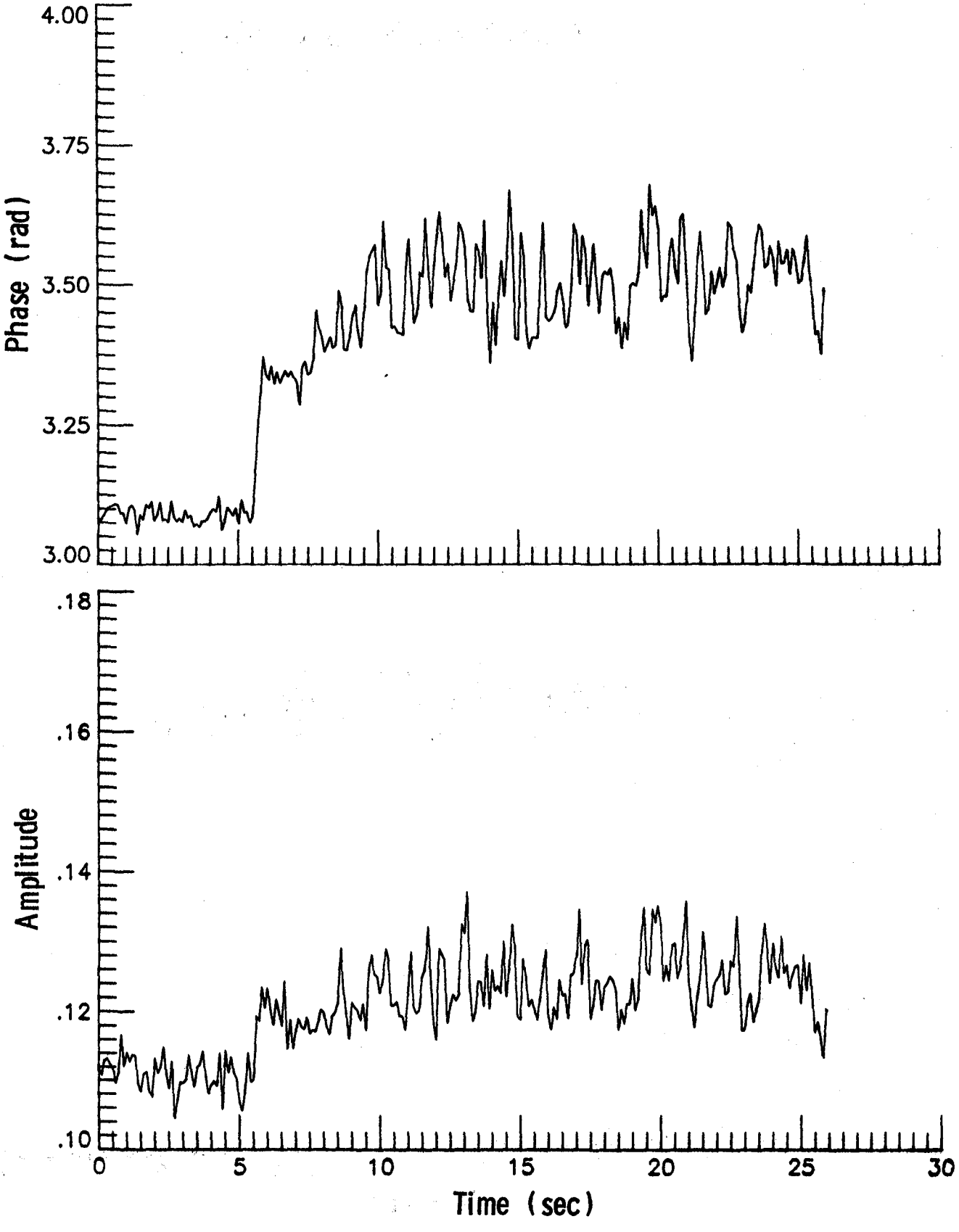

Figure B-13. Reflection coefficient for front sensor in "old" radome.

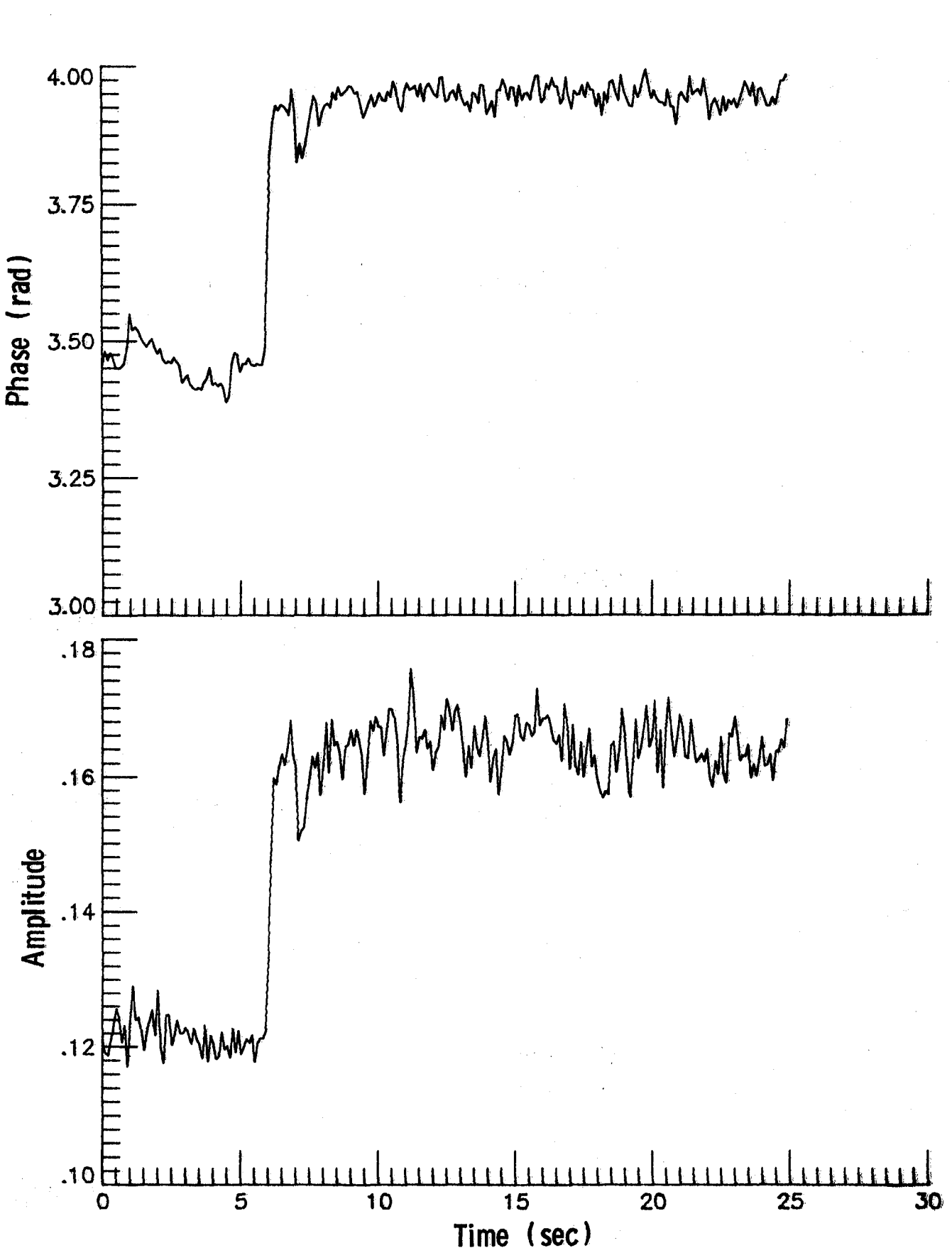

Figure B-14. Reflection coefficient for front sensor in "old" radome.

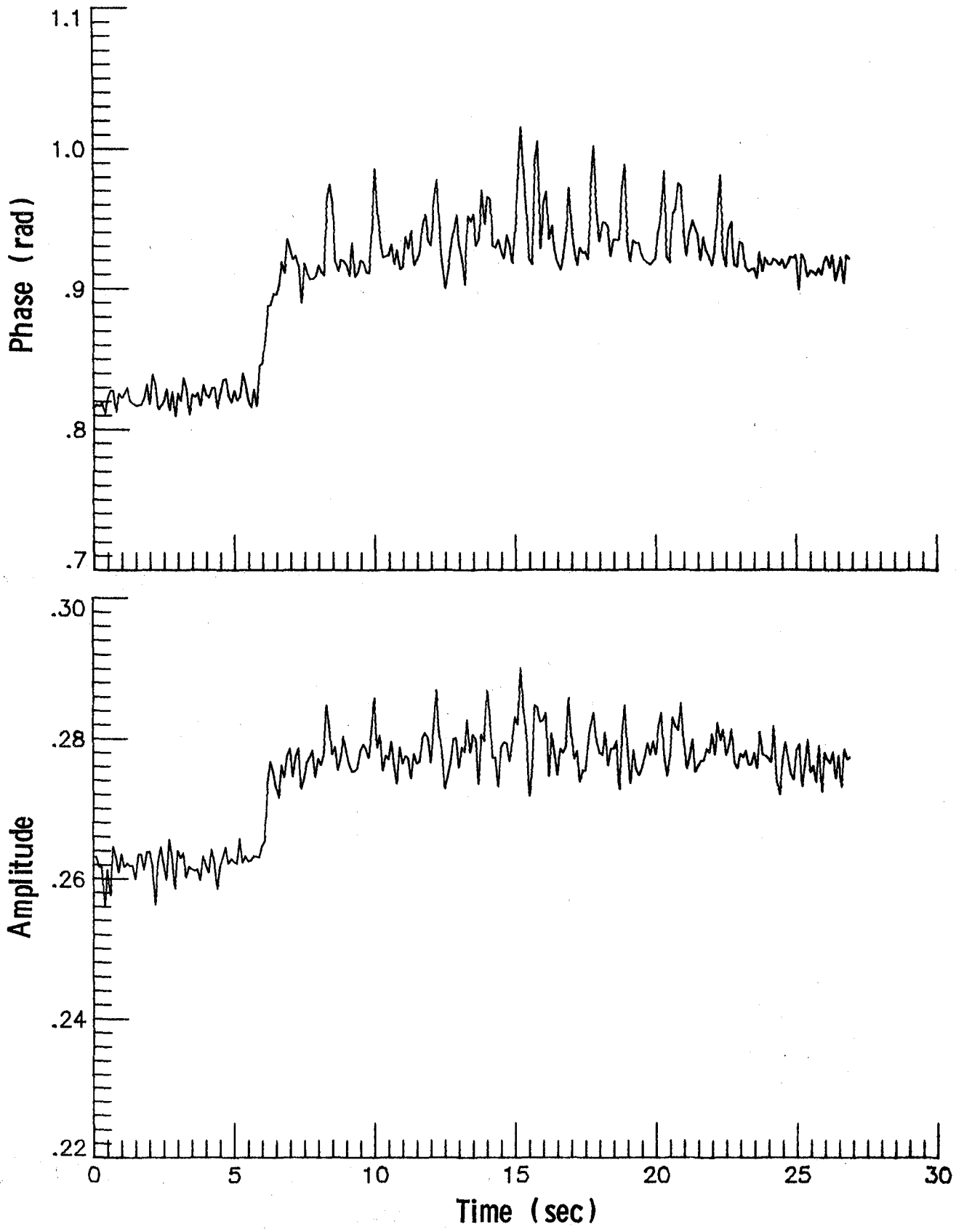

Figure B-15. Reflection coefficient for side sensor in "old" radome.

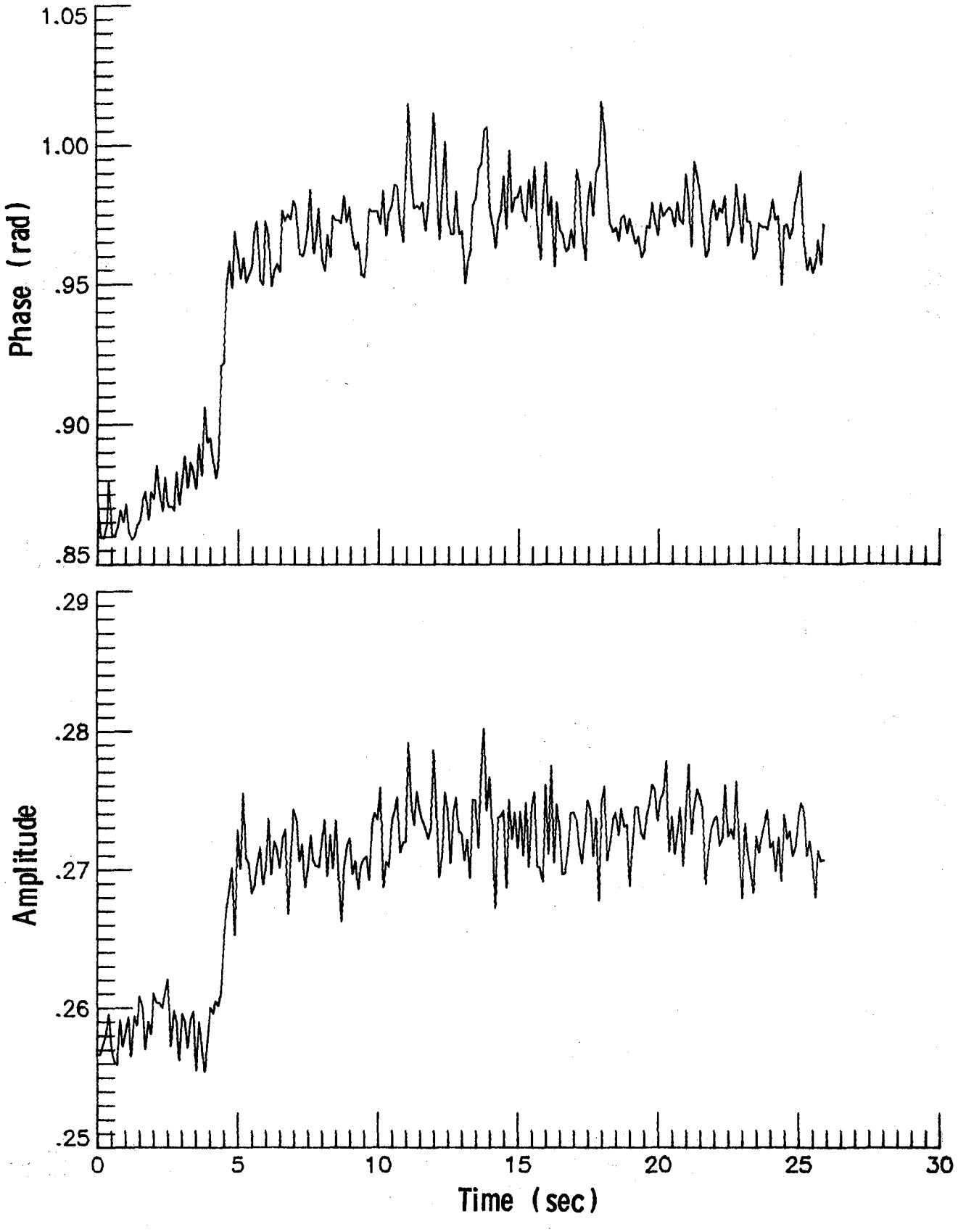

Figure B-16. Reflection coefficient for side sensor in "old" radome.

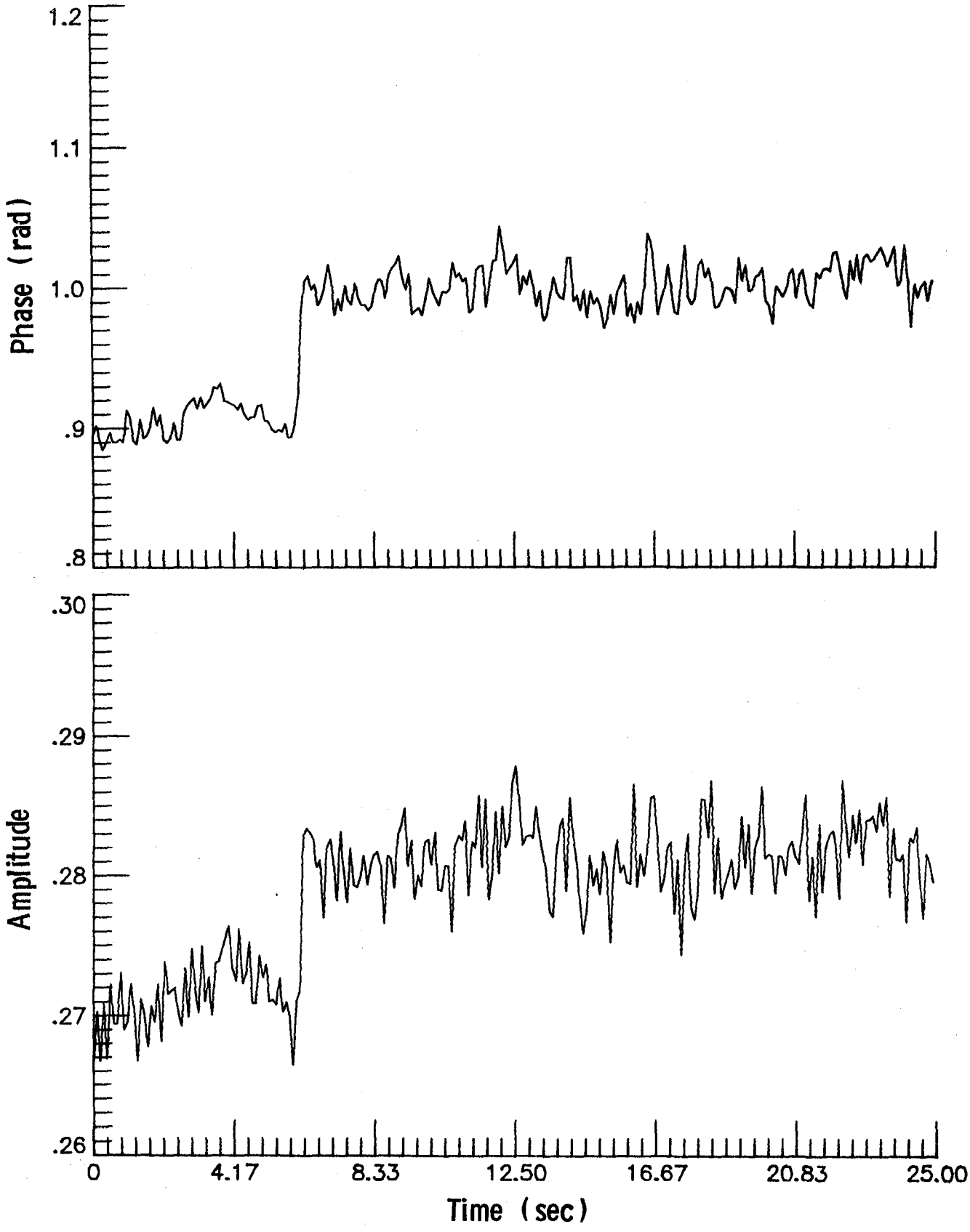

Figure B-17. Reflection coefficient for side sensor in "old" radome.

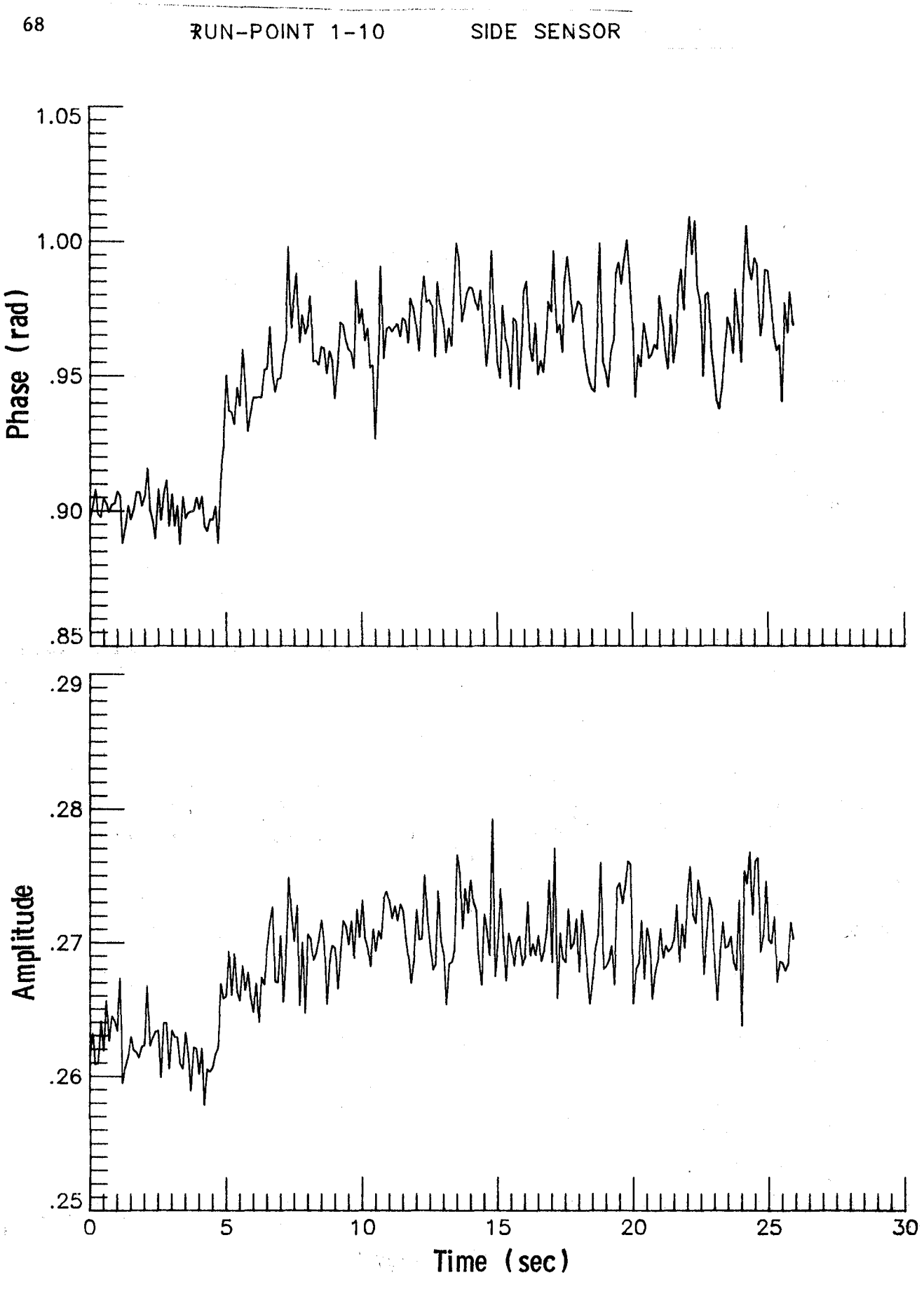

Figure B-18. Reflection coefficient for side sensor in "old" radome.

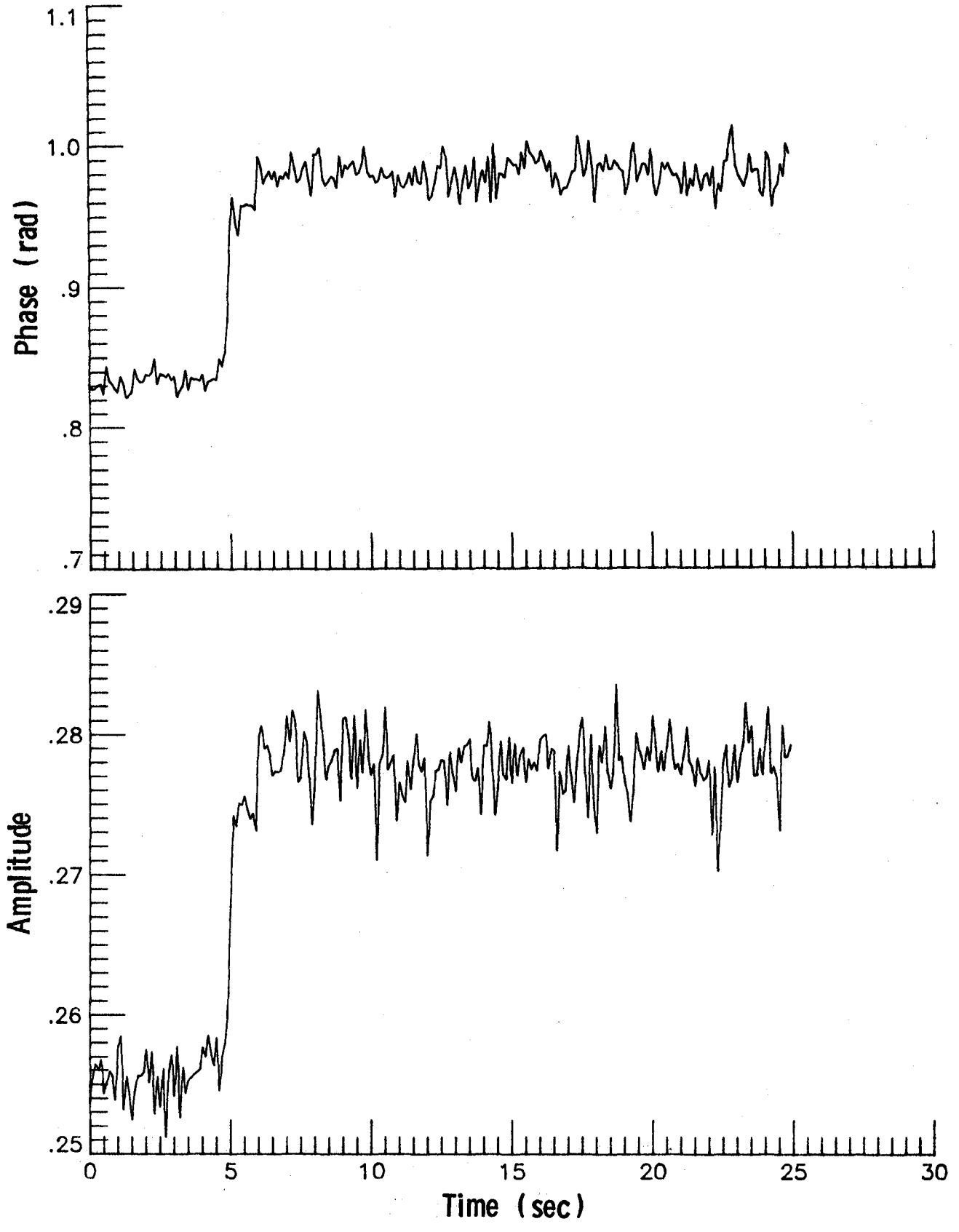

Figure B-19. Reflection coefficient for side sensor in "old" radome.

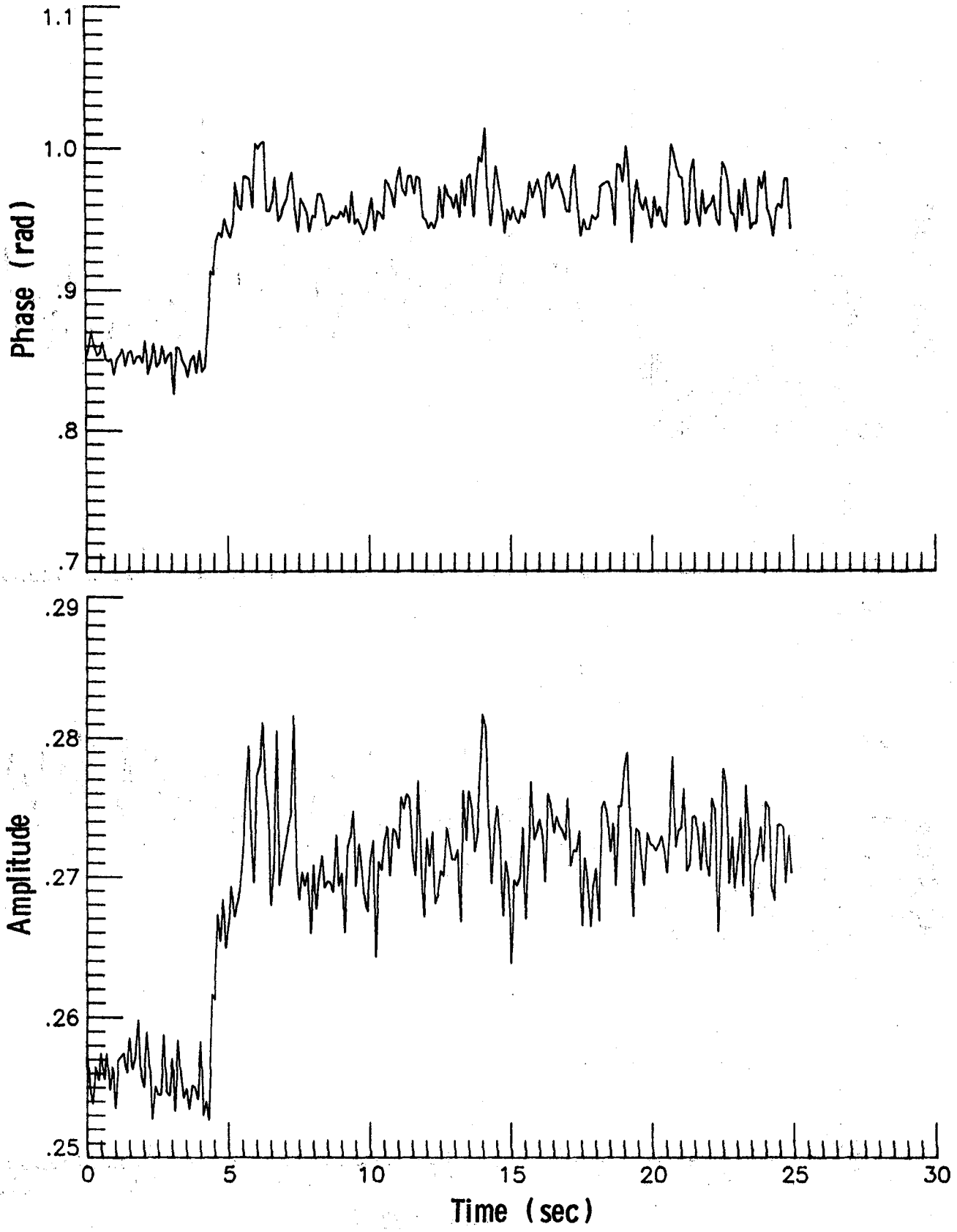

Figure B-20. Reflection coefficient for side sensor in "old" radome.

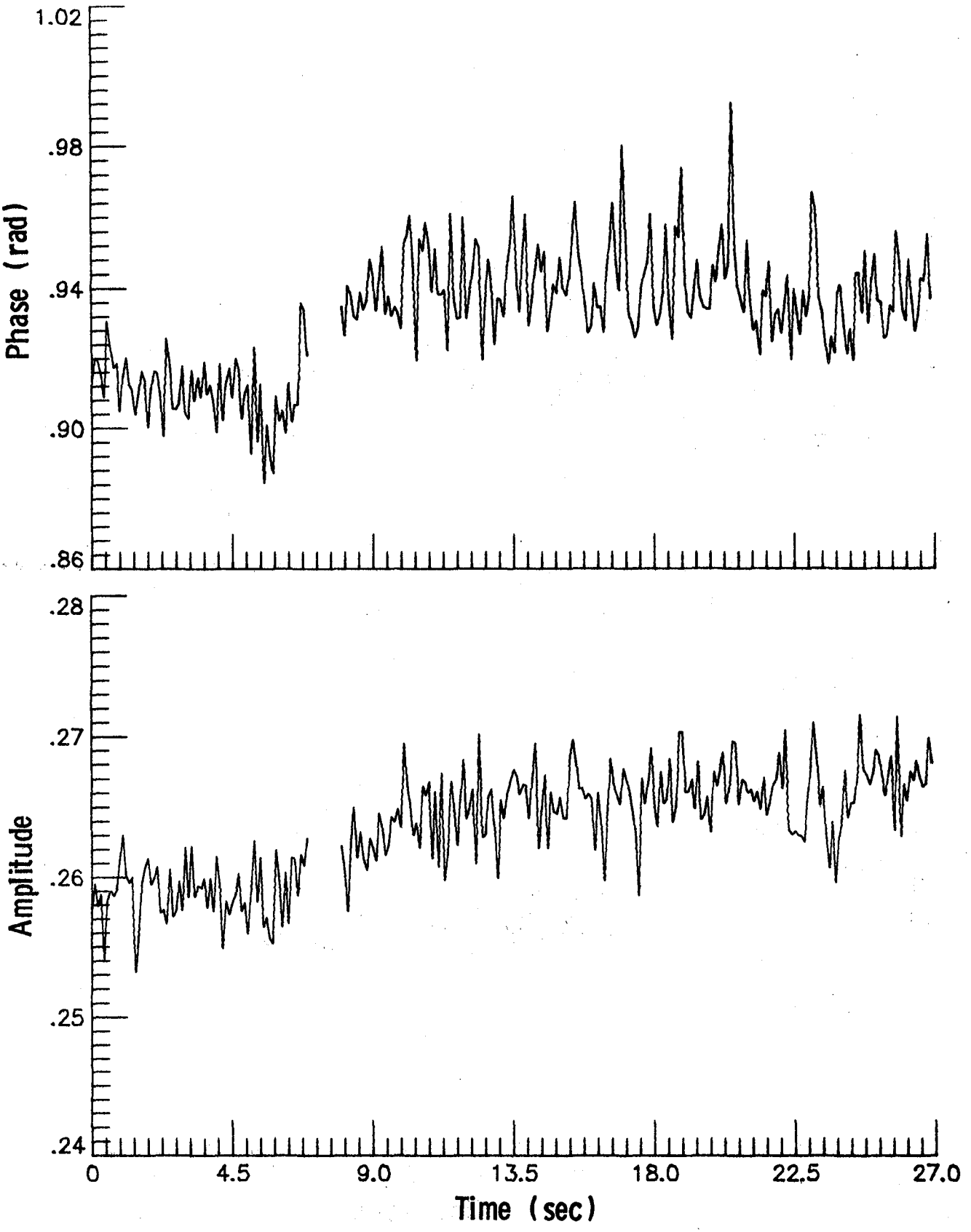

Figure B-21. Reflection coefficient for side sensor in "old" radome.

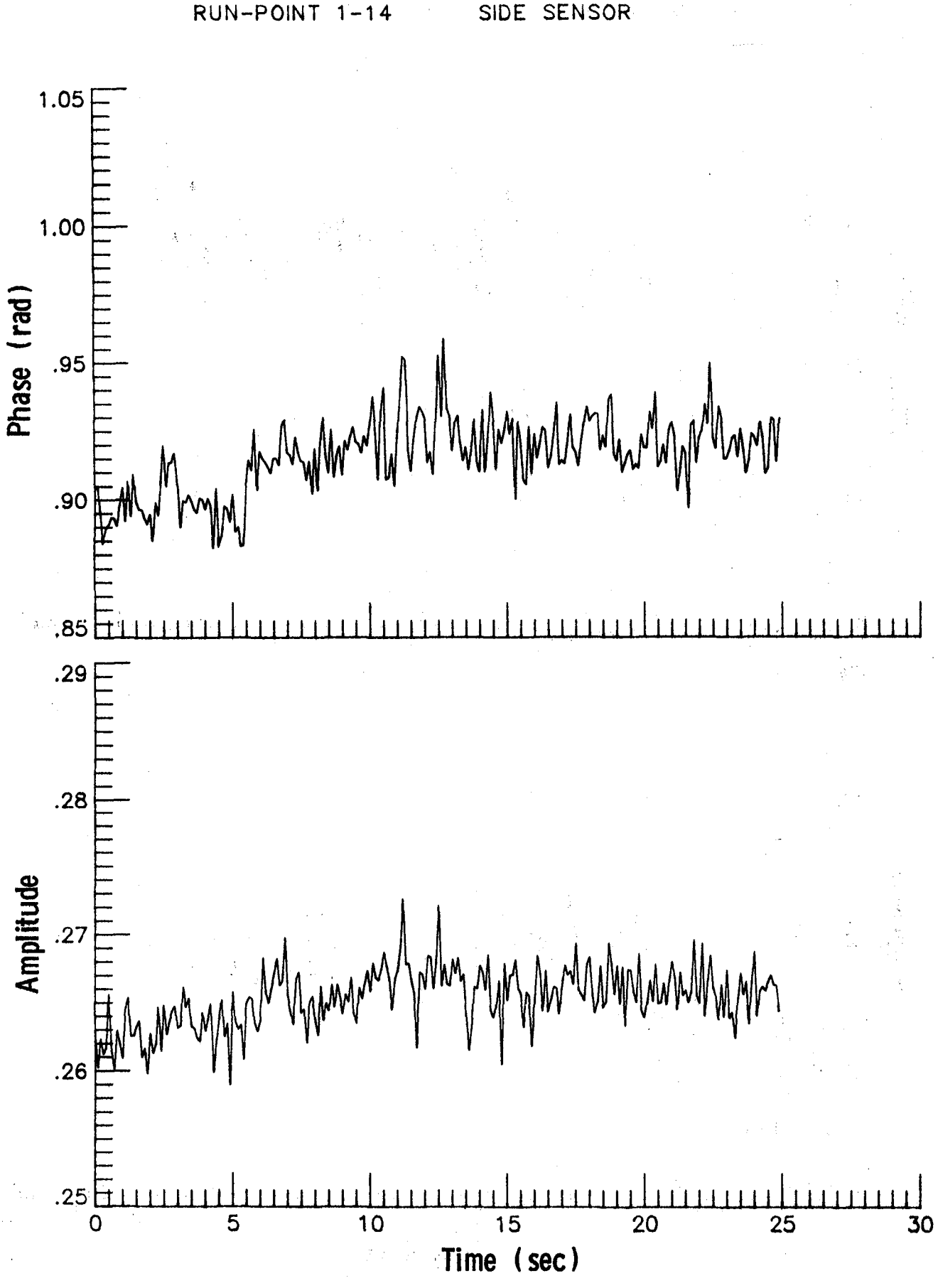

Figure B-22. Reflection coefficient for side sensor in "old" radome.

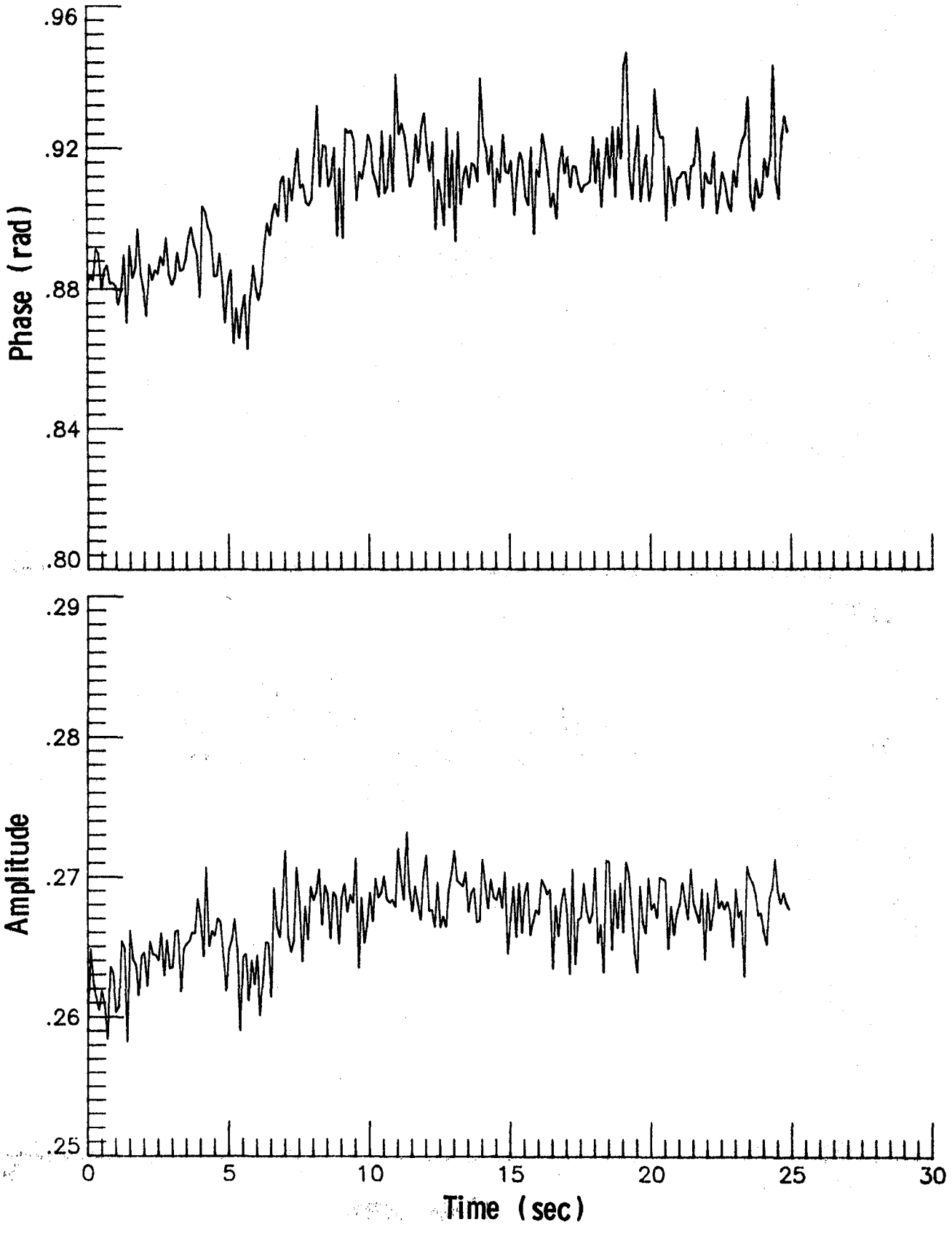

Figure B-23. Reflection coefficient for side sensor in "old" radome

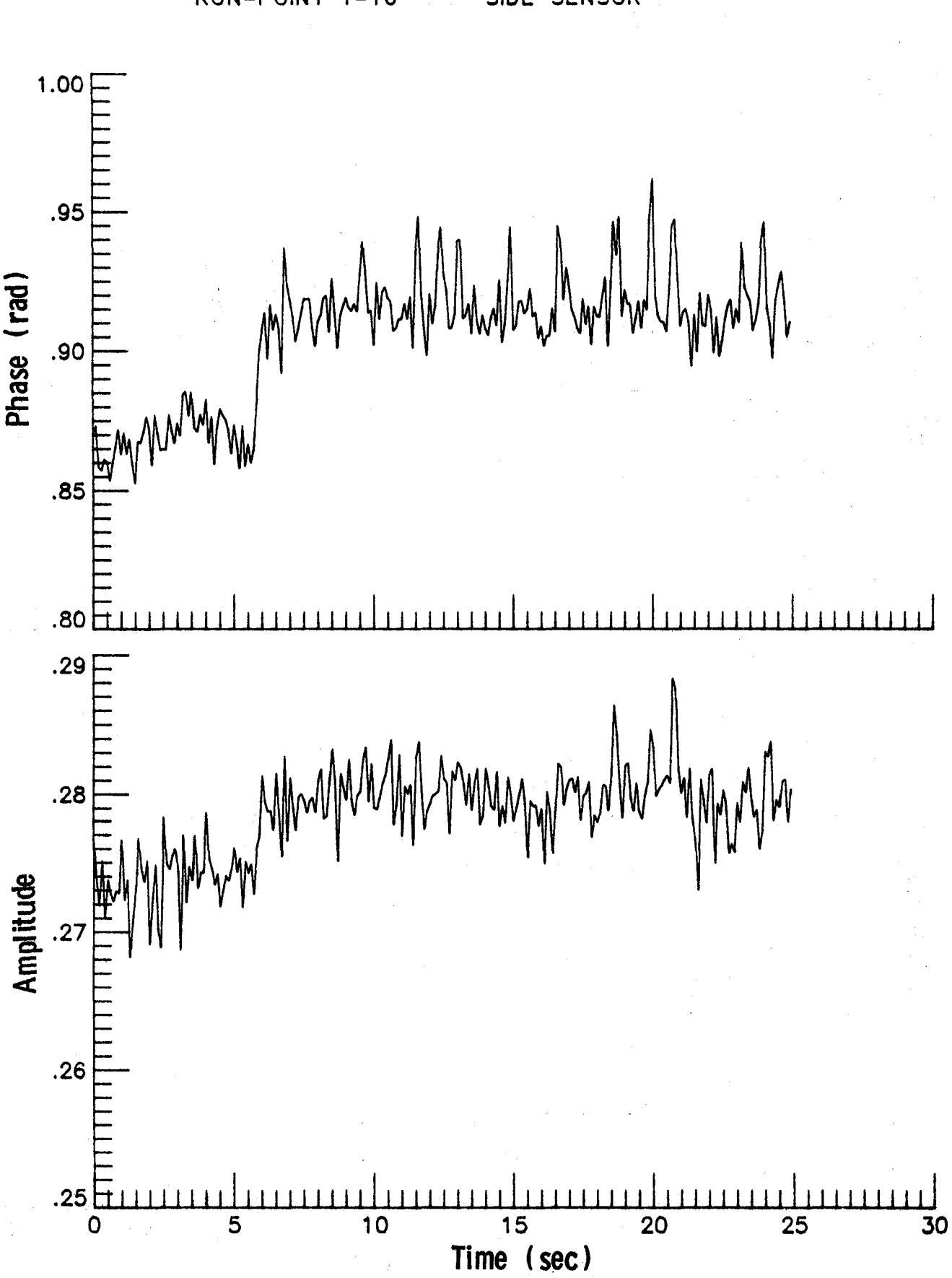

Figure B-24. Reflection coefficient for side sensor in "old" radome.

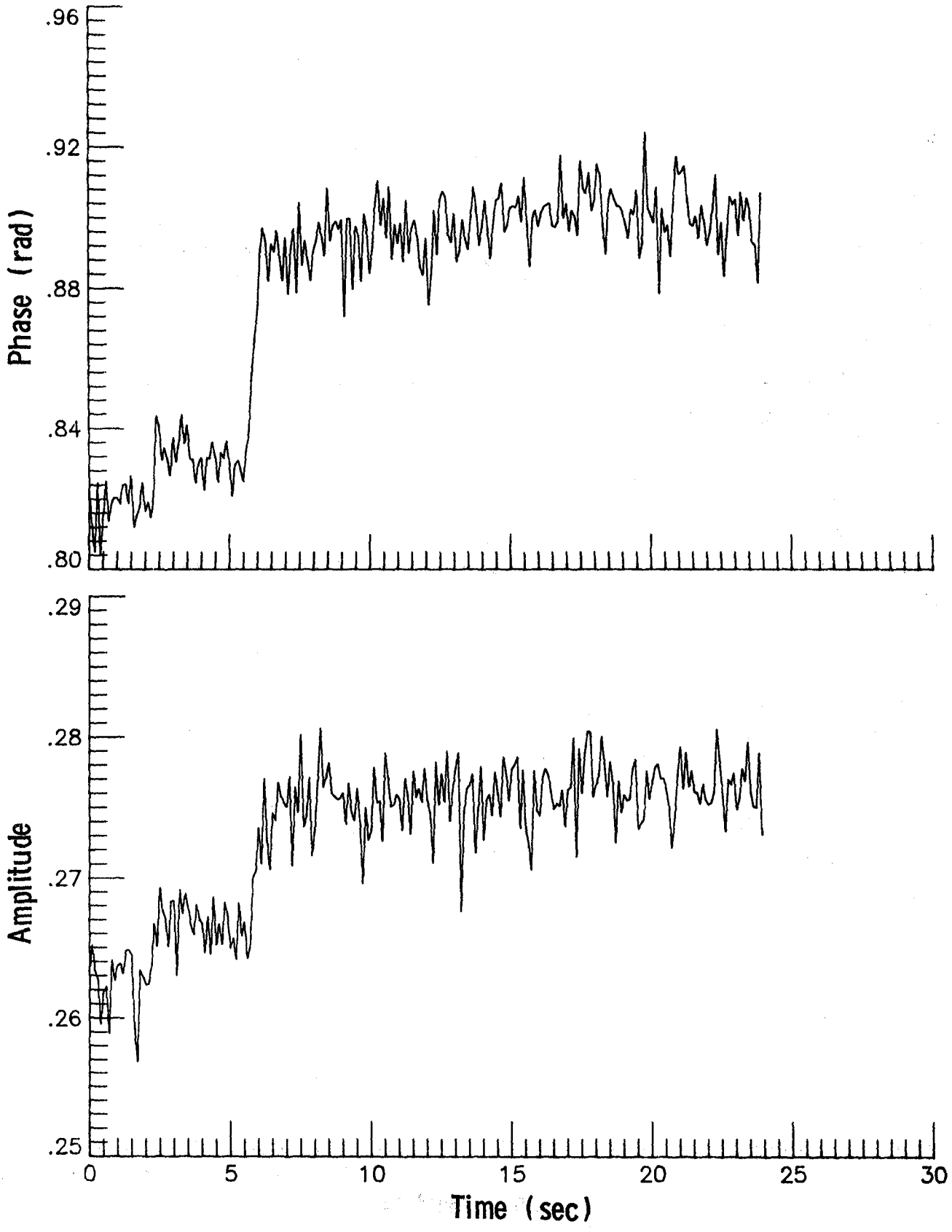

Figure B-25. Reflection coefficient for side sensor in "old" radome.

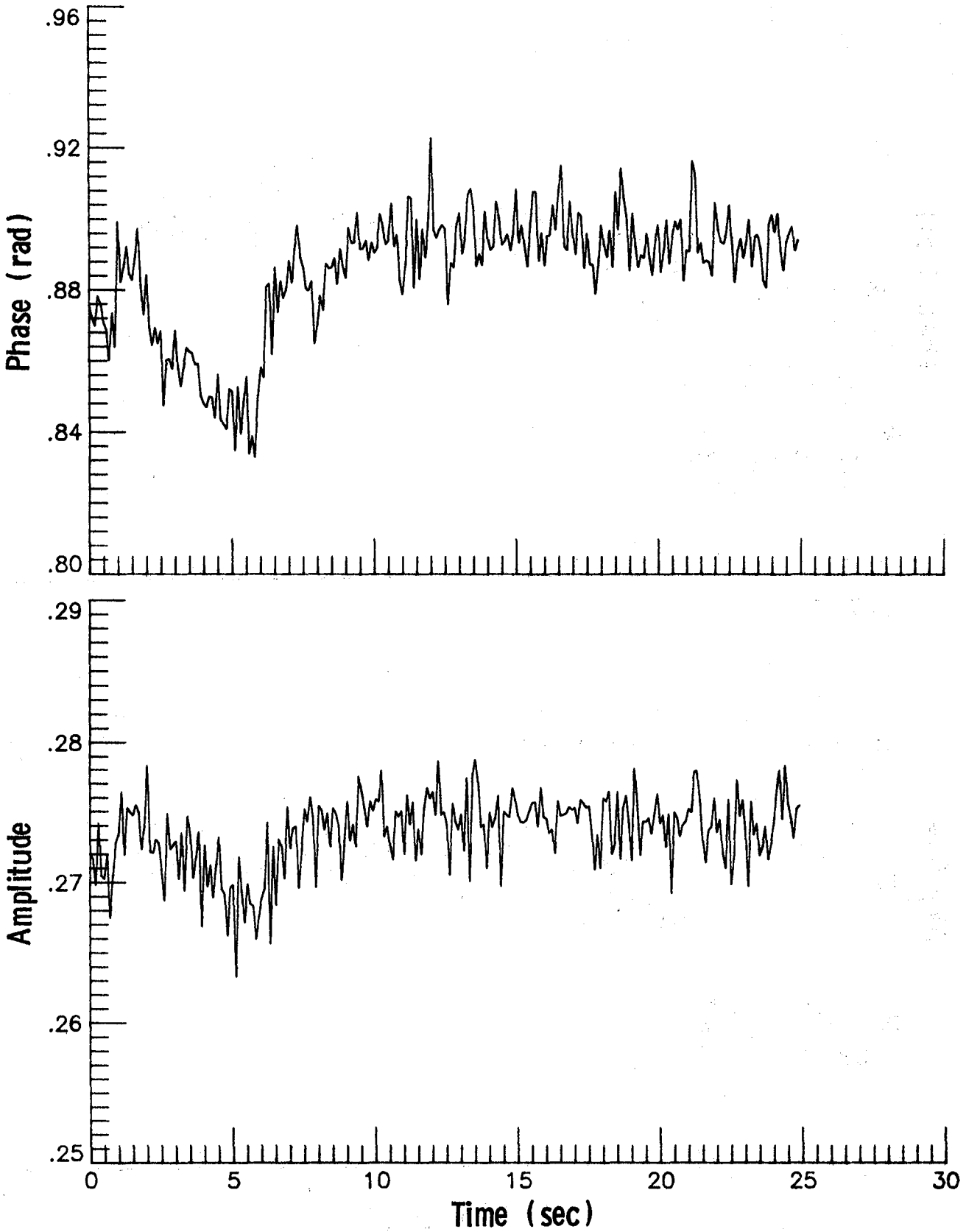

Figure B-26. Reflection coefficient for side sensor in "old" radome.

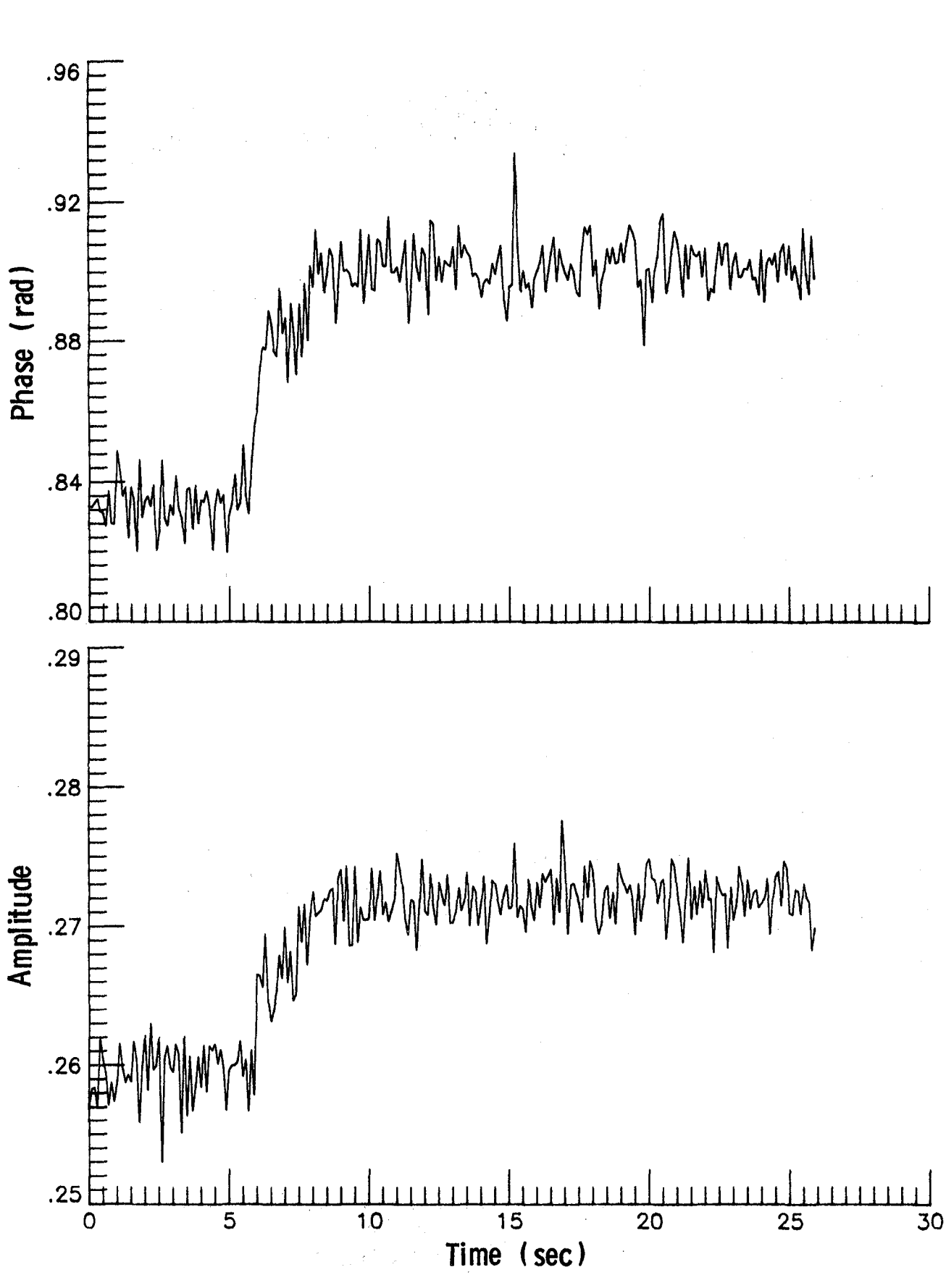

Figure B-27. Reflection coefficient for side sensor in "old" radome.

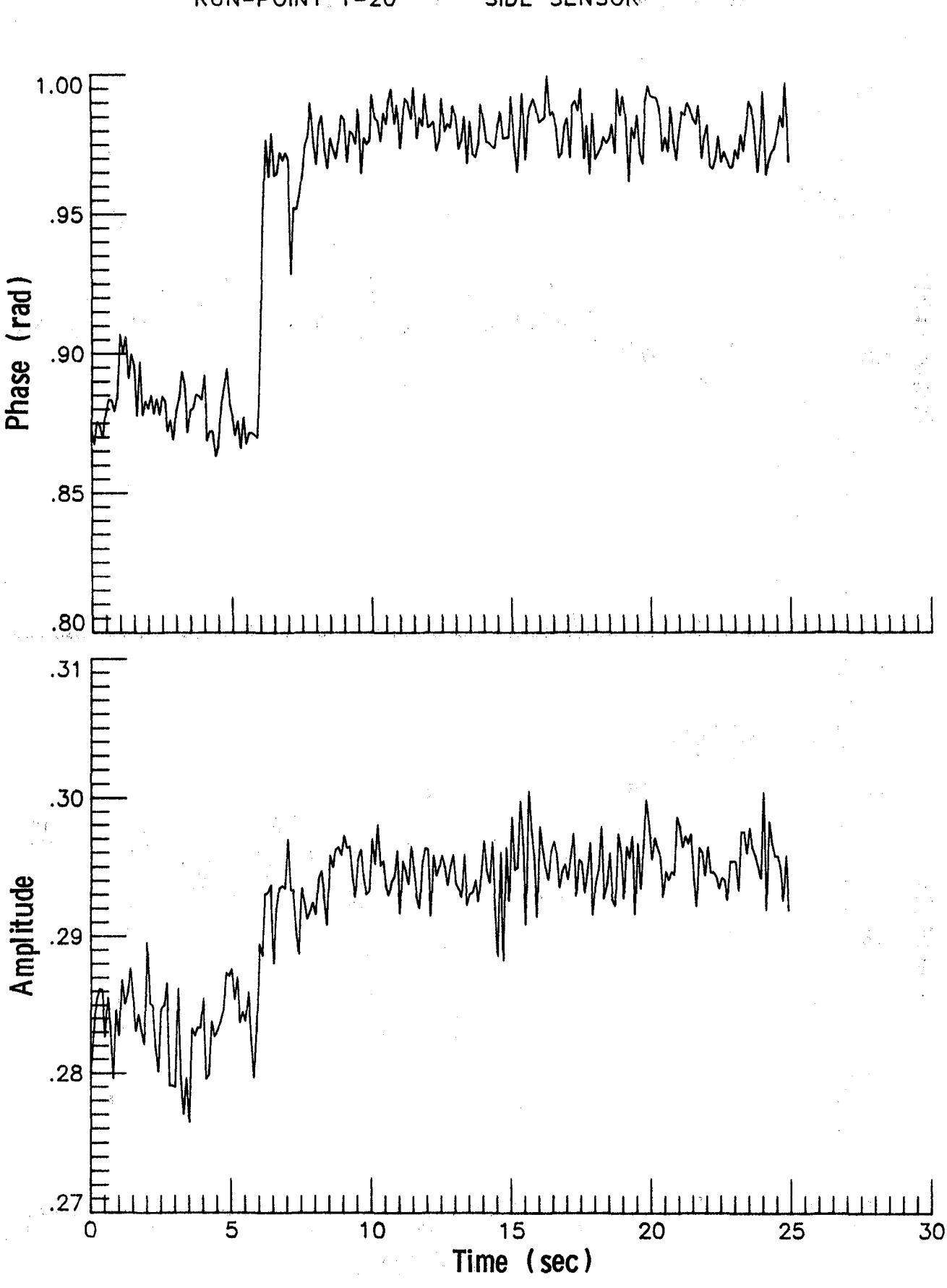

Figure B-28. Reflection coefficient for side sensor in "old" radome.

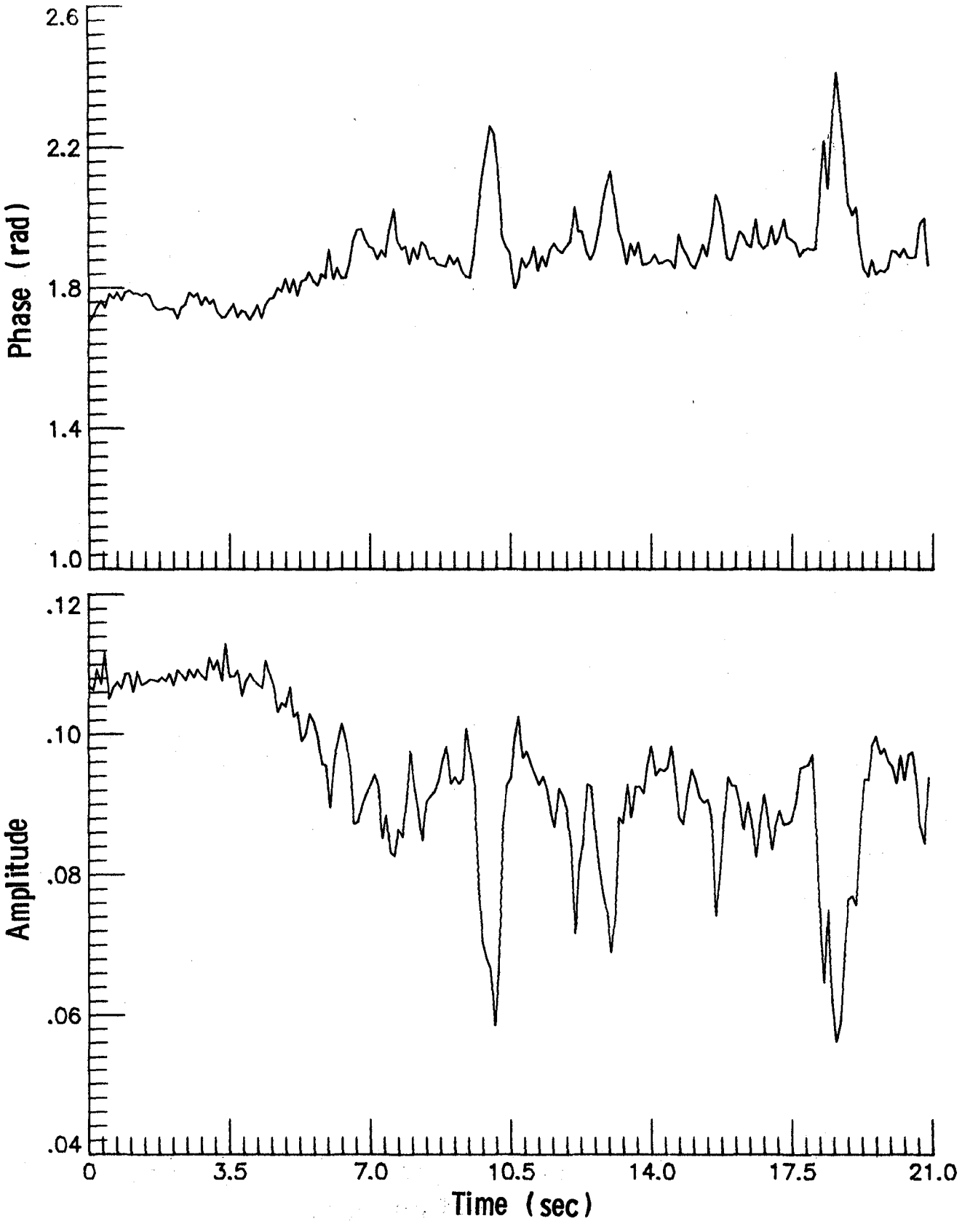

Figure B-29. Reflection coefficient for front sensor in "new" radome.

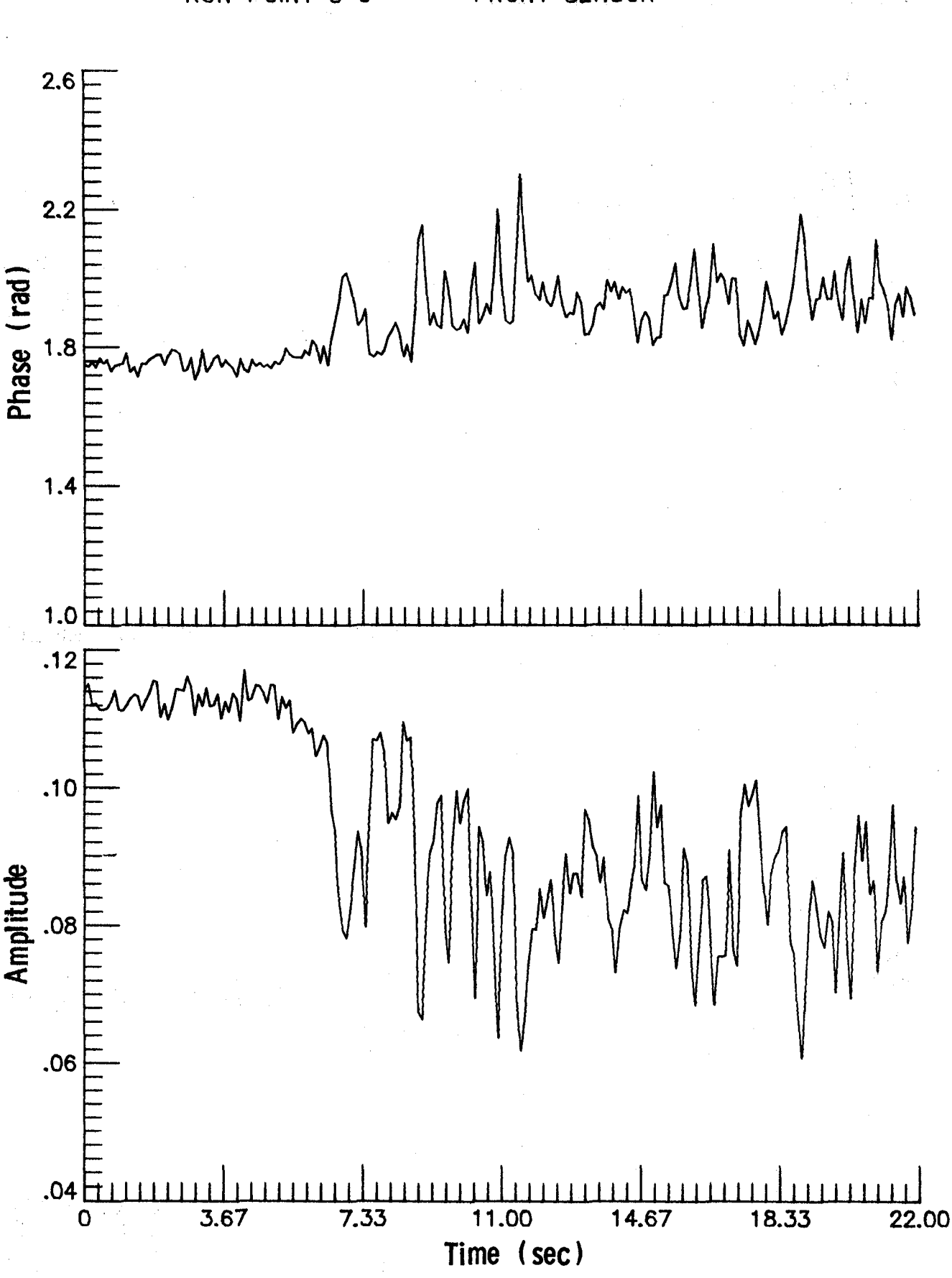

Figure B-30. Reflection coefficient for front sensor in "new" radome.

RUN-POINT 3-6 SIDE SENSOR

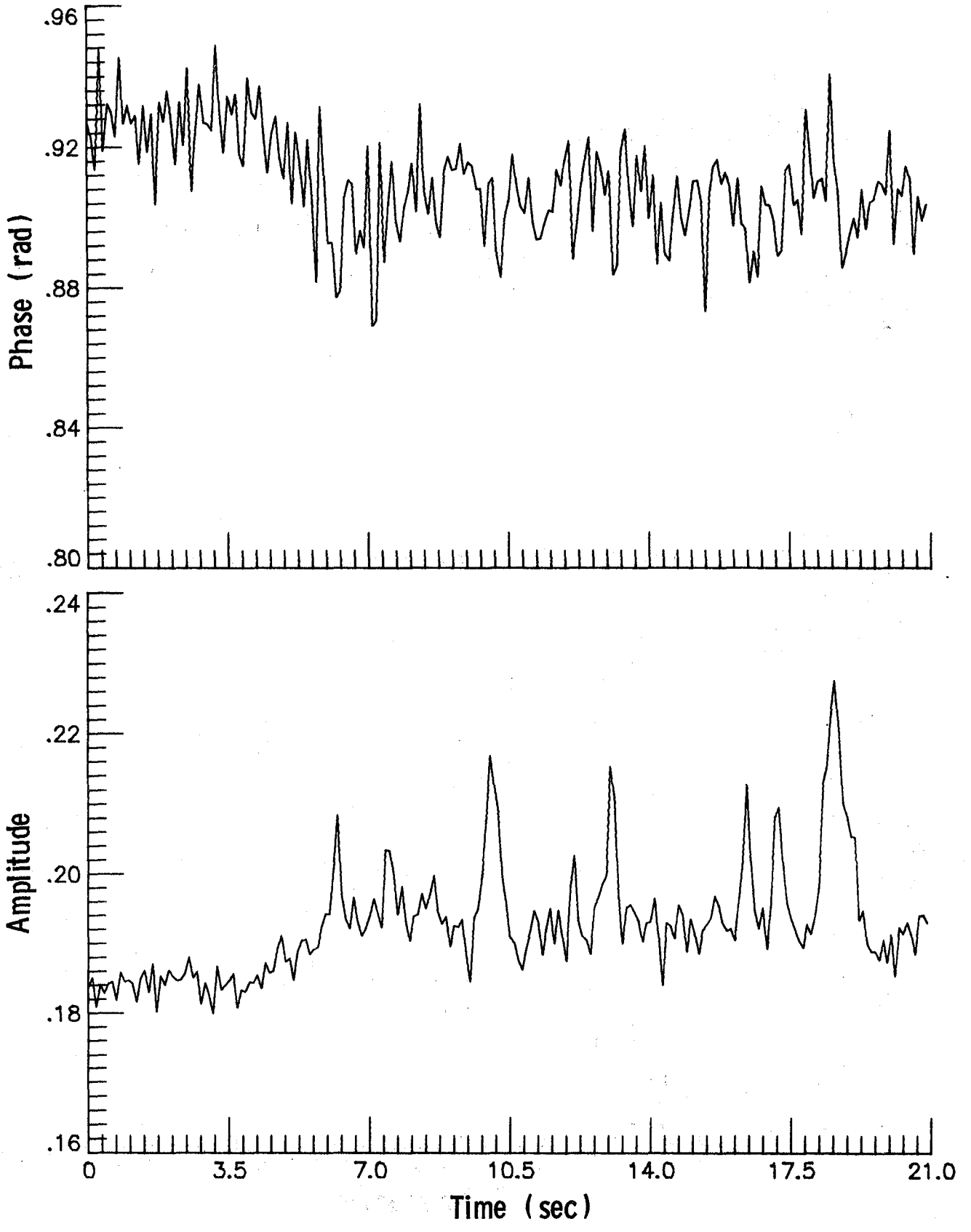

Figure B-31. Reflection coefficient for side sensor in "new" radome.

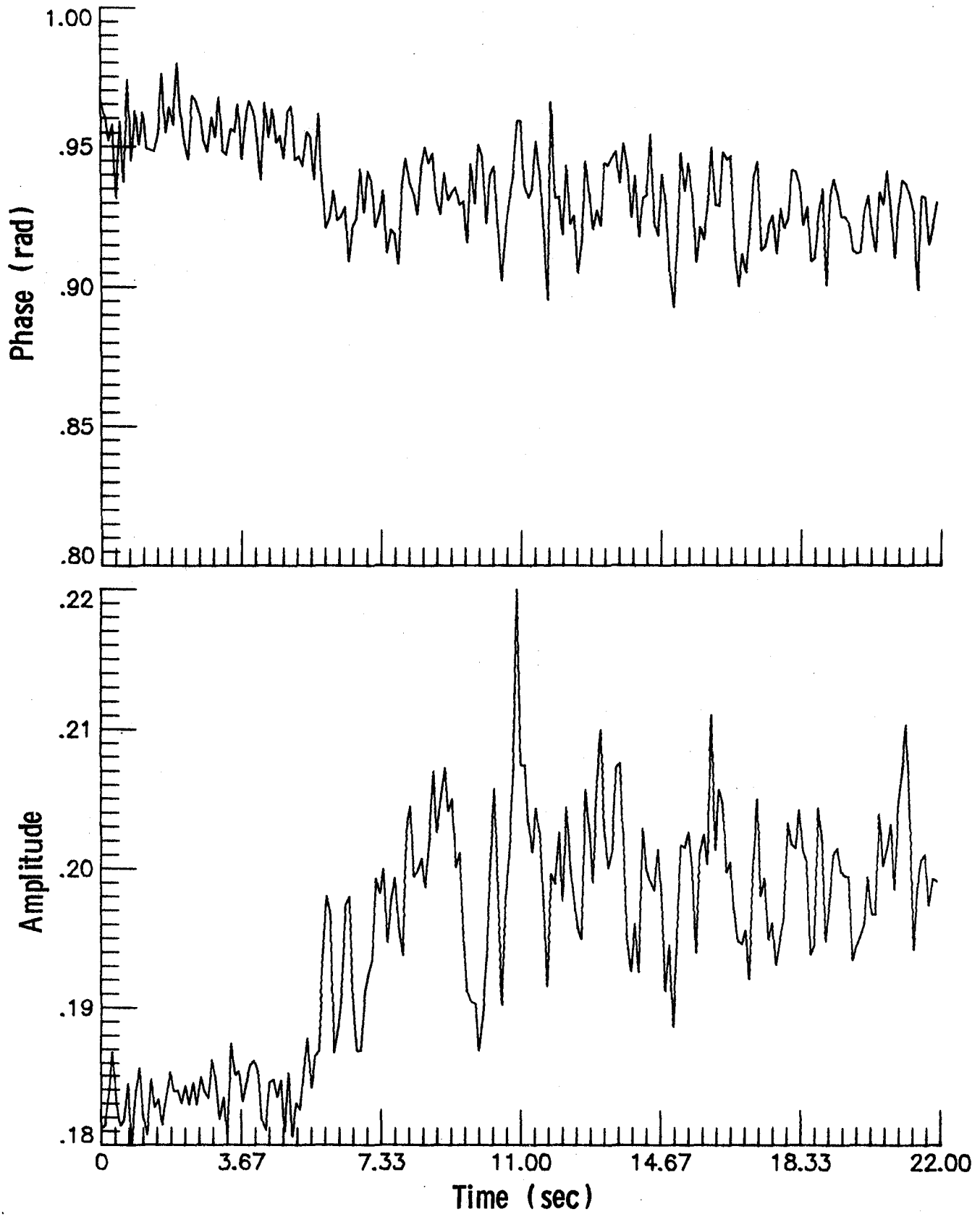

Figure B-32. Reflection coefficient for side sensor in "new" radome.

APPENDIX C

WATER FILM THICKNESS CALCULATIONS

Plots of reflection coefficient vs water spray thickness with water film thickness as a parameter.

NV = relative water volume density

d_t = thickness of spray transition region

d_s = water spray thickness

d_w = water film thickness

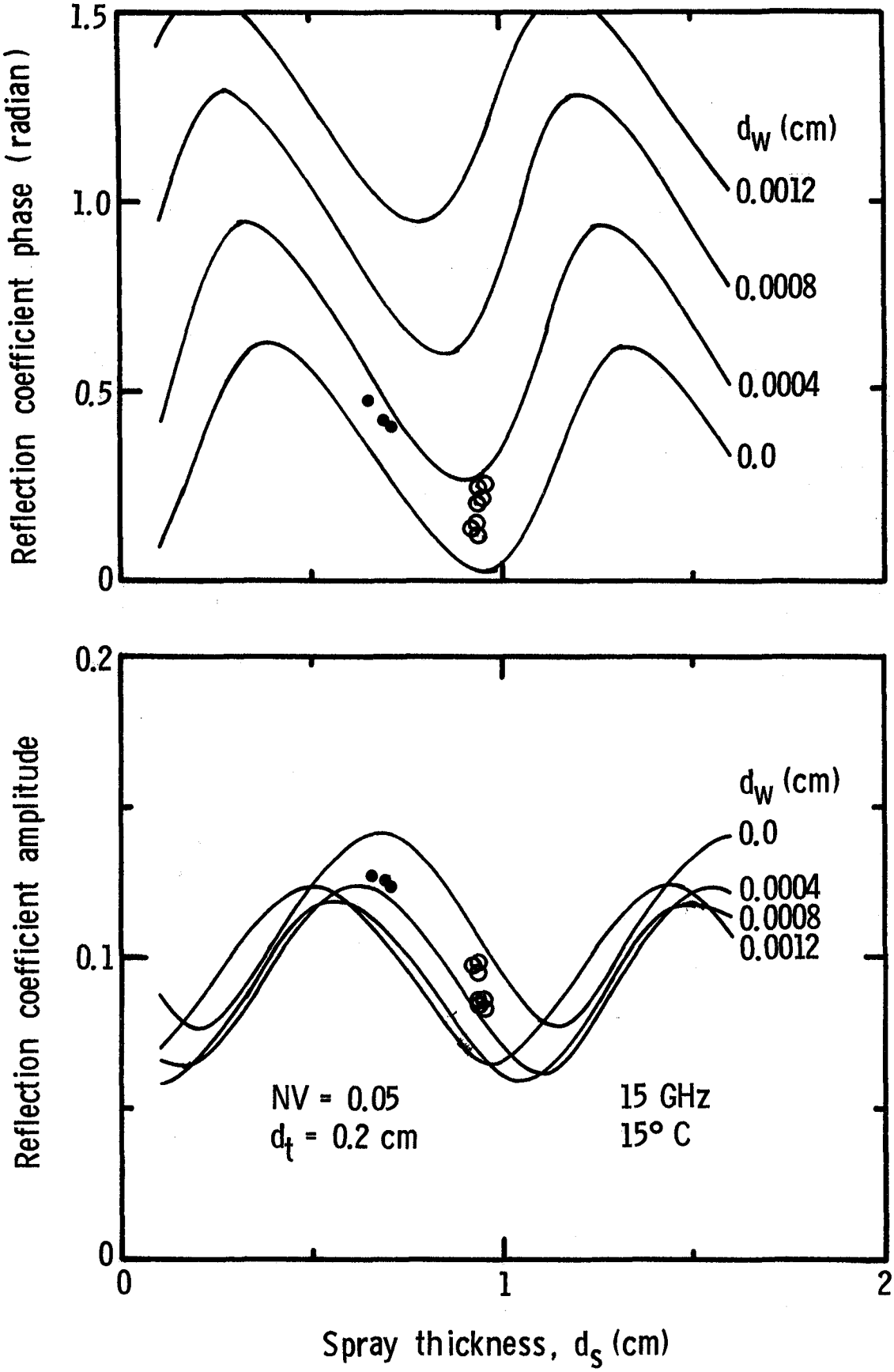

Figure C-1. Comparison between front sensor measured data and calculations.
(● old radome, ○ new radome)

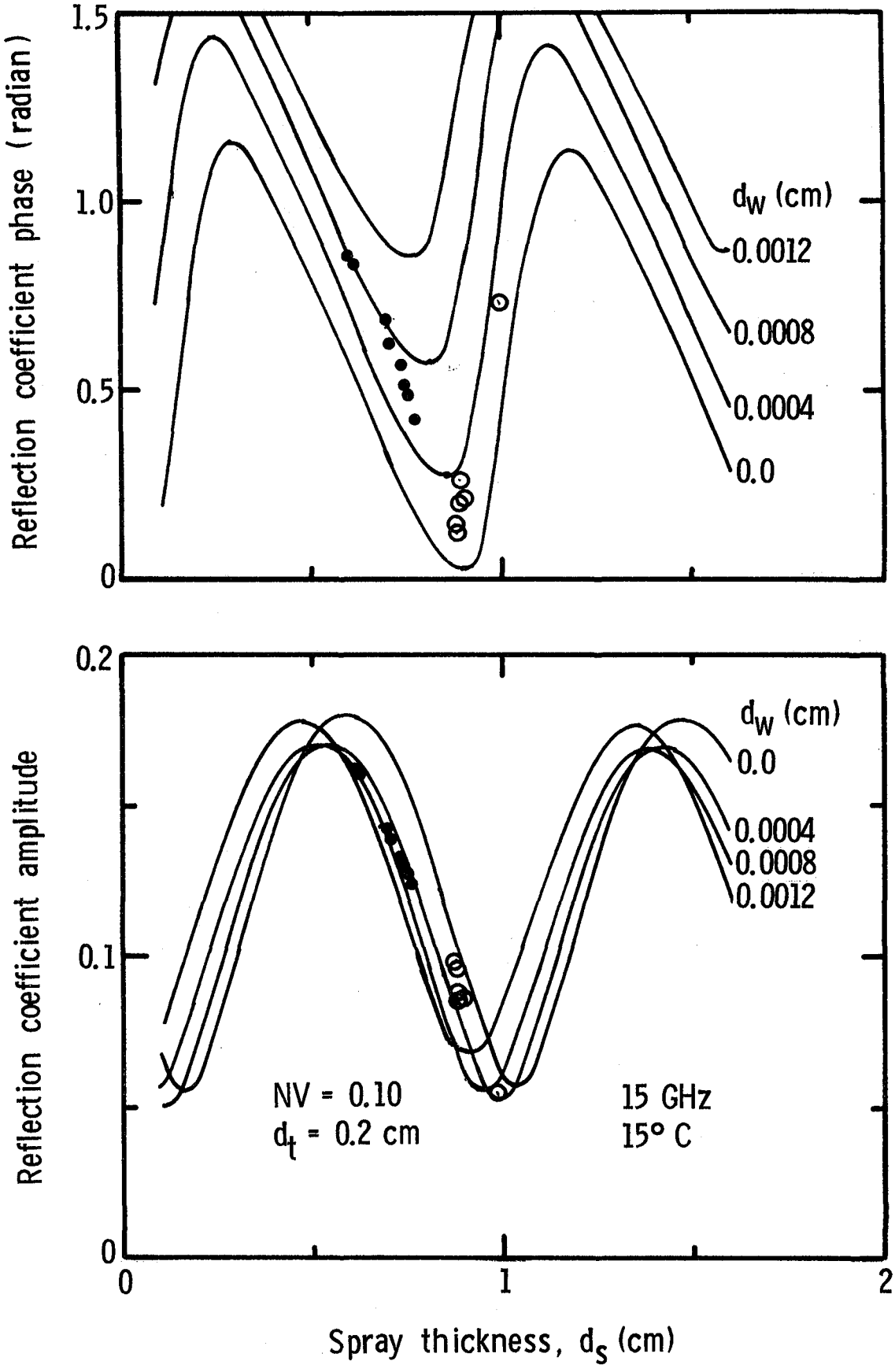

Figure C-2. Comparison between front sensor measured data and calculations. (● old radome, ○ new radome)

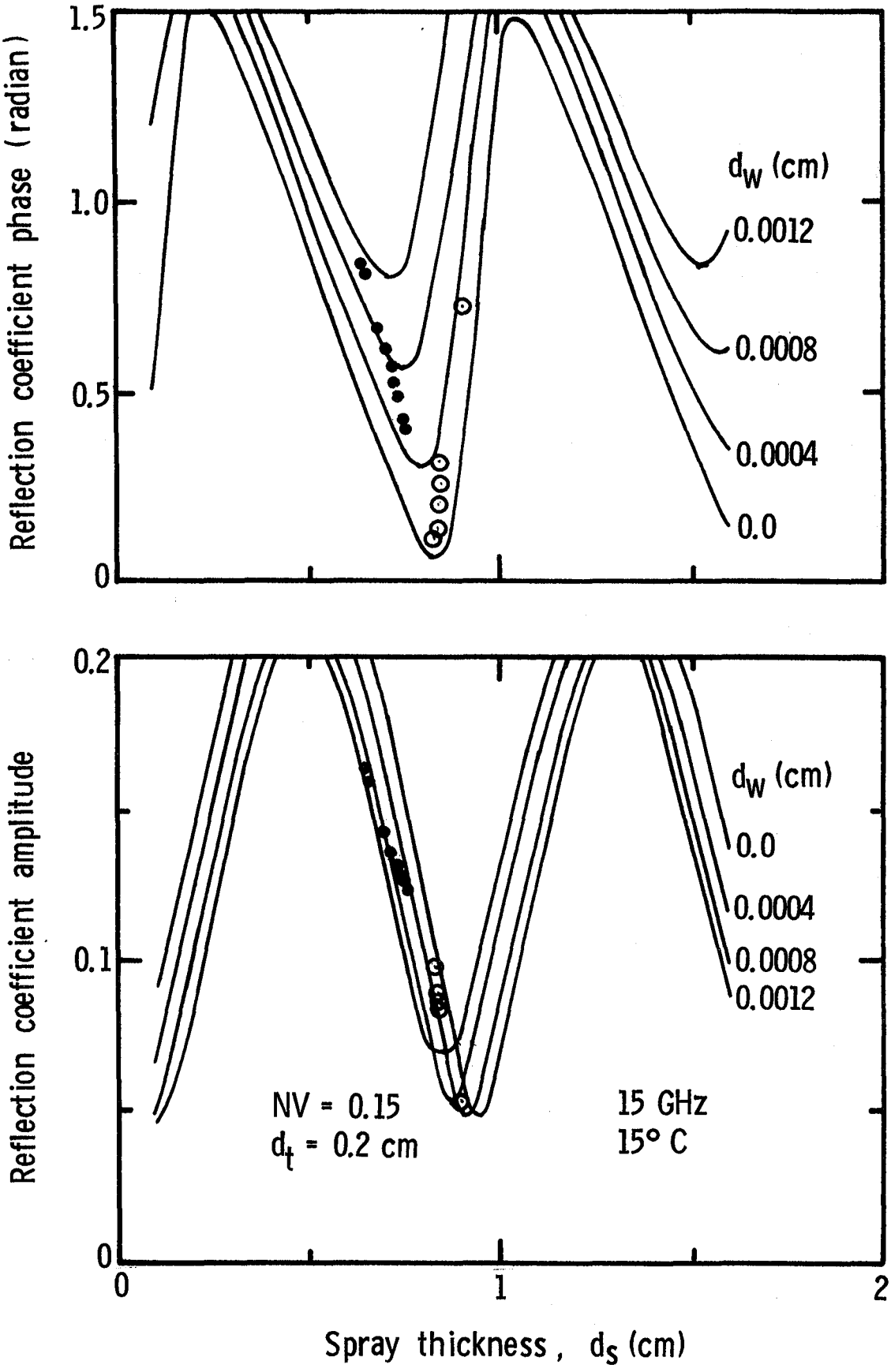

Figure C-3. Comparison between front sensor measured data and calculations. (● old radome, O new radome)

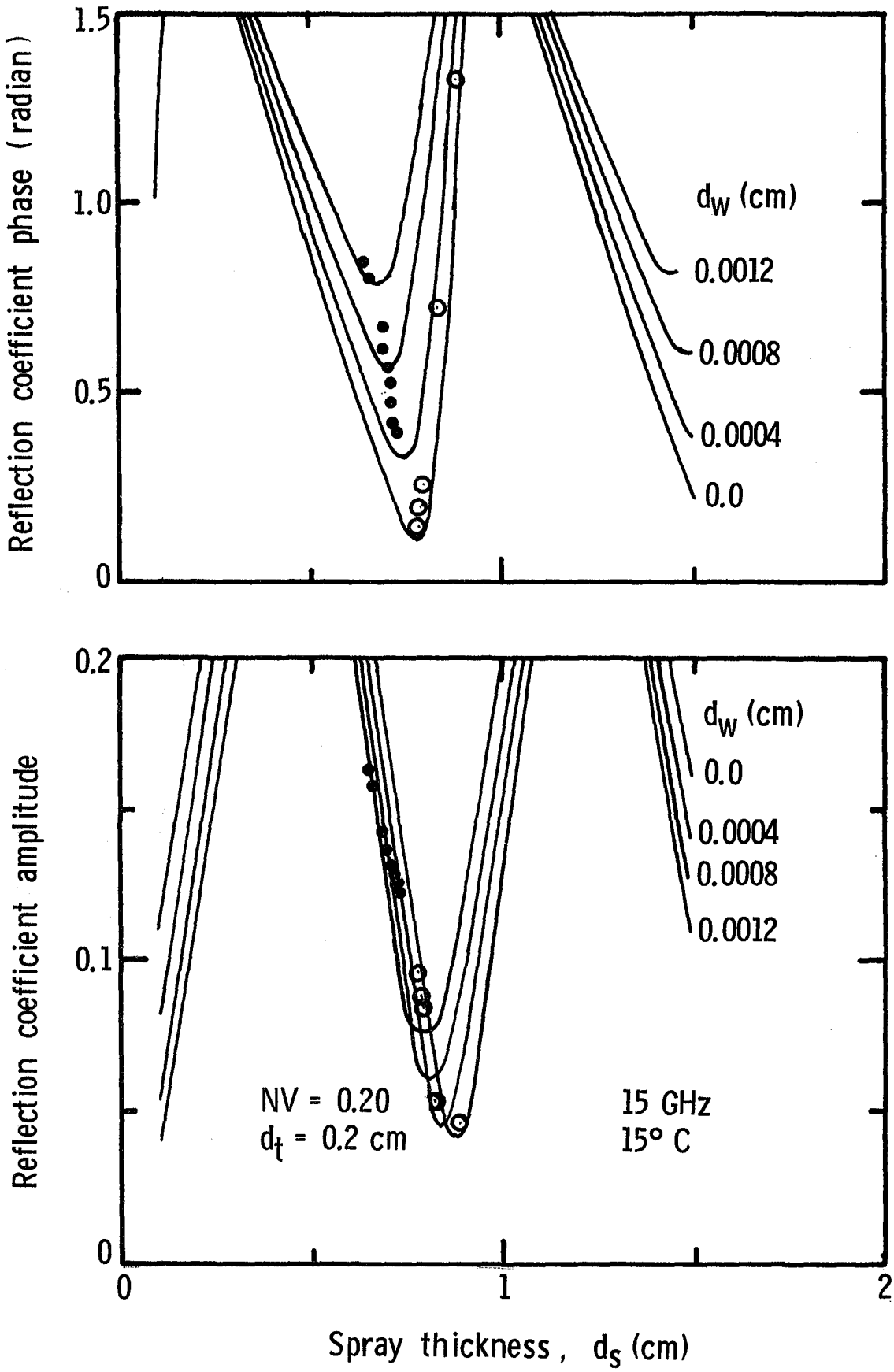

Figure C-4. Comparison between front sensor measured data and calculations. (● old radome, ○ new radome)

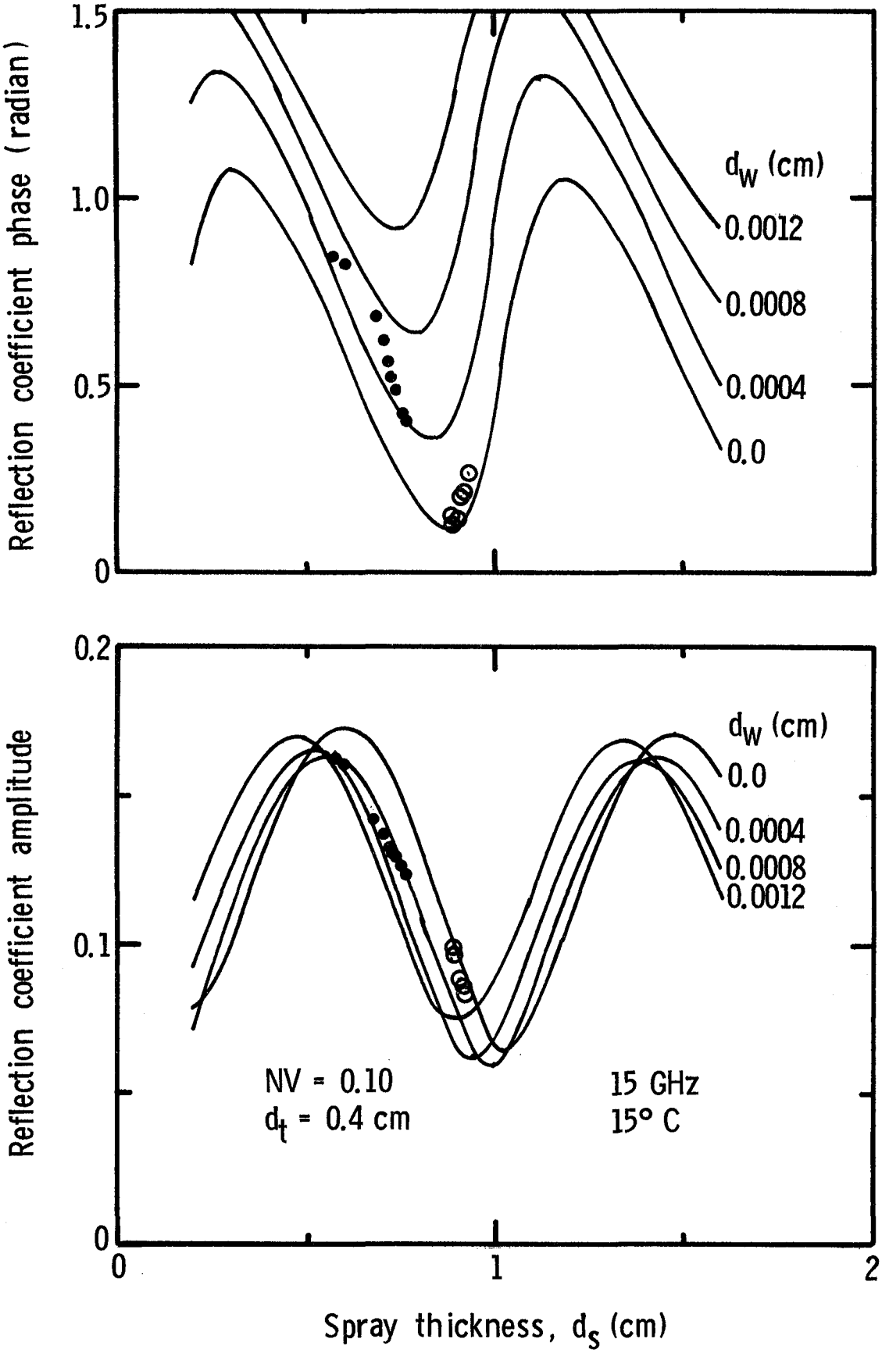

Figure C-5. Comparison between front sensor measured data and calculations. (● old radome, ○ new radome)

IX. LIST OF REFERENCES

1. Technical Facilities Catalog, Vol. I - NHB-8800.5A I, October 1974.

2. Knop, C. M.; Meier, J. J. and Kim, O. K.: The Dielectric Clad Axial Slot Antenna. NASA CR-1057, June 1968.

3. Croswell, W. F.; Westrick, G. C. and Knop, C. M.: Computations of the Aperture Admittance of an Axial Slot on a Dielectric Coated Cylinder. IEEE Trans. on Antennas and Propagation, Vol. AP-20, No. 1, January 1972, pp. 89-92.

4. Richmond, J. H.: Efficient Recursive Solutions for Plane and Cylindrical Multilayers. Ohio State University Technical Report No. 1968-1, August 1965.

5. Klein, L. A. and Swift, C. T.: An Improved Model for the Dielectric Constant of Sea Water at Microwave Frequencies. IEEE Trans. on Antennas and Propagation, Vol. AP-25, No. 1, January 1977, pp. 104-111.

6. Van de Hulst, H. C.: Light Scattering by Small Particles. John Wiley and Sons, New York, 1957.

7. Ginzton, E. L.: Microwave Measurements. McGraw Hill, New York, 1957, pp. 303-307.

8. Hu, Chia-Lun J.: A Novel Approach to the Design of Multiple-Probe High-Power Microwave Automatic Impedance Measuring Schemes. IEEE Trans. on Microwave Theory and Technology, Vol. MTT-28, No. 12, December 1980, pp. 1922-1928.

9. Draper, N. R. and Smith, H.: Applied Regression Analysis. John Wiley and Sons, Inc., 1981.

10. IMSL Reference Manual, Edition 9. IMSL Inc., 7500 Bellaire Blvd., Huston, Texas, 1982.

11. Brown, K. M. and Dennis, J. E.: Derivative Free Analogues of the Levenberg-Marguardt and Gauss Algorithms for Nonlinear Least Squares Approximations. Numerische Mathematik, Vol. 18, 1972, pp. 289-297.

1. Report No.	2. Government Accession No.	3. Recipient's Catalog No.
NASA TM-85813		

4. Title and Subtitle	5. Report Date
An Investigation of the Existence of a Surface Water Layer on Aircraft Radomes During Simulated Flight in Heavy Precipitation	June 1984
	6. Performing Organization Code 505-34-13-53
7. Author(s) J. R. Branstetter**, (Editor), M. C. Bailey*, C. P. Hearn*, R. E. Dunham, Jr.*, R. H. Couch*, H. A. Verstynen**, G. L. Gentry*, and J.B. Williams*	8. Performing Organization Report No.
	10. Work Unit No.
9. Performing Organization Name and Address NASA Langley Research Center, Hampton, VA 23665 and FAA/Langley Development & Logistics Field Office	11. Contract or Grant No.
	13. Type of Report and Period Covered Technical Memorandum
12. Sponsoring Agency Name and Address National Aeronautics and Space Administration, Washington, DC 20546 Federal Aviation and Administration, Washington, DC 20591	14. Sponsoring Agency Code DOT-FA79WAI-061

15. Supplementary Notes

* NASA Langley Research Center

** FAA/Langley Development and Logistics Field Office

16. Abstract

An experiment to investigate the electromagnetic attenuation effects of an impacting water spray on an aircraft weather radome was conducted in Langley's 4 X 7 m. wind tunnel equipped with a water spray system. Results indicate no significant liquid water film formed at the stagnation point of the radome under the test conditions. However, a water "sheath" was observed standing away from the radome surface, which could possibly have significant attenuation properties of its own. Due to the lack of fidelity in modeling both the natural environment with the tunnel apparatus and the water sheath, it is recommended that further studies be undertaken to better define the water distribution in the vicinity of the radome and measure its effect on weather radar performance.

17. Key Words (Suggested by Author(s))
WEATHER RADAR
AIRCRAFT RADOME
WATER ATTENUATION
WATER LAYER

18. Distribution Statement
Unclassified--Unlimited

Subject Category 03, 04, 32

19. Security Classif. (of this report)	20. Security Classif. (of this page)	21. No. of Pages	22. Price
UNCLASSIFIED	UNCLASSIFIED	93	A05

For sale by the National Technical Information Service, Springfield, Virginia 22161